Hyperon Production in Proton-Sulphur Interactions at 200 GeV/c at the CERN OMEGA Spectrometer

Mark Venables

Thesis submitted for the degree of
Doctor of Philosophy

School of Physics and Astronomy,
Faculty of Science,
University of Birmingham.

August 1997.

Author's Contribution

The author's contribution to the OMEGA series of experiments can be broken down into two distinct categories. The larger of the two was the analysis effort. In addition to this, the author aided in the setting up of the WA97 and WA102 layout and triggers.

The analysis effort is again split up into two parts; Monte Carlo simulations and real data analysis. The author modified all of the previously existing analysis and Monte Carlo software such that it was tuned to the conditions for the 1993 proton beam, sulphur target data–taking. Having done that, the real data was processed and corrected using the results from the Monte Carlo simulations. The author also re–ran the track reconstruction program on all of the level one data, taking into account the changes in the data structure between the sulphur beam run and the proton beam run.

During several visits to the the European Centre for Particle Physics, the author assisted in the setting up and running of the WA97 and WA102 experiments, being mainly involved with the trigger aspects of the experiments.

Synopsis

The production of strange and anti–strange hyperons is an important probe in the study of the hot, dense environment of ultra-relativistic heavy ion collisions. The aim of the WA94 experiment is to investigate ultra-relativistic heavy ion collisions at the CERN OMEGA Spectrometer, following the attempts of the WA85 collaboration to produce an exotic state of matter known as a Quark Gluon Plasma.

The WA94 experiment used a sulphur ion beam from the CERN Super Proton Synchrotron and a sulphur target, data was taken in 1991. As a control, in the autumn of 1993, the beam was changed to protons. Particles were detected in the region of central rapidity and transverse momentum greater than 0.6 GeV/c. The analysis and results from the proton beam data form the basis of this thesis.

By detecting the weak decays of Λ, $\overline{\Lambda}$, $\Xi^-$and $\overline{\Xi}^+$ particles, the relative production yields and transverse mass can be determined. These results are compared not only with the results from the sulphur beam run, but with the results from the WA85 experiment. The anti–particle to particle ratios are consistent when comparing proton beam data to sulphur beam data. There is an increase of about 30% in the $\overline{\Xi}^+$ to $\overline{\Lambda}$ ratio when going from proton–nucleus to sulphur–nucleus interactions. The inverse slope parameters from the transverse mass distributions give information about the temperature inside the collision region. In the proton–sulphur data, these parameters are lower than those for sulphur–sulphur interactions.

The production of charged kaons and negative particles has also been studied. The ratio of K^-/K^+has been measured in both proton–sulphur and sulphur–sulphur inter-

actions. The negative particles have been interpreted as being π^-s, giving an inverse slope parameter of 171 ± 1 MeV. The negative particle yield is also used to give absolute enhancements of strange particles.

Acknowledgements

I should like to begin by thanking Professors George Morrison, John Dowell and John Kinson for giving me the opportunity to undertake a Ph.D. in the School of Physics and Space Research at the University of Birmingham. I would not have been able to start a Ph.D. without the financial support given to me by PPARC, to whom I am very grateful.

I would like to thank Doctors Orlando Villalobos Baillie and David Evans for the huge amount of technical help, advice and patience that has surely been tested throughout my three years of bumbling incompetence, summed up in the months preceeding the submission of this thesis. Thanks must definitely go to Doctors Frank Votruba and Noel Carney, whose mere presence during otherwise excruciatingly dull evenings at CERN probably saved my life. A hearty 'ta' to Doctor Andrew Kirk who made the earlier parts of OMEGA meetings weeks interesting and made me homesick with his dulcet Brummy tones. In general, the OMEGA members of staff have shown me that there is another way of making students work apart from standing over them and threatening them with undergraduate–style tutorials; they even include we humble students in their rounds of beers too. Doctor Lawrence Lowe has also been of great help with his computing expertise.

Much thanks must go to my fellow students and inmates at Griffin Close. My sister Clare is always there for me. I trust my fiancée Rachel Jackson will be. Finally, my thanks at this point go to my parents, whose love, support and bizarre wish to adopt me I could never have done without as well as their being the people I've most looked up to.

I consider the people I've mentioned in these acknowledgements (and plenty of people I haven't been able to mention) as family. It is to them that I dedicate this thesis.

Mark Venables, August 1997, Birmingham.

“ Reason says ‘Miracle’: Newton says ‘Doubt.’
Aye! that’s the way to make all Nature out.
‘Doubt, doubt, and don’t believe without experiment’:
That is the very thing that Jesus meant,
When he said ‘Only believe! believe and try!
Try, try, and never mind the reason why!’”

William Blake, *You Don’t Believe.*

“ Why thus my soul should be consigned to infelicity,
Why always I must feel as blind to sights my brethren see,
Why joys they’ve found I cannot find abides a mystery.”

Thomas Hardy, from *The Impercipient.*

“ By thy grace I remember my Light, and now gone is my delusion.”

Chapter 18, Verse 73, *Bhagavad Gita.*

“ Then the Dean repeated the mantra that has had such a marked effect on the progress of knowledge throughout the ages.
‘Why don’t we just mix up absolutely everything and see what happens?’ he said. And Ridcully responded with the traditional response.
‘It’s got to be worth a try,’ he said.”

Terry Pratchett, *The Hogfather.*

“ O Lord, never suffer us to think that we can stand by ourselves, and not need Thee.”

John Donne.

Contents

List of Figures

List of Tables

Chapter 1

The Quark Gluon Plasma

1.1 Introduction

In the early part of the last decade, groups at CERN and BNL started to design and build experiments to study the behaviour of hadronic matter at high temperatures and densities [1, 2]. The intention was to induce a phase transition from 'normal' hadronic matter to a deconfined state called a Quark Gluon Plasma (QGP) [3]. It was predicted that after the phase change, the hadron constituents behave as particles in an asymptotically free gas.

Work in the QGP field has implications elsewhere in physics. Discovery of a QGP and measurement of its thermodynamic parameters would be extremely important in the study of strong interactions. It has also been proposed that the centre of a neutron star could be dense enough for a QGP to exist [4] and that the Universe, up until about 10^{-5} seconds after the Big Bang, existed as a QGP [5]. Studying heavy ion interactions, possibly producing a QGP in the laboratory is therefore an interesting and relevant branch of particle physics.

Table 1.1: Quark Characteristics.

Quark Flavour	Q/| e |	Bound (dynamical) Quark Mass	Partially Chirally Restored (current) Quark Mass
u="up"	$+\frac{2}{3}$	$m_u \sim m_d \sim 350$ MeV/c^2	$m_u \sim m_d \sim 6$ MeV/c^2
d="down"	$-\frac{1}{3}$		
s="strange"	$-\frac{1}{3}$	$m_s \sim 550$ MeV/c^2	$m_s \sim 150$ MeV/c^2
c="charmed"	$+\frac{2}{3}$	$m_c \sim 1.8$ GeV/c^2	$m_c \sim 1.4$ GeV /c^2
b="bottom"	$-\frac{1}{3}$	$m_b \sim 5.3$ GeV/c^2	$m_b \sim 4.8$ GeV/c^2
t="top"	$+\frac{2}{3}$	Not Observed	$m_t \sim 174$ GeV/c^2

1.2 The Quark Gluon Plasma

1.2.1 Quantum Chromodynamics

In the quark model of hadrons [6], a baryon is built from three objects known as quarks, each with half–integral spin. Protons and neutrons are built up of two types of quark, up and down. The properties of these quarks are shown in table 1.1. To build up a proton, one requires two 'up' quarks and one 'down' quark. In a similar way, the neutron is built from two 'down' quarks and one 'up' quark. The arrangement of the spins of these quarks has to be such that the total spin of the tri–quark object is $\frac{1}{2}\hbar$.

A complication arises when the Δ^{++} baryon is included in this model. It has spin $\frac{3}{2}\hbar$, which means that it is a fermion and requires a total wavefunction that is antisymmetric. To get the spin and charge of the Δ^{++} correct, one needs three 'up' quarks with their spins aligned, which is a configuration forbidden by the Pauli Exclusion Principle. To circumnavigate this problem, a new degree of freedom was proposed. Each quark in a hadron was assigned a 'colour' for this new degree of freedom, such that each quark in a baryon had to have a different 'colour', either red, blue or green.

As all of the quarks in the Δ^{++} are positively charged, there must be another, strong force binding it together. A quantum field theory was devised which was similar to the highly successful Quantum Electrodynamics (QED) [7], the quantum field theory of the electromagnetic interaction. Just as in QED, in quantum chromodynamics (QCD) there is a gauge boson which carries the force [8]. The QCD gauge boson is called a *gluon*. Due to the non-Abelian nature of the QCD Lagrangian, the gluon also has colour. This is different from the QED case, in which the photon carries no electric charge. There are two major consequences of the gluon carrying colour and therefore being able to interact with itself.

The first consequence is that the quarks have to be confined. Two quarks, at short distance, interact by gluon exchange, much like two electric charges interacting by photon exchange. At short distances, the strong and the electromagnetic potentials share a $\frac{1}{r}$ dependence. When two quarks are pulled apart, however, the lines of colour force are squeezed into a tube of flux or 'string' along the line joining the two quarks. The energy contained in this string grows linearly with distance, so that the colour potential has the form

$$V_s \sim -\frac{\alpha_s}{r} + \sigma r$$

where α_s is the strong coupling constant, σ is the string tension and r is the distance between the two quarks [8]. The linear term implies that an infinite amount of energy is required to free a quark. This is known as 'quark confinement'.

The second consquence is the QCD variant on charge screening in QED. In QED, an electron emits and absorbs photons which can produce virtual e^+e^-pairs. The original charged particle will be surrounded by these pairs in such a way that the virtual positrons will be closer to the original electron and the virtual electrons will be further away. This arrangement will hide the bare charge of the electron, making the effective charge smaller. A similar process occurs in QCD, but the emitted gluons can emit quark–antiquark pairs or more gluons. The total effect is to 'anti–screen' the bare quark. In other words, the effective colour charge *increases* with distance [13]. In the case of a hard interaction between a colour probe and a quark, the colour force between the two will reduce and in extreme cases, the force is so small that it is said that the two particles are 'asymptotically free'.

1.2.2 QCD Phase Transition

It has been proposed that under the rules of QCD, particles holding a colour charge become asymptotically free if they are energetic enough to break through colour anti–screening [3]. A consequence of this phenomenon is that under extreme temperatures and densities, nuclear matter could undergo a phase transition and 'melt' into an asymptotically free gas of quarks and gluons. This state is referred to as a Quark Gluon Plasma (QGP). Astrophysicists believe that the core of neutron stars might exist as a QGP [4] and that the Universe, at a time 10^{-5} s after the Big Bang existed as a QGP [5]. Both the early Universe and neutron star states are shown on the phase diagram in figure 1.1. Quantum mechanics and statistical mechanics have been used to produce equations of state for strongly interacting matter using the MIT bag model [9, 10, 11] and these are also shown on figure 1.1.

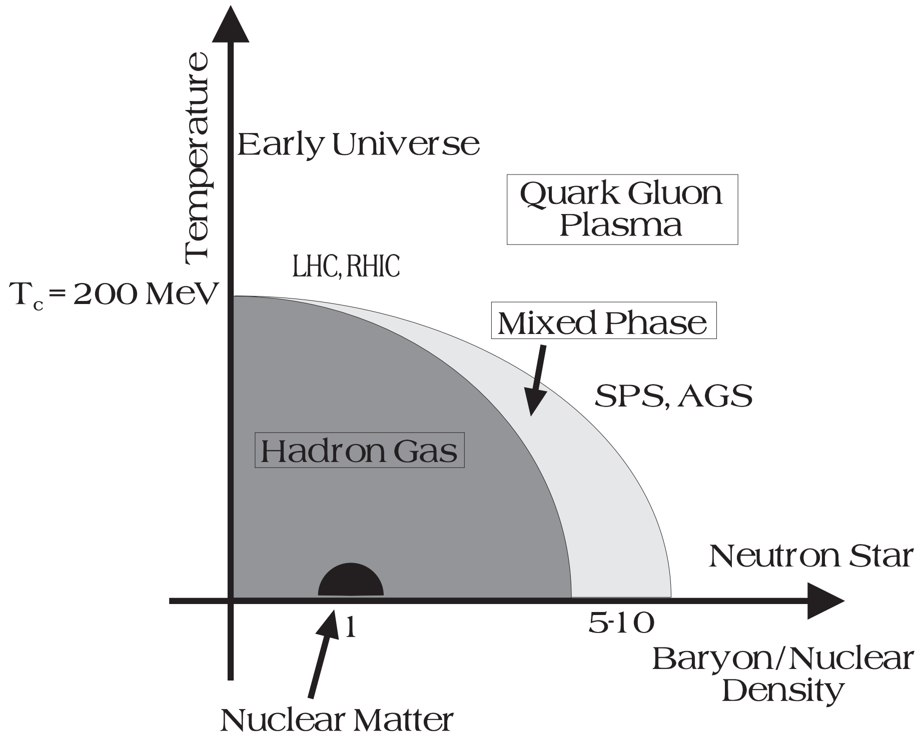

Figure 1.1: Phase diagram showing various the hadron gas, mixed and QGP phases of matter.

Lattice QCD has been employed to cope with the complex conditions such as in–medium effects which cannot be dealt with using ordinary perturbative methods. An example of lattice calculations is shown in figure 1.2 where the energy density and pressure for QCD matter with two light quark flavours has been calculated as a function of temperature [12]. At the critical transition temperature, T_c, the energy density undergoes a rapid phase transition from the low, hadron gas values to the much higher QGP values.

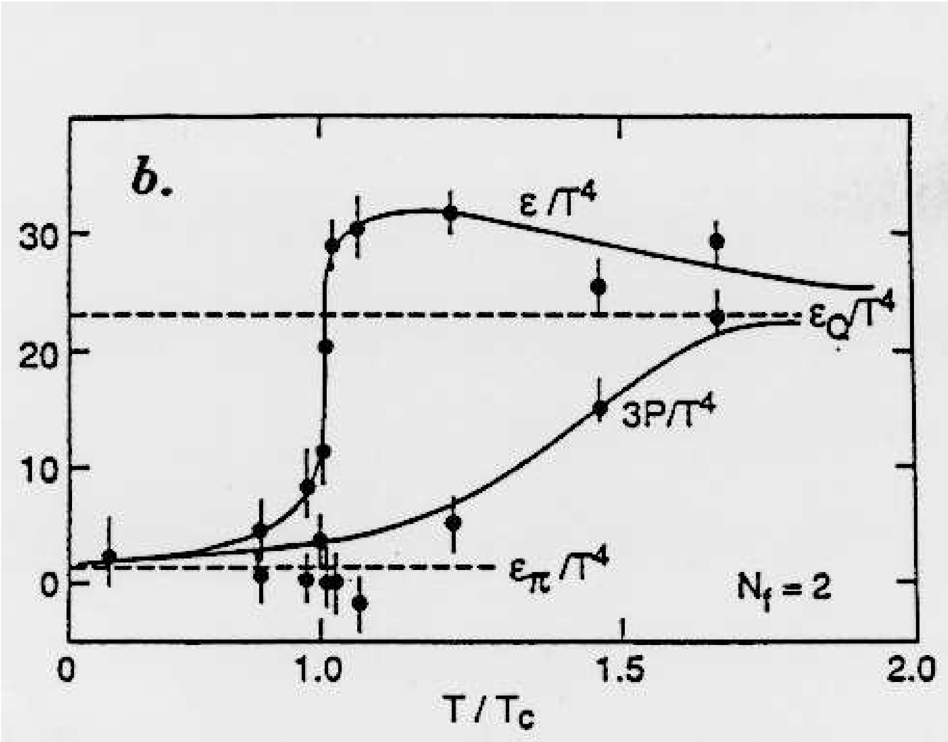

Figure 1.2: Energy density ϵ and pressure P for QCD matter with quarks of two flavours, as a function of the temperature T.

1.3 Heavy Ion Physics

Nucleus–nucleus collisions are believed to be an excellent experimental environment in which QGP formation is possible. The energy densities and temperatures which these collisions attain is thought to provide the most suitable environment to induce a phase transition from 'normal' hadronic matter into a QGP.

The major advantages of using ultra–relativistic heavy ion collisions instead of previously available hadron–hadron collisions when trying to create a QGP are two–fold. Experiments try to create an extended region of high energy density, in which the centre–of–mass energy is converted into thermal energy of the state. The interactions involved in heavy ion collisions mean that the fraction of the beam energy deposited in the collision – the stopping – is greater than in the more transparent hadron–hadron interactions. The stopping at the Super Proton Synchrotron (SPS) accelerator energies for nucleus–nucleus collisions was found to be about 70% [14] and even higher for the Alternating Gradient Synchrotron accelerator energies [15]. The proportion of matter available for thermalisation is therefore higher than in the lower energy collisions. The size of the region of high energy density rises with increasing atomic number of the projectile nucleus. This is important since the lifetime of the fireball increases with an increase in its size. Proton–ion interactions, in which QGP formation is not expected, are used as an experimental control.

Figure 1.3 shows an idealised schematic representation of an ultra–relativistic heavy ion collision in the centre of mass frame. In the lower part of the figure is the baryon centre of mass rapidity distribution one would expect from such a collision, where rapidity is defined as

$$Y = \frac{1}{2}\ln\frac{E + p_{\mathrm{L}}}{E - p_{\mathrm{L}}}$$

where E is energy of a given particle and p_{L} is the particle's longitudinal momentum. Between the projectile and target regions, one expects a flat region of particle density, centred on $Y^* = 0$, which corresponds to $Y = 3.0$ in the laboratory frame for a sulphur–sulphur collision at SPS energies. This central region is where the 'hot fireball' should

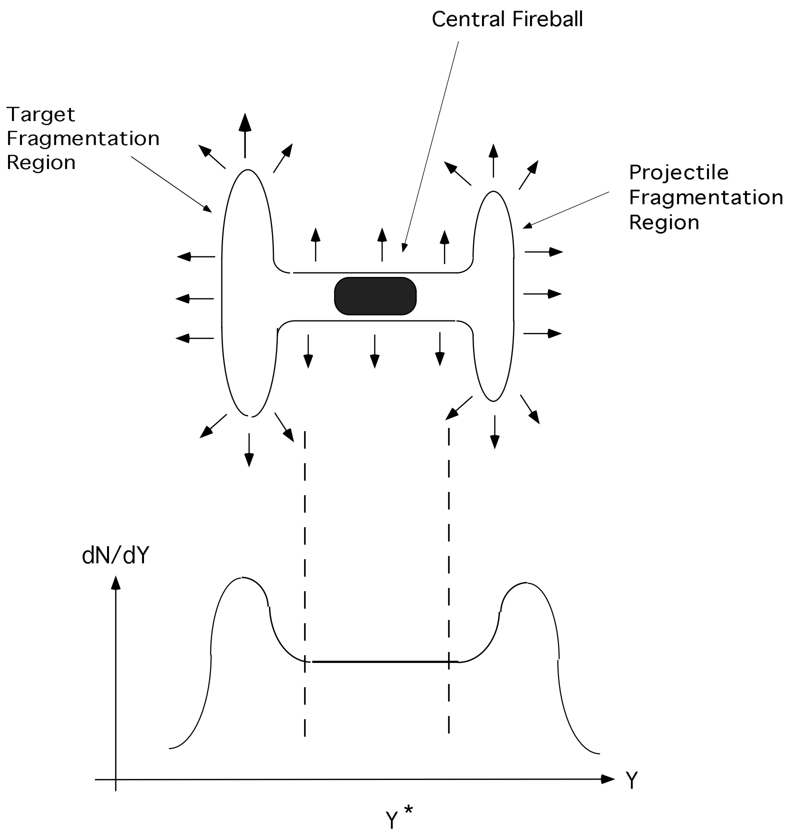

Figure 1.3: Idealised schematic representation of a heavy–ion collision, with rapidity distribution.

be formed and is where the greatest energy densities should be. Figures 1.4a) and 1.4b) show the proton rapidity distributions for increasing ion size and for central and peripheral (glancing) collisions from the E866 [15] and NA35 experiments [16]. This figure shows the peaks for the target and projectile regions and also, by comparing the separation of the peaks for silicon–aluminium with the gold–gold distributions, the relative amounts of stopping.

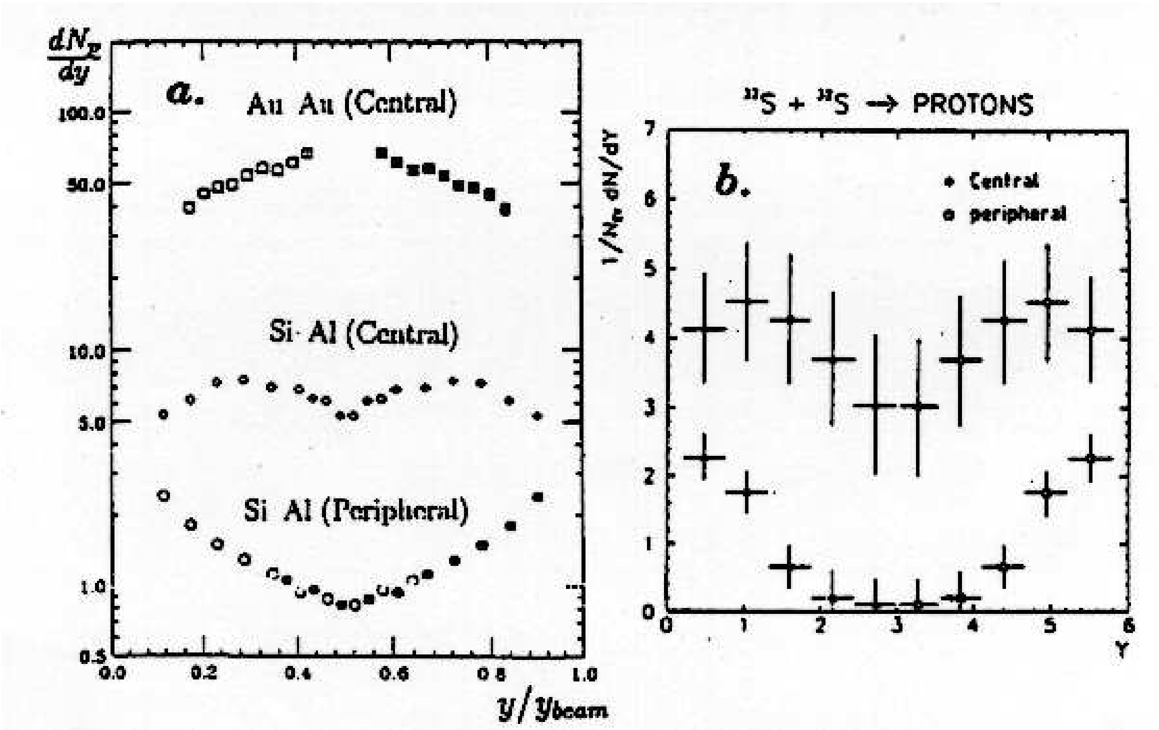

Figure 1.4: a) Rapidity distributions from E866 at the AGS and b) NA35 at CERN.

1.4 Signatures of the Quark Gluon Plasma

Figure 1.5 shows a scenario for the evolution of a QGP. The fireball is expected to last in the region of 10^{-23} seconds, during which time its temperature should drop due to expansion and radiation of particles – mainly pions from its surface. When the temperature and density falls enough, hadronisation will occur. The observed particle yields will reflect the properties of the system at hadronisation, so one has to select signals of QGP formation that remain constant or change very little during hadronisation. It is therefore important that a proposed signal should not couple to the strong interaction or should have quantum numbers that do not change under strong interactions. There now follows a brief description of several important proposed signatures, the last of which describes strangeness enhancement, the selected signal of the WA94 experiment.

1.4.1 Direct Photons

Direct photons provide one of only two proposed signals emitted by the QGP that can reach the detector directly. Photons can be produced by quark–quark annihilation

$$q\overline{q} \rightarrow \gamma g$$

or quark–gluon interaction

$$qg \rightarrow \gamma g$$

The small cross–section for electromagnetic interactions allows the photons to escape. The background for this signal is very large, however, and comes mainly from the decays

$$\pi^0 \rightarrow 2\gamma$$

and

$$\eta \rightarrow 2\gamma/3\pi^0$$

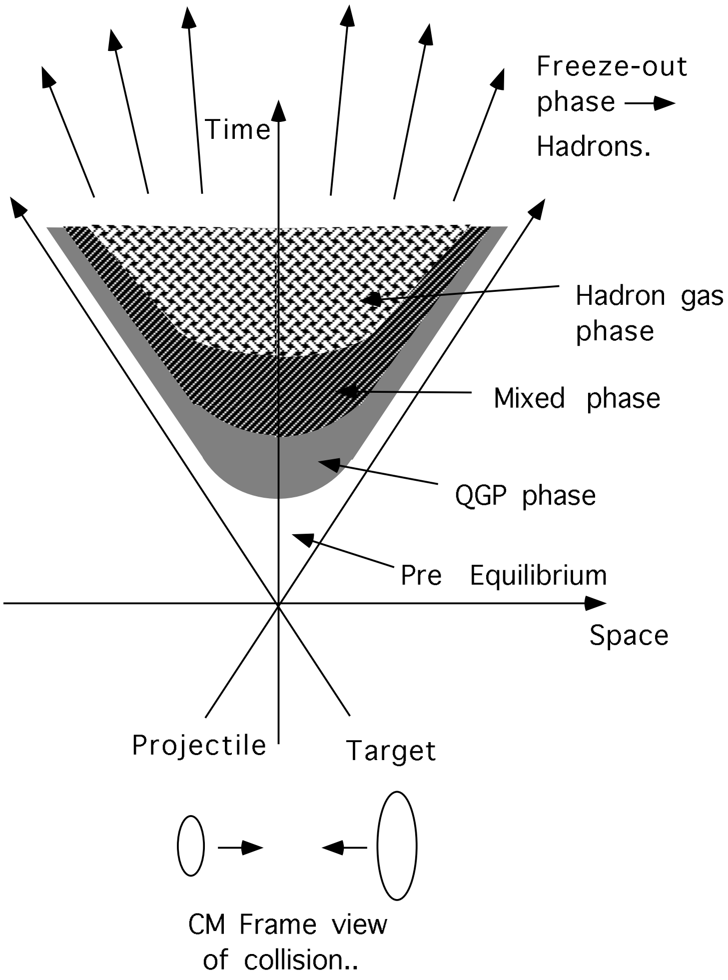

Figure 1.5: Spacetime evolution of a heavy ion collision

There are two approaches for direct photon searches. The first, employed by the NA45/CERES collaboration [20] involves measuring the ratio of the number of photons and the number of π^0s produced as a function of multiplicity per unit rapidity $\frac{dN_{ch}}{dy}$. It is thought that the production of direct photons increases as the square of $\frac{dN_{ch}}{dy}$ and the production of photons from hadrons increases as $(\frac{dN_{ch}}{dy})$. A fit to the relation

$$G\Big(\frac{dN_{ch}}{dy}\Big) = C\Big(1 + \alpha\frac{dN_{ch}}{dy}\Big)$$

where G and C are constants and $\alpha\frac{dN_{ch}}{dy} = \frac{N_{\gamma}^{dir}}{N_{\gamma}^{hadron}}$ has been performed. The fit is shown in figure 1.6 and α is consistent with being zero showing that there is no evidence for direct photon production.

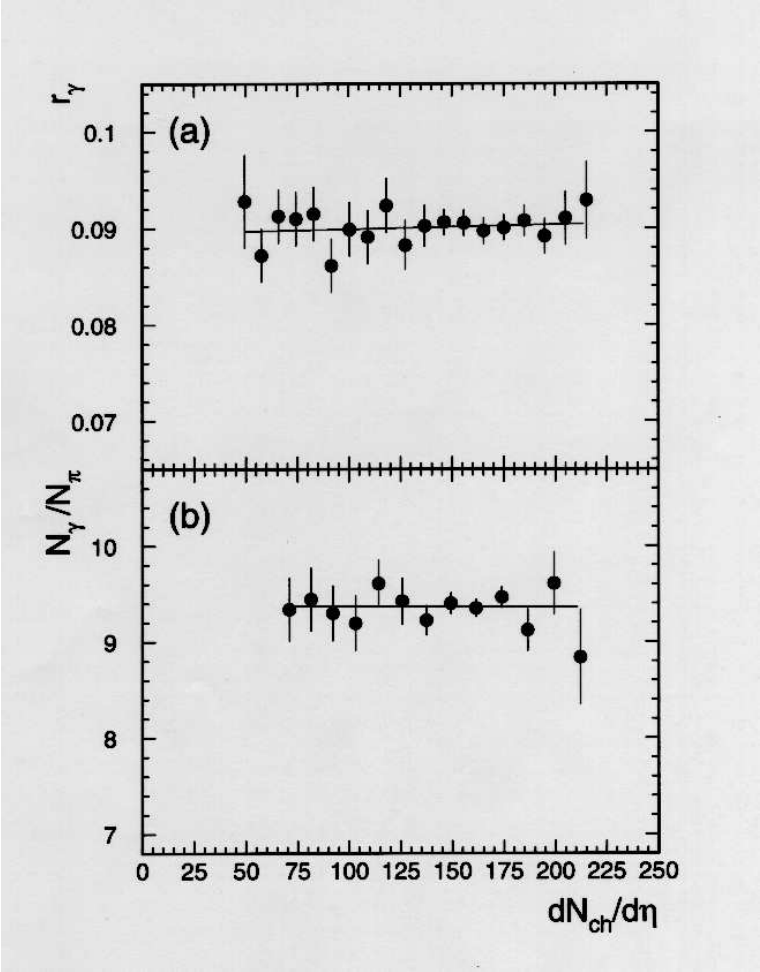

Figure 1.6: Photon production as a function of $\frac{dN}{d\eta}$ from the NA45 experiment.

The second direct photon experiment, WA80 [22], plots the observed $\frac{\gamma}{\pi^0}$ ratio over the same ratio from known background sources as a function of transverse momentum, p_{T}. The fit to a constant value, shown in figure 1.7 gives an excess of $3.7\% \pm 1.0 \pm 4.1$ for peripheral events and $5.0\% \pm 0.8 \pm 5.8$ for central events. Again, this is consistent with there being no direct photon production.

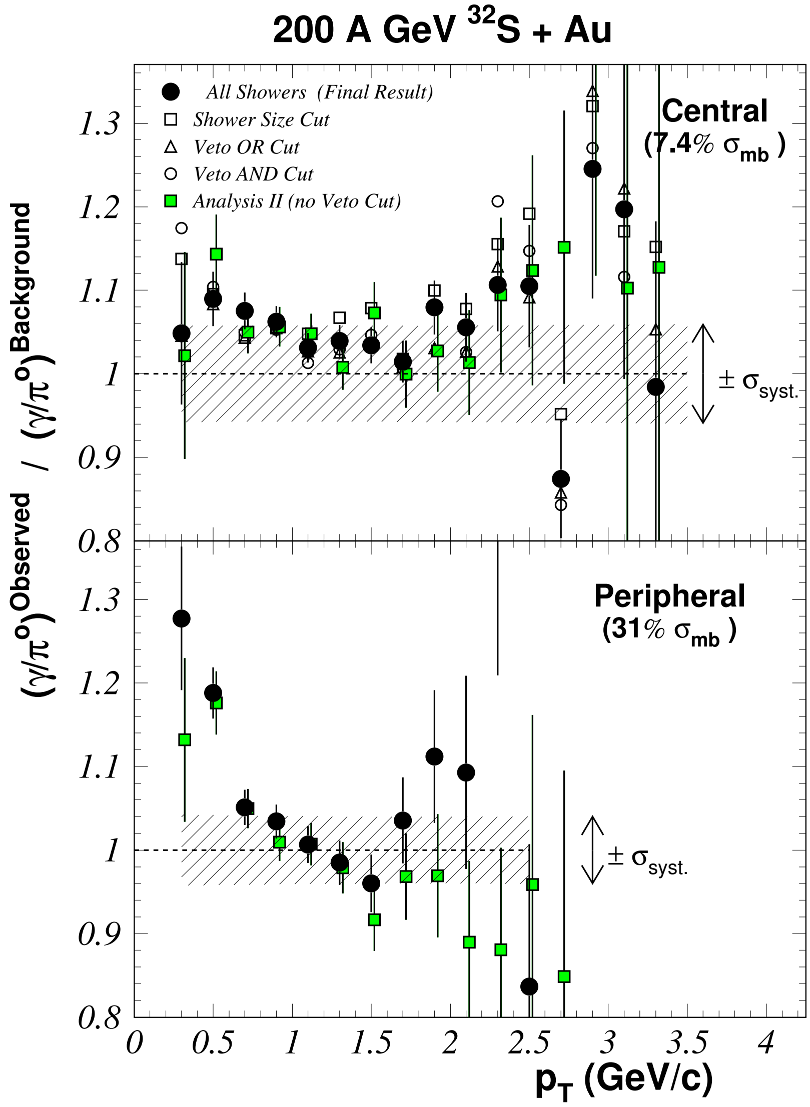

Figure 1.7: p_{T} dependence of photon production from the WA80 experiment.

1.4.2 Dilepton Production

Leptons, particles which couple only to the electromagnetic and weak forces, should be a good probe of a QGP. The study of single lepton production is dogged by the high background from hadronic decays. The observation of high energy lepton pairs, however, seems to be more promising. Lepton pairs are produced *via* electromagnetic quark–antiquark annihilations. The main background is from pion annihilation, but the background is much reduced when compared to that for single leptons. The NA38 collaboration [24] have presented data from sulphur–tungsten and sulphur–uranium interactions and have compared them to data from proton–tungsten interactions. When these data are normalised by considering the number of charged particles per event, there is a clear excess of dilepton pairs in the ρ and ω mass region and also in the region of the ϕ meson mass region as shown in figure 1.8. Recent preliminary results from the NA45 collaboration [25], which studies lead–gold collisions, have also noticed enhancement effects, in the region from about $2m_\pi$ to its extension to the region around the ρ mass, as shown on figure 1.9.

Figure 1.8: Dilepton mass distribution from the NA38 experiment, showing possible enhancement of ϕ mesons.

1.4.3 Chiral Symmetry Restoration and the ρ meson

Solutions of the Dirac equation [8] for massless particles are known to have definite helicity, $\boldsymbol{\sigma} \,.\, \mathbf{p}$. Particles that have mass are an admixture of the two different helicity states. Chirality is defined as the product of helicity with fermion number, so massive fermions can be considered to be admixtures of chiral states. These chiral states are normally referred to as *right*– and *left*–handed states. In hadrons, however, the quarks

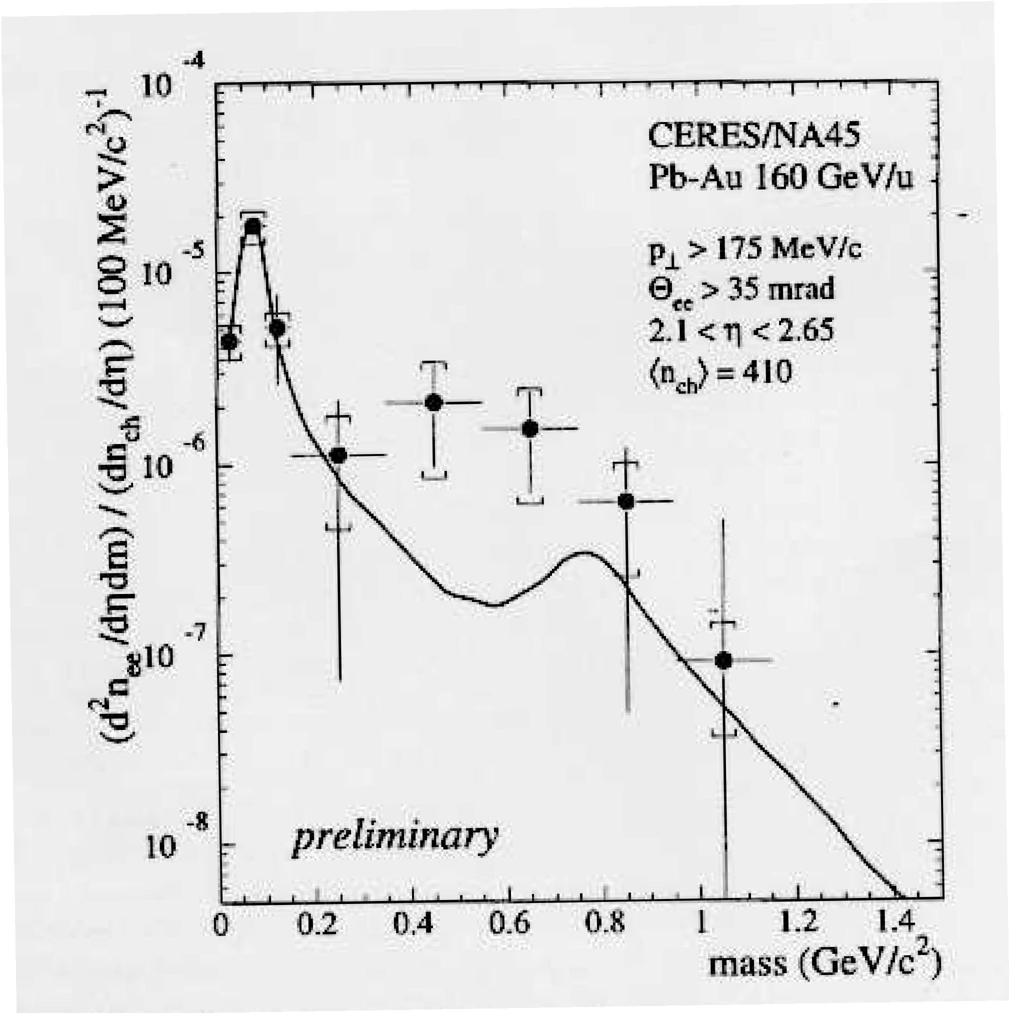

Figure 1.9: Dilepton mass distribution from the NA45 experiment, showing possible enhancement of the ρ meson.

are very light and therefore behave largely as pure chiral states so that mesons are built up in a $SU(N_f)_L \otimes SU(N_f)_R$ way [26].

When the wavefunction of the lightest isospin 1^- meson, the $\rho(770)$, is operated on by an operator of a chiral symmetry group, a small admixture of 1^+ meson wavefunction has to be included to preserve the symmetry. One would expect there to be a 1^+ particle with the same mass as the ρ. It was shown by using current algebra in the zero–temperature limit that nature does obey some sort of chiral symmetry, manifested in the conservation or partial conservation of some currents, and in their commutation relations [27]. This, in turn, constrains the spectra of 1^+ and 1^- mesons, yielding the results that $2m^2(\rho) = m^2(1^+)$ [28]. A 1^+ meson in nature, the $a_1(1260)$, has a mass which differs from that of the $\rho(770)$ by a factor of greater than 1.41 ± 0.01 [29], in very good agreement with theory.

It is predicted by lattice gauge calculations that matter undergoes a phase transition under temperatures produced in relativistic heavy–ion collisions. In this case, the quark masses go from their bound or dynamical masses to their lower 'current' masses. The lifetime of the ρ is much shorter than the expected lifetime of the hot, central part of a heavy–ion collision. It is thought that some ρ mesons decay inside the dense region, retaining their reduced masses. Weakly interacting particles such as dileptons provide a window to the dense–medium effects on the ρ meson. The CERES/NA45 collaboration [24] studies the dielectron channel and the HELIOS–3 collaboration [30] looks at the dimuon channel. Both have observed enhancement of dileptons over the expected scaled proton–proton yield in the invariant mass range $0.2 < m_{l^+l^-} < 1.5$ GeV/c^2, especially in the range $m > m_{\pi\pi}$. This is taken to represent the $\pi^+\pi^-$annihilation channel *via* a ρ meson. The shape of the spectrum in heavy–ion interactions differs from the proton–proton spectrum in such a way that it is difficult to fit from known sources. Models including an in-medium ρ mass, however, fit the data better than keeping a free mass ρ.

1.4.4 J/Ψ and Ψ' Suppression

It has been predicted that the conditions inside a QGP are such that Debye colour screening is important, especially when considering production of resonant charmed quark pairs [31]. At the high densities expected in the plasma, the colour screening radius is smaller than that radius of a bound $c\bar{c}$ pair. In other words, the charm quark and anti–quark do not see each other, thus formation of a bound state, such as J/Ψ or Ψ', is suppressed and D meson production is enhanced when compared to 'normal' hadronic interactions. Ψ's are expected to be supressed more because the bound state radius is greater than that for the J/Ψ and so screening will be more important.

A further feature is that if a J/Ψ or Ψ' is formed in a highly central collision, where the energy density is greatest, there should be a E_T dependence to the suppresion [32]. NA38, and more recently, NA50 looked at the dimuon spectrum for sulphur–uranium and lead–lead interactions respectively [24, 33]. Both experiments observed a depletion of the J/Ψ and Ψ' yield and a E_T dependence as shown in figures 1.10 and 1.11. The data from sulphur–uranium collisions have been shown to be consistent with hadronic re–interaction scenarios [34] whereas the picture for lead–lead interactions is not so well understood. Theories including co–moving particles have had some success in explaining the picture further [35].

1.4.5 Entropy per Baryon

In the event of QGP formation, gluons provide a large increase in the number of degrees of freedom in the system. This, in turn, would give rise to a large increase in the system's entropy, S. The entropy per baryon, S/B, for a 3-flavoured QGP system has been examined using lattice QCD calculations and it was found to be at least twice that found in hadron gas formation under the conditions detected by heavy ion experiments [36].

Experimentally speaking, S and B are not easy to measure directly but can be inferred. The multiplicities of postively and negatively charged particles can be measured (N^+ and N^- respectively), such that the baryon number is assumed to be the difference between the two and the entropy the sum. The EMU05 collaboration performed a measurement using the charge asymmetry

$$D_Q = \frac{N^+ - N^-}{N^+ + N^-}$$

which by the assumptions in the previous paragraph amount to a measurement of B/S. The charge asymmetry was found to be 0.088 ± 0.007 which cannot be reproduced

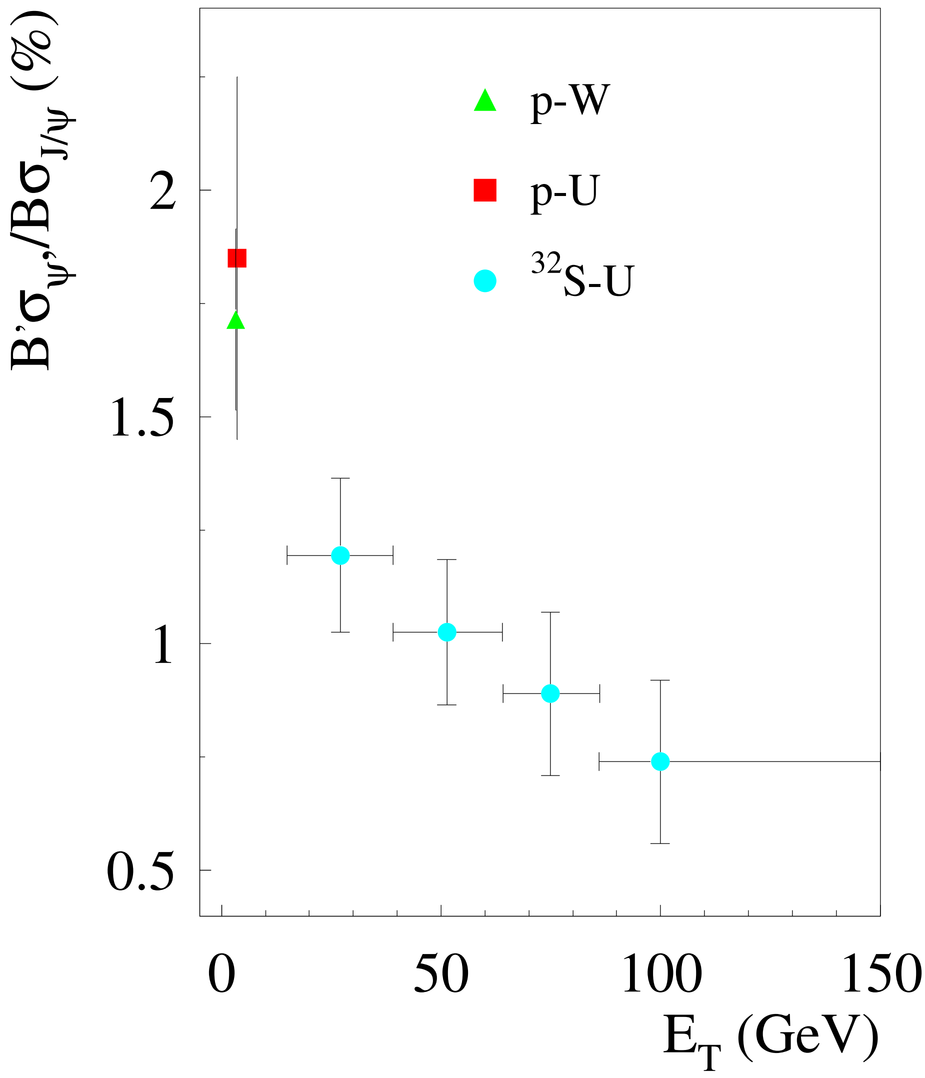

Figure 1.10: Ratio of J/Ψ and Ψ' cross–sections as a function of transverse energy from the NA38 experiment.

by hadronic models. A further measurement of the entropy per baryon, in lead–lead collisions at two beam energies, will be undertaken by the NA57 experiment, which shall start to take data in late 1997 [37].

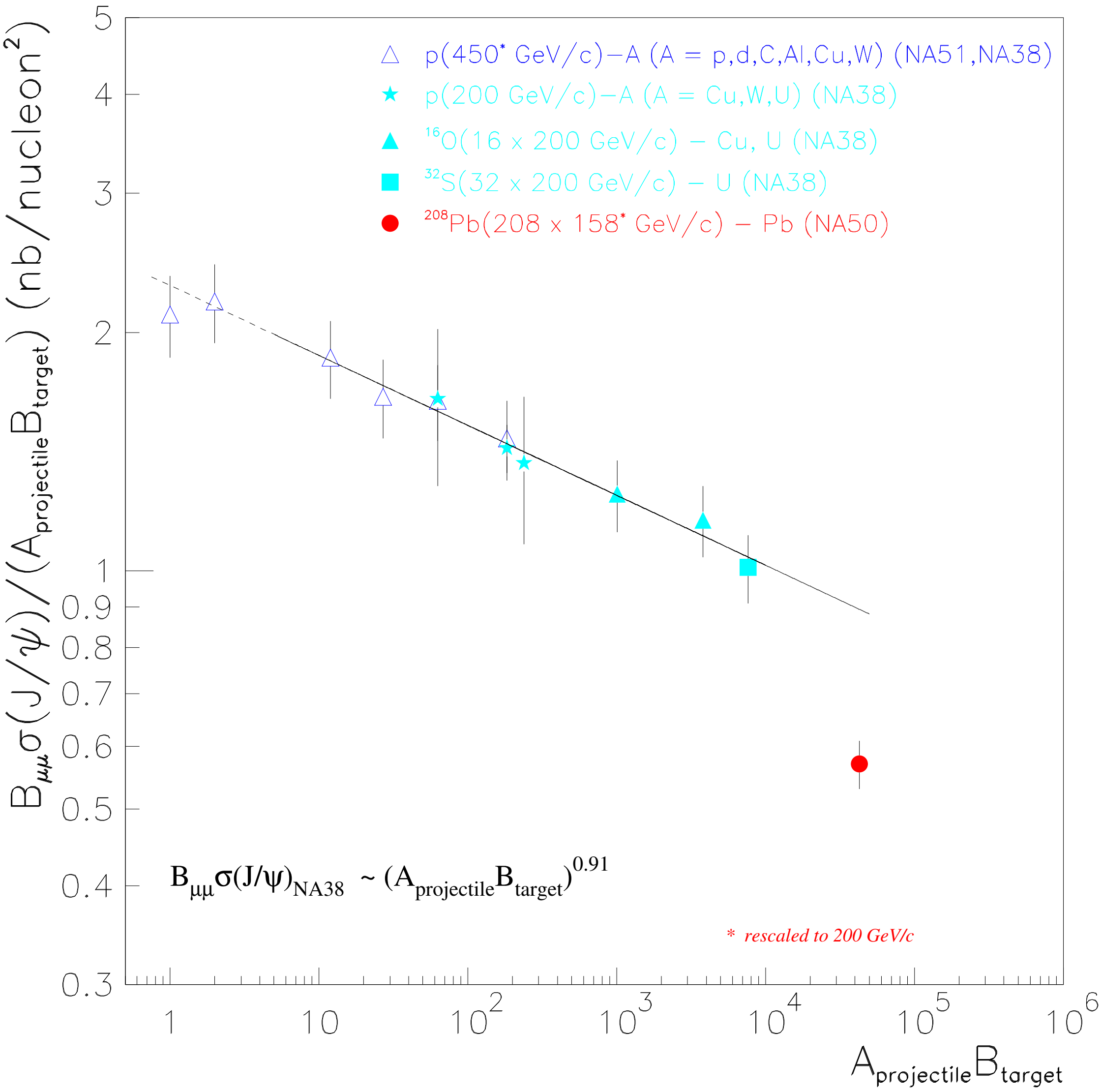

Figure 1.11: Ratio of J/Ψ and Ψ' cross–sections as a function of the product of number of target and beam nucleons from the NA38 and NA50 experiments.

1.4.6 Strangeness Enhancement

Strangeness is produced in heavy ion collisions whether or not a QGP has been formed. Strangeness enhancement, the relative amounts of produced strangeness when comparing nucleon–nucleon and central nucleus–nucleus collisions, is thought to be an excellent signal for distinguishing between a very dense nuclear state, known as a hadron gas (HG) and QGP phases.

The development of a thermal model to interpret data on particle abundances relies upon global parameters characterising the system. To determine the abundances of the various species of strange particles, one must examine how the individual quark flavours go towards chemical equilibration. The chemical potential μ is the energy required either to add a quark of a given flavour to the plasma phase or to add a hadron to the hadron gas phase. This parameter is highly dependent on the quark densities. Light quarks (the up and down quarks) have a chemical potential μ_q and the light anti–quarks have a chemical potential $-\mu_q$ – the anti–quarks might annihilate with quarks of the same flavour. The net strangeness density in the plasma will be zero, as strangeness production comes from $s\bar{s}$. This means that the strangeness potential (μ_s) of the plasma should be zero. This is not necessarily true of the hadron gas phase, since strangeness production is accompanied by light quark production. A brief description of both phases follows.

The production of strangeness in a HG phase is *via* reactions of the sort $h_1 + h_2 \rightarrow$ hadrons. For example,

$$pp \rightarrow p\mathrm{K}^+\Lambda,$$

$$pp \rightarrow pp\mathrm{K}^+\mathrm{K}^-,$$

and

$$pp \rightarrow pp\Lambda\overline{\Lambda}$$

all produce strangeness in the primary collision between constituents of the target and projectile nuclei. Secondary interactions, such as

$$\pi^- p \rightarrow \Lambda\mathrm{K}^0$$

and

$$\pi^-\pi^+ \rightarrow K^+K^-$$

also contribute towards strangeness production. The important point to remember is that the lowest threshold momentum for centre–of–mass production for Λs is 522 MeV/c and for $\overline{\Lambda}$s is 1.83 GeV/c *via* the first and third reactions respectively. This means that the saturation of strangeness phase space, especially *via* anti–baryons, will be quite slow, upwards of a few hundred fm/c, which is much longer than the expected lifetime of the central fireball (approximately 10 fm/c) [17].

In an extended region of QGP, the picture is markedly different. Given that the plasma's radius is of the order of a few fm, several hundred gluons should be produced by the time gluon equilibrium occurs. The high gluon yield leads to a large production of quark–antiquark pairs via the process

$$gg \rightarrow q\overline{q}.$$

Light quark and antiquark production will reach equilibrium after a couple of fm/c. Strange quark production approaches equilibrium more slowly, since the strange quarks are much heavier and are suppressed by a factor $e^{m_s/T}$. The expected temperature of the plasma is about 200 MeV, which is easily great enough for copious and fast production of $s\overline{s}$ pairs. Theory predicts that production of strange quarks should saturate in approximately 3-5 fm/c [41]. At SPS energies, the light quark yields would be suppressed by Pauli blocking [42]; the large baryochemical potential ($\mu_B = 3\mu_q$), resulting from the high u and d quark densities from the original colliding ions would inhibit the production of further light quark pairs, meaning that s (and especially $\overline{s}$) production is enhanced relative to light quarks and antiquarks. This would be reflected in an increase in the yield of strange and multistrange particles and antiparticles when compared to a hadron gas scenario.

The fore–runner to the WA94 experiment, the WA85 experiment [1] took data from 1987 to 1990, using a sulphur beam and then a proton beam incident on a tungsten target. The relative production of Λs, Ξ^-s and their antiparticles were measured. The anti–particle/particle ratios stayed constant when going from proton–tungsten to sulphur–tungsten, but the $\frac{\Xi^-}{\Lambda}$ and $\frac{\overline{\Xi}^+}{\overline{\Lambda}}$ ratios both increased by about 40%, which corresponds to a two and a half standard deviation effect. In addition, transverse mass distributions gave some information about the temperature of the central fireball. The WA85 experiment was also the first heavy ion experiment to detect an Ω signal (see figure 1.12)

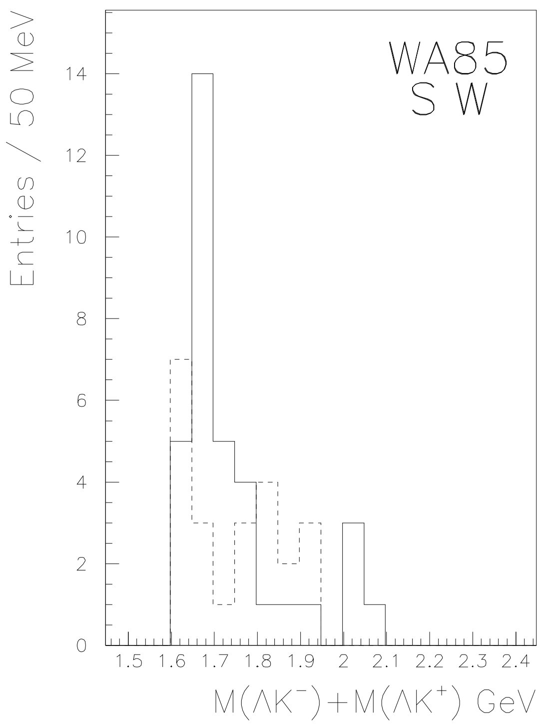

Figure 1.12: $\Omega^- + \overline{\Omega}^+$ signal detected by the WA85 experiment.

Recently, string models have provided an alternative approach to strangeness production in heavy ion collisions. The basis of such models is the description of low p_{T} hadron–hadron collisions in terms of interactions between strings [43]. Additional production mechanisms such as final state interactions, colour rope formation [44, 45], string fusion [46] and quark droplet formation [47] have all been considered in order to account for the observed strangeness enhancement.

Recent fits to all of the published data using thermal models show that thermal and chemical equilibrium might have been reached in relativistic heavy ion collisions at both the AGS and SPS. Hadron yields for the silicon and sulphur beams are in reasonable agreement with at least one fit [48, 49], which shows that the available phase space is filled and that the freeze–out parameters are very close to the phase boundary between a hadron gas phase and a QGP phase. Indeed, it is very difficult to reach thermal equilibrium and also to fit the experimental data with using a QGP scenario.

In summary, production of strange and multistrange baryons and antibaryons should be sensitive to a phase transition from normal hadronic matter to a QGP phase. Heavy, strange particles and particularly anti–baryons are thus an excellent signature of QGP formation. The WA94 experiment, and the WA85 experiment before it, studies the relative production of Λs, Ξ^-s and their antiparticles (along with other strange particles). Both experiments use a sulphur beam to create a dense, baryon rich environment and a proton beam as a control, WA94 using a sulphur target and WA85 a tungsten target.

1.4.7 Strangelets

It has been proposed that Strange Quark Matter (SQM or strangelets) might also be formed in a QGP [38, 39]. Stranglets are objects stable relative to nuclear matter or metastable compared to weak interaction timescales. Experiments such as the NA52 experiment at CERN have attempted to measure strangelets *via* the charge to atomic number ratio with arrangements of time–of–flight counters, Čerenkov detectors and calorimeters. For strangelets, the ratio is lower than that for normal nuclear matter. NA52 have observed one strangelet candidate [40], but are awaiting further data and an upgrade to the short–lifetime section of the detector to confirm their observations.

1.5 Summary

The study of ultra–relativistic heavy ion collisions has implications both inside and outside of particle physics, namely in helping to understand QCD and possibly even the early Universe itself. There are several predicted signals of a QGP, including strangeness enhancement. The WA94 collaboration has measured ratios of strange particles and found evidence of enhancement. As a control, the beam was changed from sulphur ions to protons in late 1993. Analysis of the hyperons found in the proton beam, sulphur target experiment forms the basis of this thesis.

Chapter 2

The WA94 Experiment: The Proton-Sulphur Apparatus and Trigger

2.1 Introduction

The WA94 experiment was designed to explore the nature of the central fireball region created in ultra-relativistic sulphur-sulphur interactions and to search for evidence of a phase transition from normal hadronic matter into a new state of matter – the QGP. The signature that WA94 uses is strangeness enhancement. In order to appreciate the extent of strangeness enhancement, it is important not only to examine heavy systems such as sulphur–sulphur, but also the cleaner environment of proton-sulphur interactions. In this case, the energy density is not thermalised, hence a QGP is unlikely to occur. The data from this lighter system provide results that are the benchmark for comparison with the results from the sulphur–sulphur data. This chapter will describe the experimental set-up (figure 2.1) and the trigger (figure 2.5) that were employed in the 1993 proton–sulphur run.

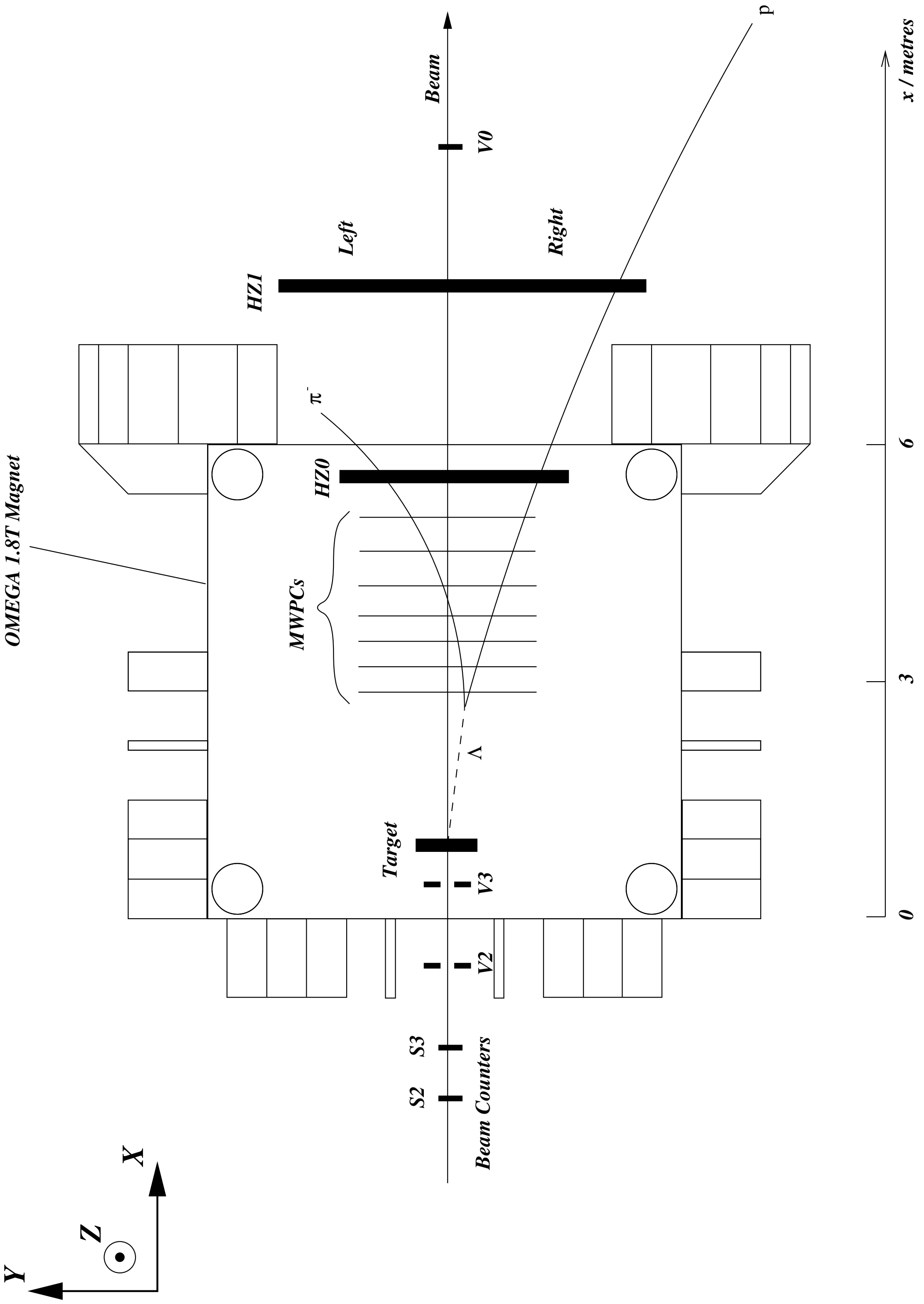

Figure 2.1: Experiment layout for the 1993 proton-sulphur run.

In order to study the hyperons that are produced in heavy ion collisions, the WA94 experiment concentrates on the weak decays

$$\Xi^- \to \Lambda + \pi^-,$$

$$\Lambda \to \mathrm{p} + \pi^-$$

and their charge conjugates. The identification of these decays is made more difficult, ordinarily, by the large number of other charged tracks; around 300 in each sulphur-sulphur interaction. To reduce this problem, the detectors were designed so that they only detected tracks in a narrow phase space window ($p_{\mathrm{T}} \geq 0.6$ GeV/c and $2.0 < Y_{LAB} < 3.2$). The charged particle multiplicity in the detectors is thus reduced by almost two orders of magnitude.

2.2 Beam

The CERN Super Proton Synchroton (SPS) produces a beam of protons whose momentum is 450 GeV/c. In order to reduce the momentum of each proton down to 200 GeV/c - the beam of sulphur ions had momentum 200 GeV/c per nucleon - the beam was focused onto a 400 mm thick beryllium target. The resulting beam passed through a series of quadrupole and dipole magnets – in order to select particles with the correct momentum – and steered onto the sulphur target in the OMEGA spectrometer. Protons were selected using the Čerenkov differential counters which are explained later.

2.3 The OMEGA Spectrometer

The OMEGA spectrometer consists of a superconducting magnet whose two Helmholtz coils produce a magnetic field of 1.8 T. The target and most of the detectors for track identification sit inside the field region produced by the magnet. Just as in the sulphur run, data were taken for both field polarities. Although the system is symmetric with respect to charge, reversing the field is important to reduce residual systematic errors in the fine alignment of the detectors.

A useful system of co-ordinates is that which is defined relative to the centre of the OMEGA spectrometer. In this system, the beam crosses the $x = 0$ cm ($x_\Omega = 0$ cm) at $y_\Omega = 0$ cm and $z_\Omega = -0.5$ cm. The beam travels along the x-axis of this system. The main component of the magnetic field is in the OMEGA z-direction.

2.4 The Target

The position of the sulphur target was $x_\Omega = -215$ cm. For the 1993 proton run the target thickness was chosen to be 9% of an interaction length. This corresponds to a thickness of 40.5 mm.

2.5 Detector Descriptions

Detectors were used for two different purposes; tracking and triggering. The major detectors were seven modules of Multi-Wire Proportional Chambers (MWPCs) – the A-chambers – which were used for tracking the decay products of the hyperons produced at the target. Two scintillator hodoscopes were placed downstream of the A-chambers and were used in part of the trigger. Upstream of the target were two threshold Čerenkov differential counters with achromatic ring focus (*CEDAR*s) which selected beam particles that were protons; about thirty-five *per cent* of the beam particles were pions.

2.5.1 Multiwire Proportional Chambers

The main reason for including MWPCs in an experiment such as WA94 is to find points on the paths of charged particles. Tracks can then be fitted to these points and by finding the curvature of these tracks, momentum values can be assigned to the particles that made them. The first four A-chambers also provided a multiplicity condition in the trigger, the idea being that this would enhance the detection of strange particle decays.

The A–chamber modules consisted of three wire planes known as U, V and Y planes. The Y plane wires were along the z-direction of the OMEGA co-ordinate system and provided information about the y co-ordinate of a hit in the chambers. It was also the plane in the middle of the three. The wires of the U and V planes were inclined at angles of $+10.14°$ and $-10.14°$ to the z-axis respectively and this is shown in figure 2.2. The reason for having three planes at angles to each other is to resolve an ambiguity problem. If one simply has two orthogonal planes, and two wires fire in each plane, there is an ambiguity in the position of the real hit (N tracks give N^2 space points on one plane).

The 752 anode wires in each plane are spaced 2 mm from each other. The gas in each chamber was a mixture of argon, isobutane and ethanol. When a charged particle passes through a wire plane, a cluster of wires can fire, though usually only one fires. By using the clusters from all three planes it is then possible to determine the true point on the track. Each chamber behaves in this way and thus it is possible to get a maximum of seven points for each charged particle track. The seven chambers were positioned at $x_\Omega = 71$, 90, 109, 147, 190, 215 and 250 cm.

The introduction to this chapter states that the WA94 experiment concentrated on a certain kinematic region and that this was achieved by modifying the shape of active regions of the MWPCs. This was labelled the 'butterfly' geometry and was designed to select tracks which had $p_\mathrm{T} \geq 0.6$ GeV/c. When the magnetic field is switched off, the locus of tracks which originate from the target, in a plane orthogonal to the beam

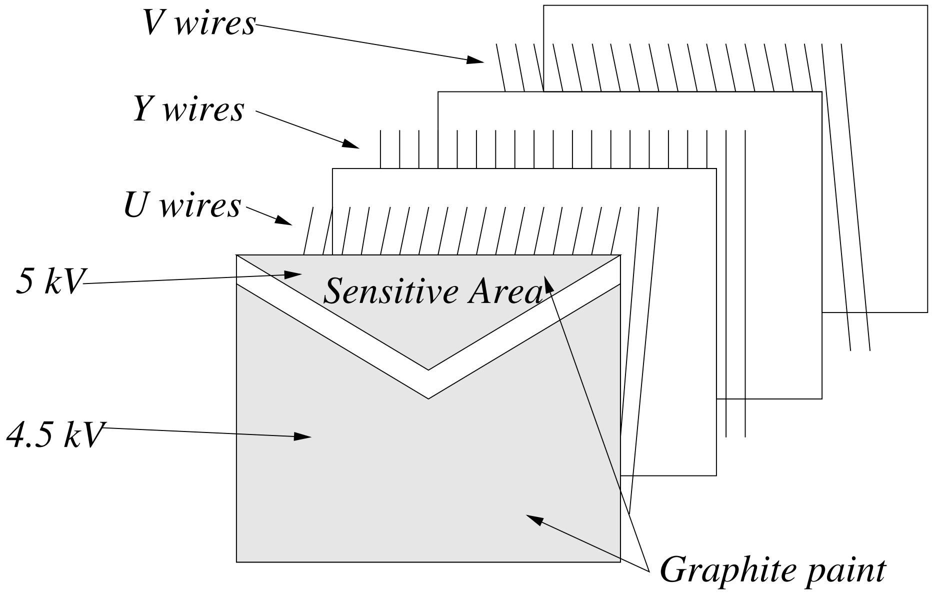

Figure 2.2: View of a section through an Omega A-chamber.

direction, is a circle of radius R. By simple geometry,

$$R = d \cdot \frac{p_{\mathrm{T}}}{p_{\mathrm{L}}}$$

where d is the perpendicular distance from the target plane to the plane under consideration, p_{L} is the longitudinal momentum of the particle and p_{T} is the transverse momentum. This means that for a given p_{T} and x_{Ω}, R is inversely proportional to p_{L} and the loci for tracks of differing p_{L} are concentric. When the magnetic field is switched on, the tracks which have lower p_{L} are swept out further from the beam axis. The locus of tracks for given p_{T} will no longer be a set of concentric circles. The envelope will be two V-shaped regions in the plane in question and thus define the 'butterfly' region as shown in figure 2.3. Thus tracks from the target with $p_{\mathrm{T}} \leq 0.6$ GeV/c cannot enter the shaded region. In fact, only the upper section was used in the experiment. If both sections are used, then the efficiency of the chambers goes down as more hits are recorded in the event.

The A-chambers were made inefficient in the unwanted regions by removing a strip of graphite paint on the cathode planes. The upper 'butterfly' region was held at a

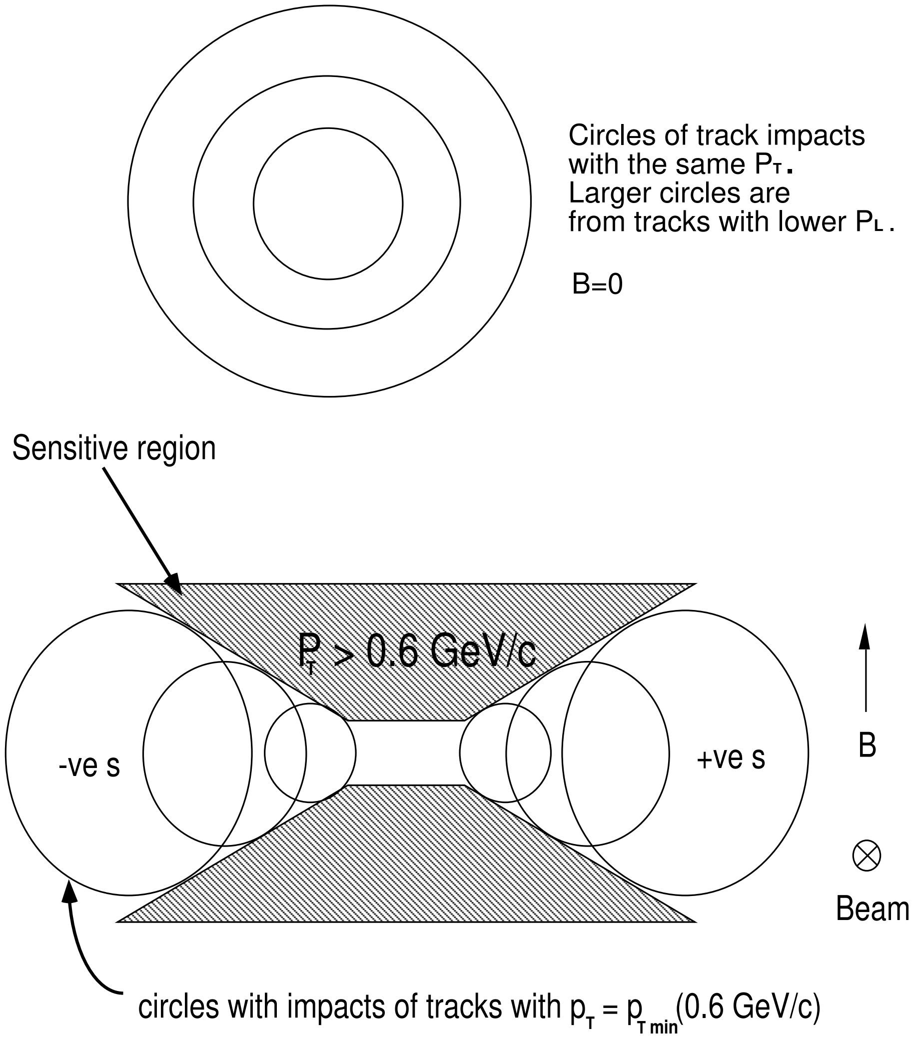

Figure 2.3: Butterfly geometry.

potential of 5kV and the lower, disabled region was held at 4.5 kV. The shape and size of the sensitive regions varies between chambers so that the geometric acceptance is the same in each case. The average number of tracks per event recorded in the sensitive regions of the A-chambers in sulphur–sulphur interactions is around 20. The shapes of the chambers were kept the same for proton–sulphur interactions, in order to keep the same kinematic window, but the average number of tracks per event is below one by using this method, which is useless for efficient detection of hyperon decays, so a good trigger was devised to increase the hyperon detection rate. The trigger shall be described in section 2.6.

2.5.2 The Hodoscopes

There were two arrays of scintillator slabs in this experiment. Each array is known as a *hodoscope*. HZ0, the first hodoscope downstream from the target (at $x_\Omega = 277$ cm) was just past the final A-chamber and inside the OMEGA field region. HZ1, the second hodoscope (at $x_\Omega = 480$ cm) was outside the field. Both hodoscopes consisted of five horizontal slabs, arranged in such a way that particles that passed through the sensitive regions of the A–chamber modules would pass through the hodoscopes. The slabs were split into two logical halves, LEFT and RIGHT as seen by the beam, so that a correlation of hits could be used in the trigger to enhance the hyperon detection rate. This is shown in figure 2.4

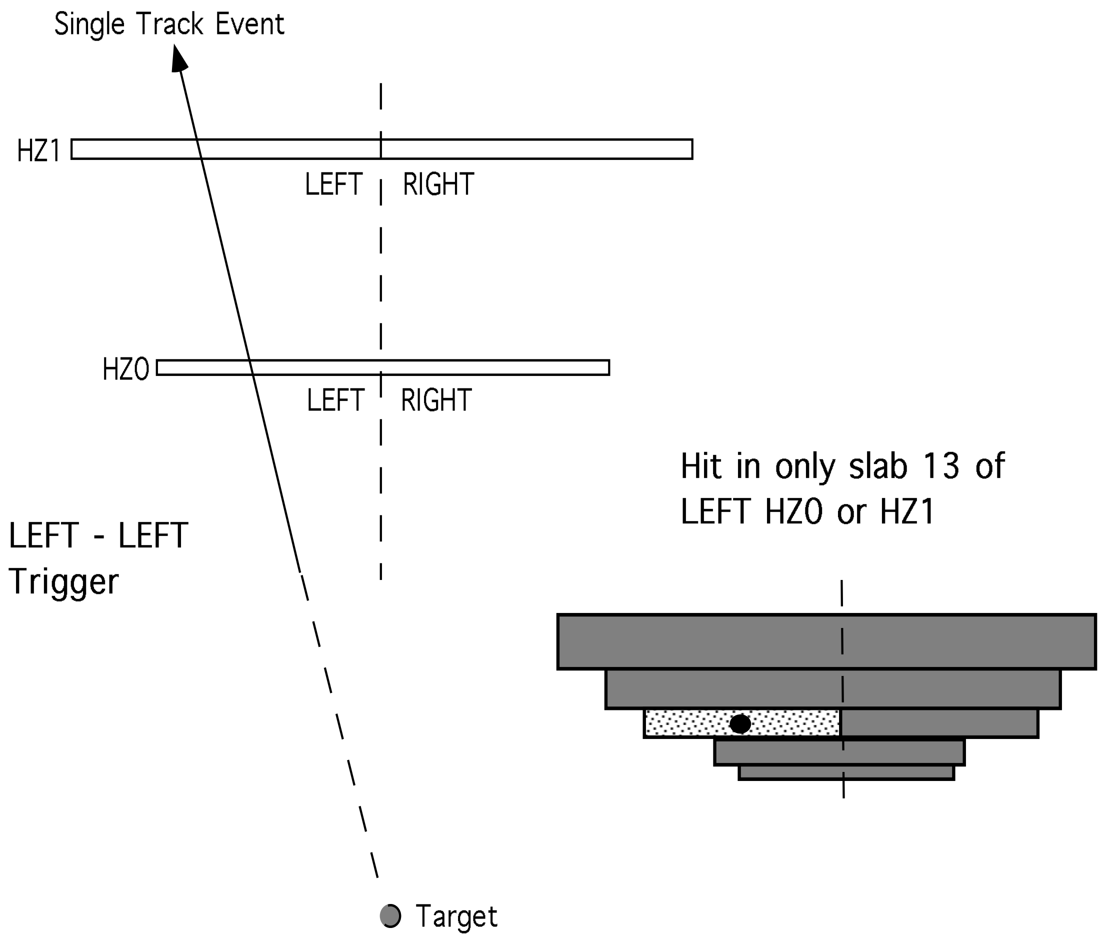

Figure 2.4: Schematic diagram indicating L–L correlation.

2.6 The 1993 Proton Trigger

The aim of any trigger is to select events with characteristics which enhance examples of a given physical process without any bias towards any particular type of triggered event. Figure 2.5 is the trigger diagram for the 1993 proton run and figure 2.6 summarises the trigger stages in a schematic way.

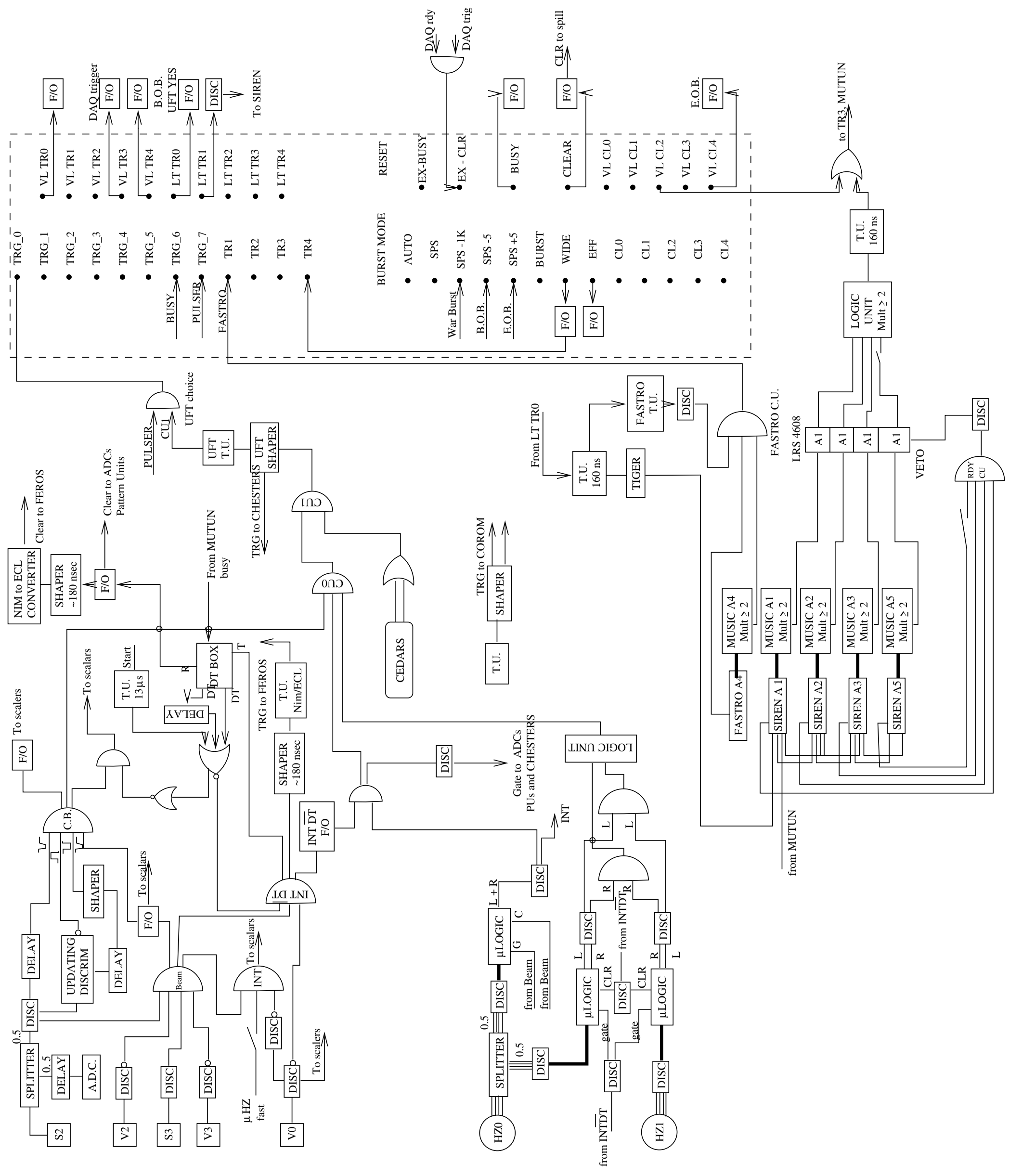

Figure 2.5: Trigger diagram for the 1993 proton-sulphur run.

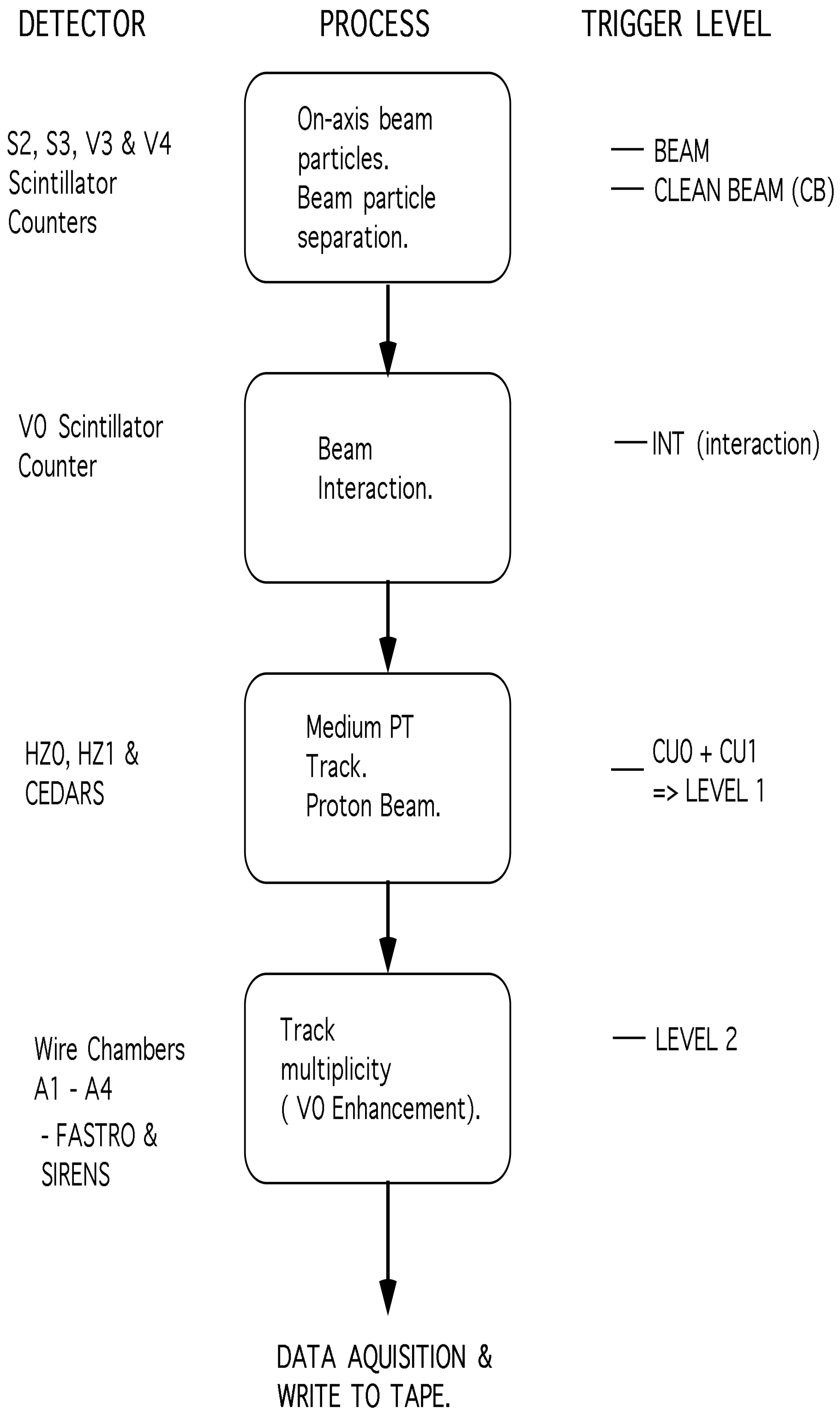

Figure 2.6: Schematic diagram showing trigger stages.

2.6.1 Beam Counters

As the signals from the beam counters are the fastest of all, they are used at the lowest trigger level. There are five simple scintillator counters, labelled S2, V2, S3, V3 and V0 on the layout figure 2.1. S2 and S3 were aligned in the beam and positioned upstream of the target. V2 and V3 were veto counters; they were square with a circular hole in the centre to allow the beam to pass through. The veto counters were also placed upstream of the target and were used to veto particles that were not running truly along the beam axis. The final counter, V0, was placed downstream of the target. If the beam particle interacted with a target particle, it would be deflected away from the beam axis and so should not pass through V0. This is displayed pictorally in the upper part of figure 2.7.

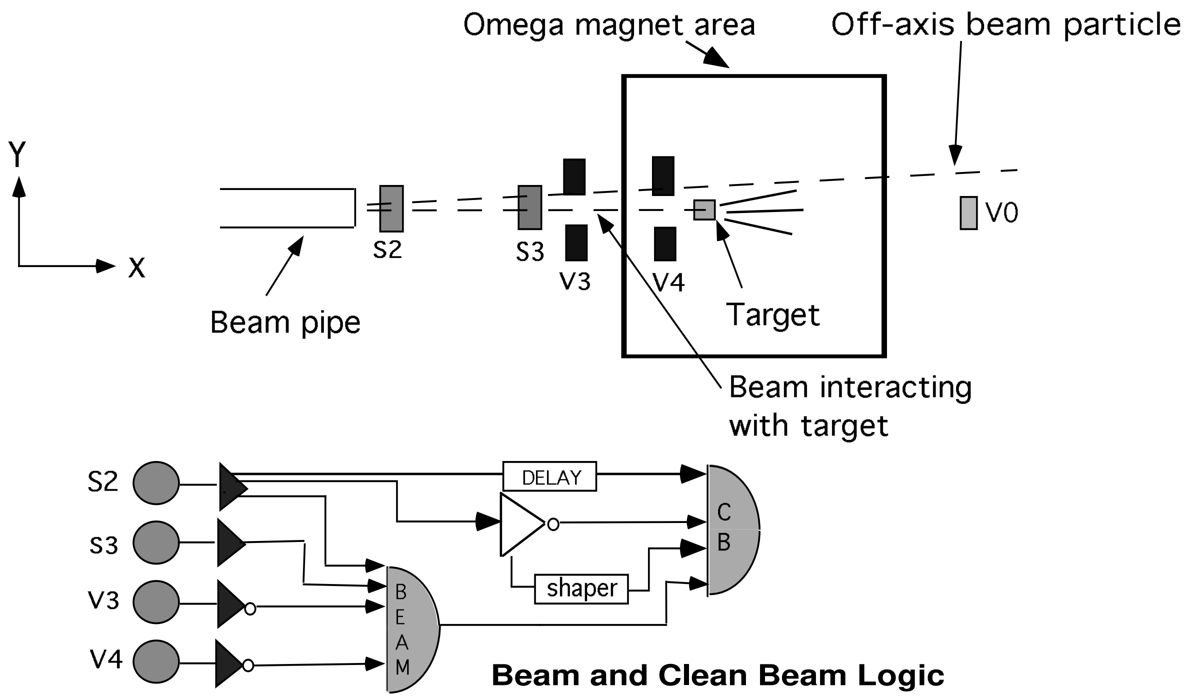

Figure 2.7: Beam Counter Trigger and Layout.

2.6.2 Trigger Logic

The first trigger level is called *BEAM*. There must be a signal from S2 which is in coincidence with a signal from S3. This reduces the possibility of triggering on noise in S2. It can be seen from the trigger diagram that there must be no signal in either V2 or V3. Thus *BEAM* is defined by

$$\mathbf{BEAM} = \mathbf{S2} \cdot \mathbf{S3} \cdot \overline{\mathbf{V2}} \cdot \overline{\mathbf{V3}}$$

The beam logic is shown in the lower part of figure 2.7.

The next step in the trigger logic is *CLEAN BEAM* or *CB*. Clean beam requires that there must be no further signals in S2 in a time interval of 40 ns centred on the interaction time. This would occur if there had been two separate interactions in the target from a pair of beam protons arriving at the target with too small a separation between them. Part of the signal from the S2 counter is passed to an updating discriminator. If a second signal arrives from S2 during the time Δt after the first signal arrives, then the inverse of the signal from the updating discriminator, $\overline{S2_p}$, which is lengthened by Δt, will be in anti-coincidence with S2, BEAM and $S2_{p'}$ and so the event will be vetoed. The delay Δt was set to be twenty nanoseconds. The idea that has been described here, CB, is also known as *past-future protection*. Figure 2.8 shows the input signals to the past-future coincidence unit.

The final step in beam logic is the interaction level, or *INT*. In the beam counter subsection, the counter V0 was mentioned. If this fired, then there had been no interaction between the beam and target particle and so the beam particle had not been deflected away from the beam axis. Thus the INT level requires the absence of a signal in V0.

2.6.3 Level One Trigger

It is at this stage of the trigger that the outputs from the hodoscopes and the CEDARS are fully considered. The hodoscopes were divided into two logical sections each, known as quadrants. They were labelled LEFT and RIGHT as seen by the incoming particle. For the event to pass this stage of the trigger, there must be at least one hit in *both* left halves or *both* right halves of the two hodoscopes. This is known as a LEFT-LEFT and a RIGHT-RIGHT correlation of hits. The main component of the magnetic field is parallel to the OMEGA z-axis, so oppositely charged particles will tend to be swept to opposite halves of the hodoscopes. This condition enhances the chance that an event includes a track of medium to high p_{T} and reduces the probability of triggering on electronic noise. This hodoscope condition entered the trigger at coincidence unit zero (CU0).

The CEDARs enter at coincidence unit one (CU1) even though they are used as part of the beam definition. The CEDARs were tuned to fire if the beam particle that passes through them was a proton. As there were two CEDARs, the outputs were fed into a logical OR gate before being passed to CU1, the output of which was the complete level one stage of the trigger.

2.6.4 Level Two Trigger

The fourth A–chamber, A4 was fitted with a fast read-out and multiplicity determining card called a *FASTRO*. It was therefore possible to measure the multiplicity of this chamber quicker than the other A–chambers. If the multiplicity was less than two then the event was rejected. This saved of the order of two hundred microseconds for each rejected event.

If the event passed this condition, then the read-out from the slower SIREN [50] and MUSIC [51] read-out systems from chambers A1, A2 and A3 were considered. The multiplicity from these chambers was worked out and if the multiplicity from at least two of these chambers was greater than one, then the event passed. This consideration of the chamber multiplicity biases the experiment towards events with two or more tracks in them, so that the detection rate for V^0s and cascades goes up. The multiplicity condition completed the second level trigger.

During the data-taking of the 1993 proton run, data were taken for various levels of trigger. Most of the data was taken at trigger level two, but some was at the trigger level one in order to determine the $\frac{\Lambda}{h^-}$ ratio which is important for enhancement normalisations. Level one data was also taken to determine the efficiencies of the chambers. Second level data without the hodoscope inputs were also taken for the procedure of determining the hodoscope efficiencies.

2.7 Data Acquisition (DAQ) and Off-line Processing

After an event has satisfied the selected trigger requirements, it is written to tape in the machine independent, 16 bit EPIO [52] format in a ROMULUS [53] block structure. A given address would allow access to the information on the wires for any given plane that fired. This tree structure is depicted in figure 2.9.

The data in this raw stage is processed offline by a modified version of the track identification program TRIDENT [53]. The program uses the independent information from the three planes in each chamber to build up tracks. A fitting routine then produces a three-dimensional track. A hit, or *space point* is counted when there is a cluster in the Y-plane and at least one other plane in the same chamber.

The data taken using each of the two field polarities were used to determine the alignment of the wire planes. The shifts from the nominal positions are in the order of microns. These small corrections are added into the track reconstruction and momentum fitting.

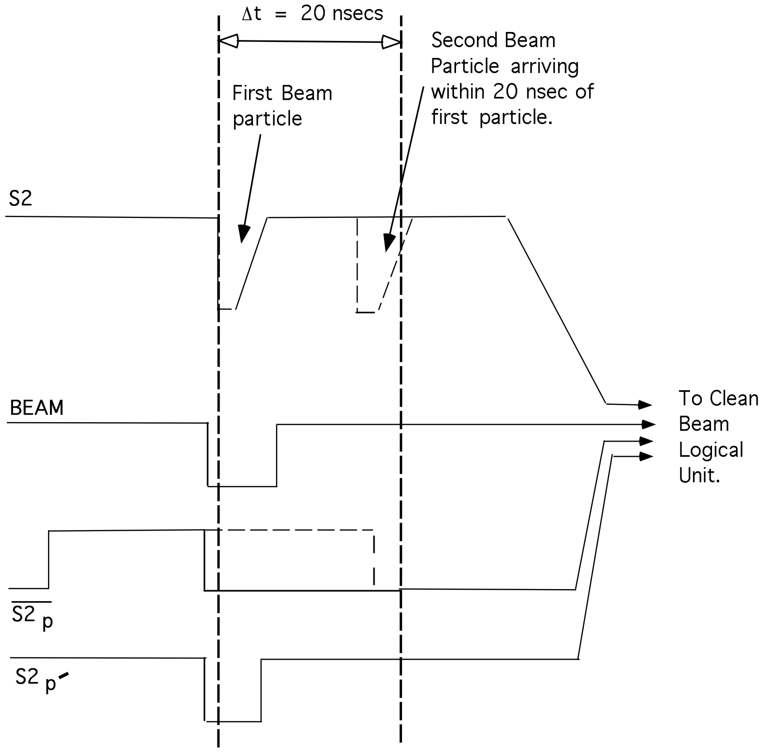

Figure 2.8: The input and output signals to the past-future protection coincidence unit.

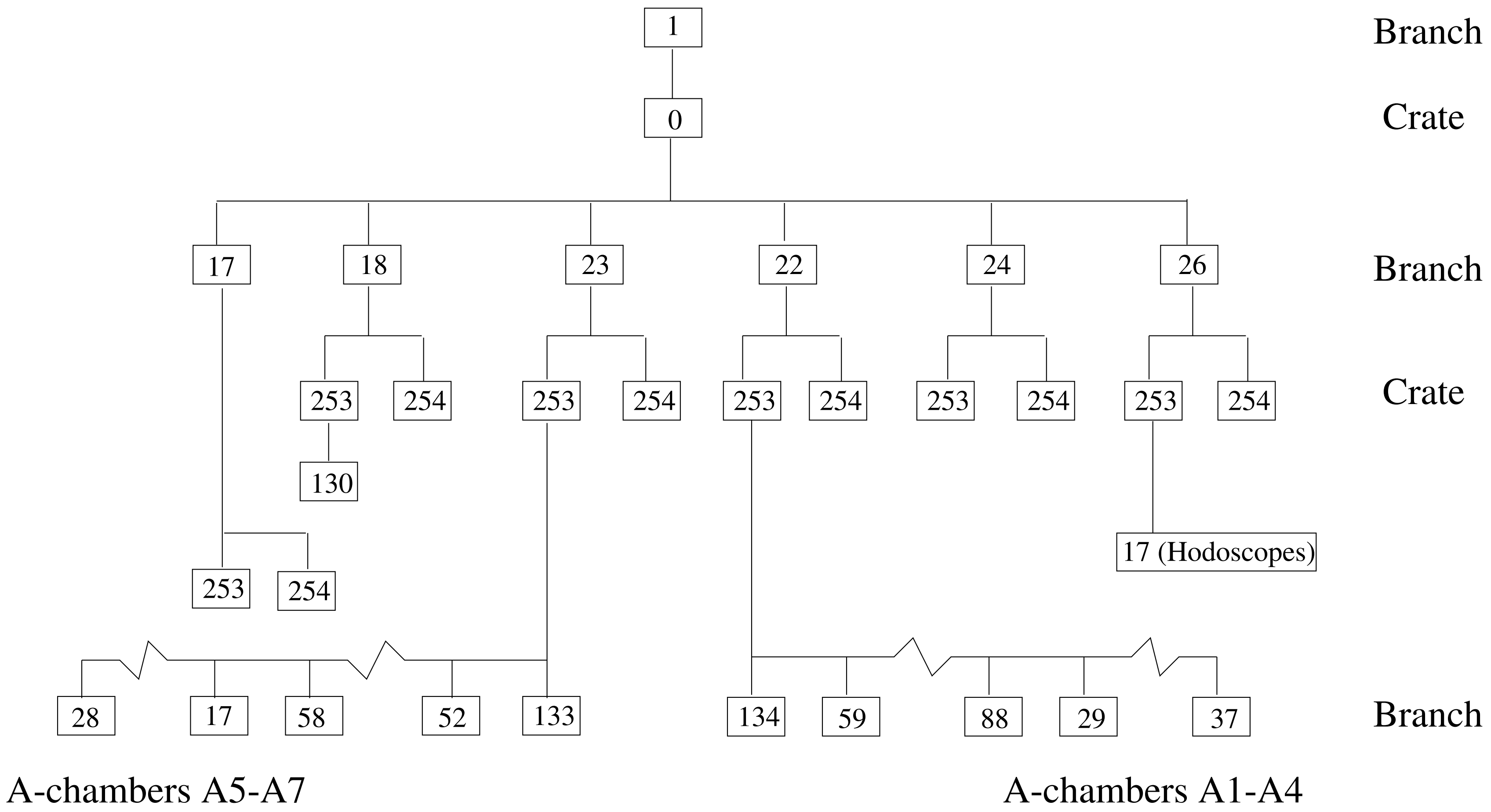

Figure 2.9: ROMULUS block data structure.

Chapter 3

Reconstruction of Λ and Ξ^- Decays

As has already been mentioned, the WA94 collaboration performed an experiment at the OMEGA spectrometer using a proton beam (from the SPS at CERN) incident on a sulphur target. This is a control experiment because the relative yields of strange hyperons and anti–hyperons can be compared with those from the sulphur beam, sulphur target experiment which was performed in 1991. The hyperons that the experiment was designed to look for are Λs and Ξ^-s; they are identified by reconstructing the tracks from the weak decays

$$\Xi^- \to \Lambda + \pi^-$$

and

$$\Lambda \to \mathrm{p} + \pi^-$$

and the charge conjugate decays.

The signature for a Λ decay is, therefore, two oppositely charged tracks intersecting. Similarly, the signature for a Ξ^- decay is a charged track that intersects the path of a Λ.

3.1 V^0 Reconstruction

The track identification program TRIDENT reconstructs tracks from the hits recorded in the A-chambers. In order to find V^0s, the TRIDENT output data are passed to a program called STRIPV0 which uses a NAGLIB [54] minimising routine to find the closest point of approach of oppositely charged tracks. This program also performs some very loose cuts on the data sample in order to produce a data summary tape (DST) of V^0 candidates. Figure 3.1 shows a schematic diagram of a V^0 decay.

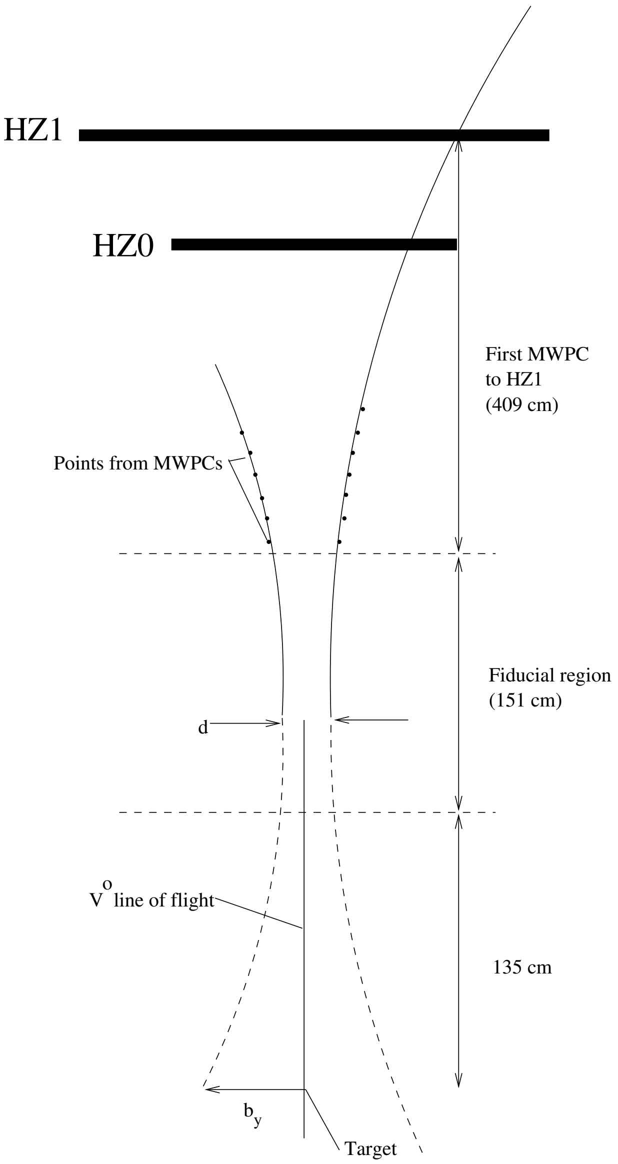

Figure 3.1: Schematic diagram showing a Λ decay.

All of the tracks are traced back from the A-chambers to the $x_\Omega = 0$ cm plane. This is the position where the OMEGA magnetic field is the most uniform. The tracks are then modelled as helices and the distance of closest approach is calculated for each pair of oppositely charged tracks. This distance has to be less than 1.6 cm for the candidate to be considered further.

The V^0 vertex is defined to be half way along the line joining these two points. This vertex position must lie between $-115 < x_\Omega < 71$ cm for the candidate to proceed to the next cut. The acceptance decreases for V^0s that decay a long way away from the A–chambers while the combinatorial background from tracks from the target increases. The upper limit is the x_Ω position of the first A-chamber. The decay tracks of those candidates that decay after this position will not trace through all the A-chambers, reducing the ability of TRIDENT to give accurate measurements of the decay particle's momentum.

The transverse momentum of each decay particle with respect to the momentum vector of the V^0 candidate, q_T, must be less than 0.3 GeV/c for the V^0 to proceed as a good candidate. This cut is employed to reduce the background from a crossing of oppositely charged tracks that come from the target instead of a V^0 decay. The final cut is that the momentum of the V^0 candidate must be greater than 6.5 GeV/c because the geometric acceptance is very small for real V^0s below this momentum. Λs recorded by the chambers have a mean momentum of about 10 GeV/c.

Figure 3.2 shows that even after these loose cuts, there is a clear peak in the effective mass M(pπ^-) distribution of V^0 candidates at the Λ mass. As a quality control on the momentum definition of the decay tracks, a cut is put on the number of space points that each decay track possesses. Each track must have at least four space points. If this is not the case, then the track's curvature and hence its momentum is poorly defined.

There is another condition that must be satisfied because it is part of the trigger requirement. The hodoscope condition requires that at least one decay track must trace through corresponding quadrants of the hodoscopes, *i.e* one track must pass through

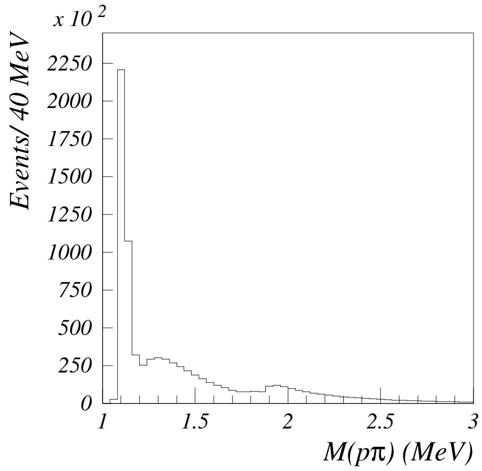

Figure 3.2: Effective pπ^- mass distribution after STRIPV0.

both right hand sides or both left hand sides of the two hodoscope planes. This is called a RIGHT-RIGHT or a LEFT-LEFT correlation respectively. The effect of enforcing this condition is to lose about two percent of the data, but the trigger requirements of the analysis chain must match those of the experiment itself and thus those of the acceptance calculations.

Both of the decay tracks from the Λ must trace through each of the seven A-chambers. The region within one centimetre of the edge of the chamber is inefficient and events with tracks that fall in this area are rejected. This reduces systematic errors.

Figure 3.3 a) shows the vertex distribution of those events that have satisfied the cuts made by STRIPV0. A direct comparison with the same distribution from the Monte Carlo acceptance program (figure 3.4) reveals that there is an excess in the region furthest away from the A-chambers in the real data and also at the position of the first A–chamber. The shape of the Monte Carlo distribution is a convolution of two effects. Firstly, there is an exponential decay length for Λs of given momentum [1] so most of them decay well upstream of the chambers. Secondly, those Λs that decay

[1]The transverse momentum spectrum was assumed to be proportional to $\frac{1}{m_{\mathrm{T}}^{3}/2}e^{-m_{\mathrm{T}}/\beta}$, where β is taken from fit to the acceptance corrected real data.

nearer to the first A-chamber are more likely to have both tracks passing through all seven chambers and so have greater acceptance. The excess is due to oppositely charged tracks coming from the target, which cross downstream and create fake Λ candidates. Figure 3.3 b) shows the distribution of the vertex position of the V^0 candidates against their effective mass. The excess at the position of the first A–chamber is due to γ conversions in the material of the chamber. The cut on vertex position $-80 < x_\Omega < 71$ cm reduces the number of candidates but increases the signal to background ratio.

One other cut performed by STRIPV0 is tightened in the final analysis program. Most of the candidates also pass a tightened distance of closest approach cut. This distance was reduced from the STRIPV0 maximum of 1.6 cm to 1.0 cm.

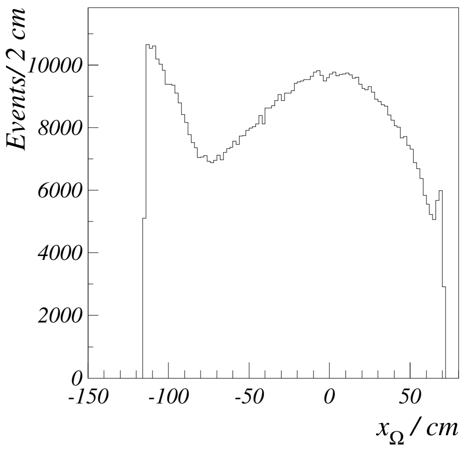

(a)

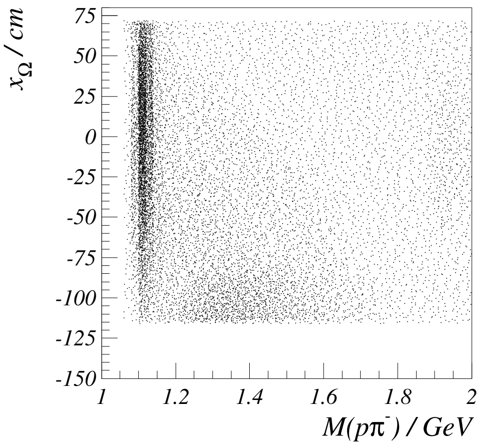

(b)

Figure 3.3: a) Λ vertex distribution. b) Λ vertex distribution plotted against effective M(pπ^-).

Three new cuts are introduced at this stage. A reduction in the maximum allowable angle between the V^0's line of flight and the sum of the three-momenta of the decay particles to 0.75° does not reduce the number of candidates significantly. It means, however, that the object from which the decay particles originated did indeed came from the target. The q_T (figure 3.5) distribution shows that there is a high- and a low-

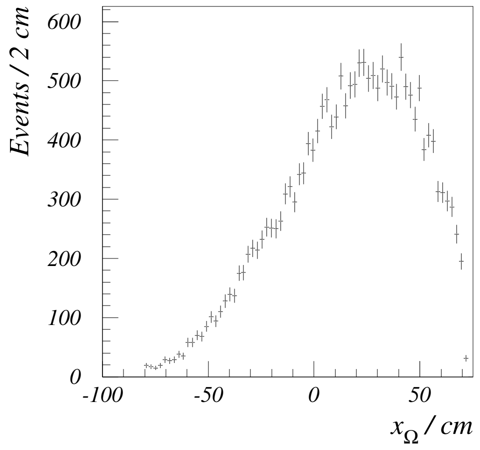

Figure 3.4: Monte Carlo vertex distribution for Λs.

q_T background to the Λs. The events at low-q_T are generally from photon conversion into e^+e^- pairs and those from high-q_T come from K^0 decaying into two pions. The low-q_T background is removed by a simple cut ($q_T < 0.01$ GeV/c). To reduce the K^0 background requires a more subtle approach involving the Armenteros-Podolanski variable, α [55].

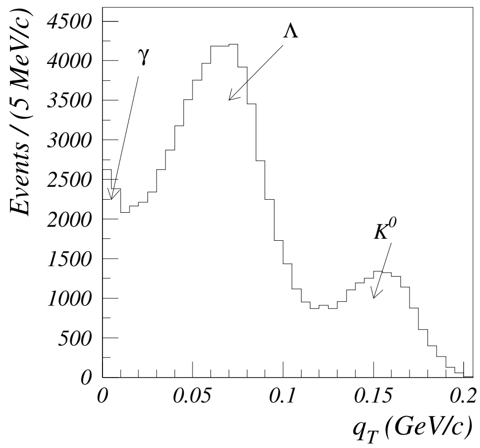

Figure 3.5: q_T distribution after STRIPV0.

By forming a variable which is a function of the the longitudinal components of the decay particles' momenta with respect to the V^0 momentum and observing this new variable's correlation with q_T it is possible to distinguish Λs and K^{0}s to a large degree. The Armenteros-Podolanski variable α is defined by the relation

$$\alpha = \frac{q_L^+ - q_L^-}{q_L^+ + q_L^-}$$

where q_L^+ and q_L^- are the momentum components, parallel to the the V^0 momentum, of the positive and negative decay particles respectively. Further discussion of the α variable and its relation with q_T can be found in appendix A; figure 3.6 a) is the Armenteros-Podolanski plot for V^0s from STRIPV0. The theoretical loci in this plane for K^0 , Λ and $\overline{\Lambda}$ are shown in appendix A. Figure 3.6 b) shows the Armenteros-Podolanski plot for the V^0 candidates after all the other cuts have been applied.

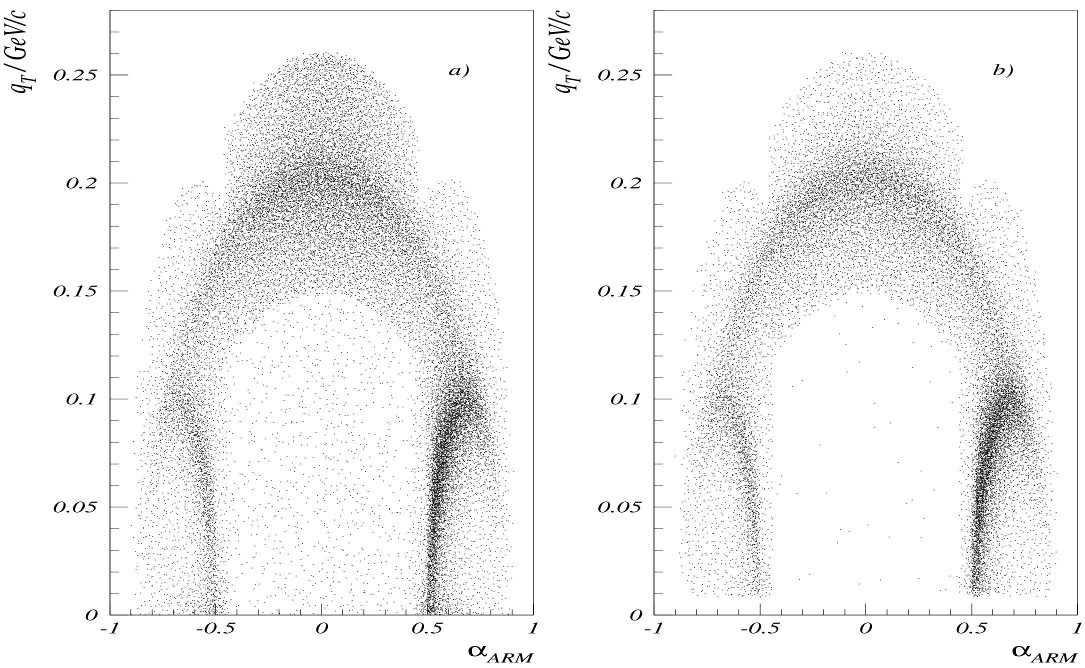

Figure 3.6: Armenteros-Podolanski plot a) from STRIPV0 and b) after cuts.

In order to define a set of Λ and $\overline{\Lambda}$ candidates in a specific kinematic window, there is a cut on α, namely Λs and $\overline{\Lambda}$s which have $0.45 < |\alpha| < 0.6$, and are thus unambiguous inside a 50 MeV mass cut. This is equivalent to a cut in the cosine of the decay angle in the centre of mass frame.[2] It has been found that the ratio of numbers of $\overline{\Lambda}$ and Λ

[2]This angle is defined to be the angle between the lines of flight of the V^0 and of the decay proton

does not vary as a function of $|\alpha|$ above 0.6. Even after performing this cut, there is still some risidual contamination of K^0 in the Λ and $\overline{\Lambda}$ samples. This contamination is estimated to be around 1% for the Λ and 2% for the $\overline{\Lambda}$. This calculation is described later on in chapter seven.

The kinematic region of acceptance is defined in chapter five. Only reconstructed V^0 decays which lie in the region where the acceptance is greater than 10 *per cent* of the maximum value are considered. This is defined as the region of *good* acceptance. The last condition that the candidate has to satisfy is that the reconstructed mass must lie in a mass interval 50 MeV wide centred on the PDG value for the Λ mass (1.1156 GeV) [29], *i.e.* $1.09 < M_{cand} < 1.14$ GeV.

3.2 Ξ^- and $\overline{\Xi}^+$ Reconstruction and Selection

The events that have passed the loose cuts in STRIPV0 are passed on to a further program, STRIPXI, to find cascade particles. Events with Λ candidates and an extra negatively charged particle and events with $\overline{\Lambda}$ candidates and a extra positively charged particle are tested to see whether the extra particle intersects the line of flight of the V^0. Figure 3.7 is a schematic diagram illustrating a cascade decay. This new program imposes some more preliminary cuts on the V^0 candidate. $|\alpha|$ must be above 0.4 and the effective mass must lie within 40 MeV of the PDG Λ mass.

The distance of closest approach between the V^0's path and the extra track is a further loose cut. This extra parameter must have a value less than 3 cm. In addition, the cascade vertex must appear in the fiducial region $-220 < x_\Omega < 71$ cm.

The cascade candidates must satisfy criteria of a similar nature to those used on the Λ candidates. Just like in the Λ case, each of the three selected tracks must have at least four space points, for reasons of momentum and track definition. Each track must also trace through the first four A-chambers, missing the edges by at least 1 cm.

in the V^0 rest frame.

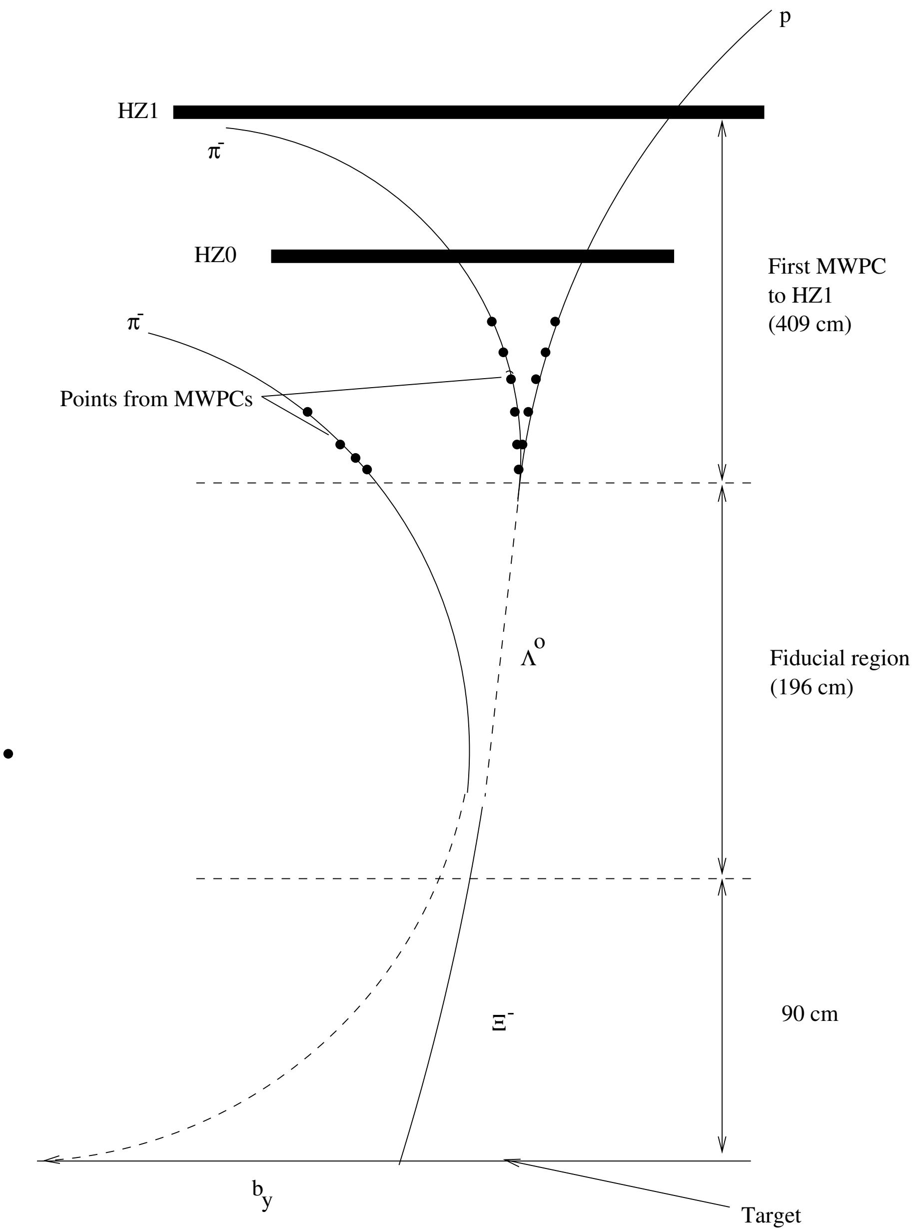

Figure 3.7: Schematic diagram showing a Ξ^- decay.

One of the tracks must satisfy the same hodoscope condition too (see section 2.5.2).

The final selection cuts for the V^0 candidates from a cascade candidate are slightly relaxed in comparison to those for the Λ final cuts. Firstly, the vertex must lie in the region $-115 < x_\Omega < 71$ cm. Secondly, the distance of closest approach of tracks from the V^0 decay particles is required to be less than 1.6 cm. Finally, the tracks from the V^0 decay must have q_T less than 0.14 GeV/c. The condition that the V^0 points back to the target is not required for the cascade selection.

The acceptance for Ξ^- drops with increasing distance between the decay vertex and the A-chambers. This is exactly the same effect as in the case of the Λ decays. Figure 3.8a) shows the vertex distribution of the real raw Ξ^- candidates after passing through the loose cuts of STRIPXI and figure 3.8b) shows the same distribution after all of the cuts are made.

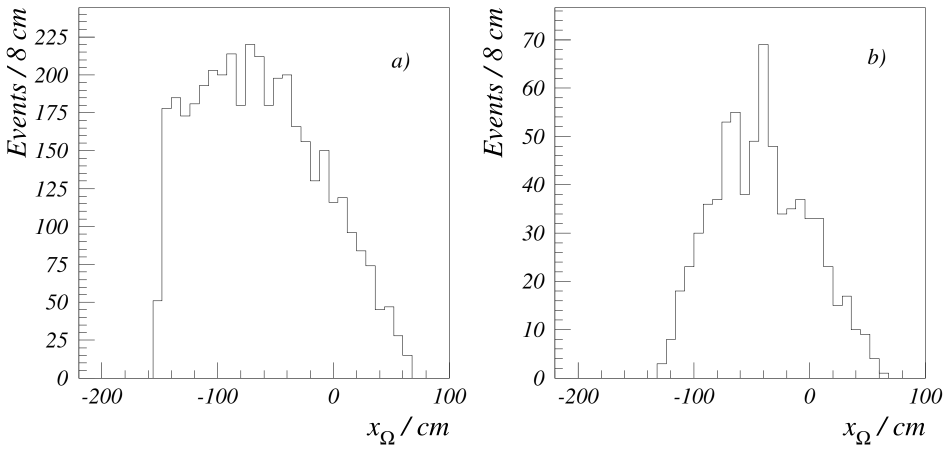

Figure 3.8: Cascade vertex distribution for a) STRIPXI candidates and b) after all cuts.

It does not make sense to consider candidates whose Λ vertex occurs further upstream than the Ξ^- vertex. Hence there is a causality cut, which expressed mathematically is

$$x_\Omega(V^0) \geq x_\Omega(\Xi^-).$$

Smearing of the Λ and Ξ^- vertices will, however, result in the loss of some of the genuine Ξ^- particles. The reconstruction efficiency calculation accounts for this loss.

The cut on the distance of closest approach, *dclose* , between the line of flight of the V^0 and the extra track in the event is also tightened, just as in the case of the V^0 candidates. The distributions of *dclose* for (a) candidates written out to tape after the loose cuts of STRIPXI and (b) candidates after all other cuts are shown in figure 3.9. The maximum distance for good candidates is 2.0 cm.

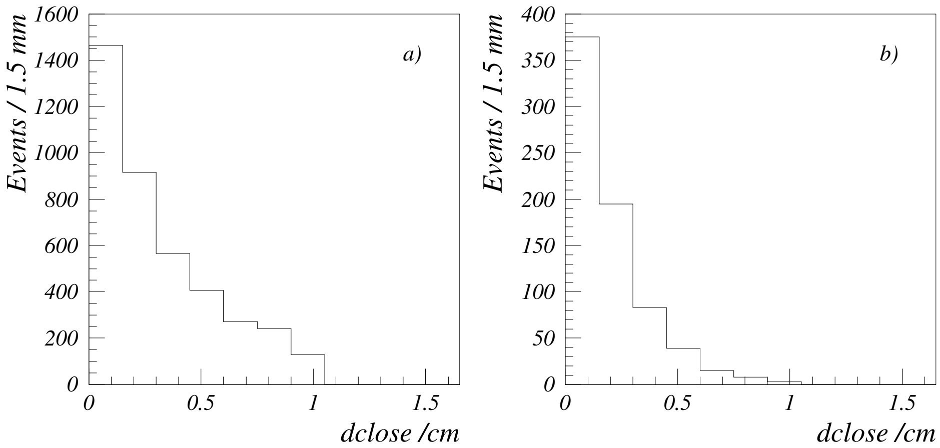

Figure 3.9: Distance of closest approach for a) STRIPXI candidates and b) after all cuts.

A good check of the reconstruction procedure is to trace the candidates back to the target plane. The distributions of impact parameter[3] after all other cuts are shown in figure 3.10. As can been seen, there is a strong peak in the region around zero, which shows that the procedure works well.

The cut that reduces the background most severely is a cut on the impact parameter of the pion from the Ξ^- decay. Most of the background comes from spurious charged tracks from the target intercepting the line of flight of the V^0 candidate. A pion from a genuine Ξ^- decay does not, in general, come from the target, so when it is traced back to the target plane, its impact parameter should, on average, be quite large. Figure 3.11a) shows the drastic nature of a cut on the pion impact parameter. A large proportion of the bad candidates have an impact parameter of less than 6 cm as shown by a Monte Carlo simulation (see figure 3.11b)), so it is here that the cut is made.

[3]This is the distance in the OMEGA bend- (y-) direction between the target and the point where the candidate hits the target plane when it is traced backwards

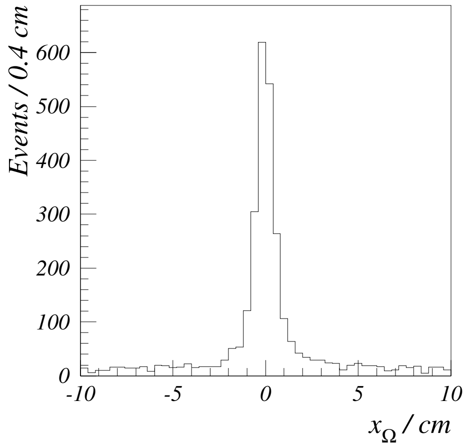

Figure 3.10: Cascade candidate impact parameter after all other cuts.

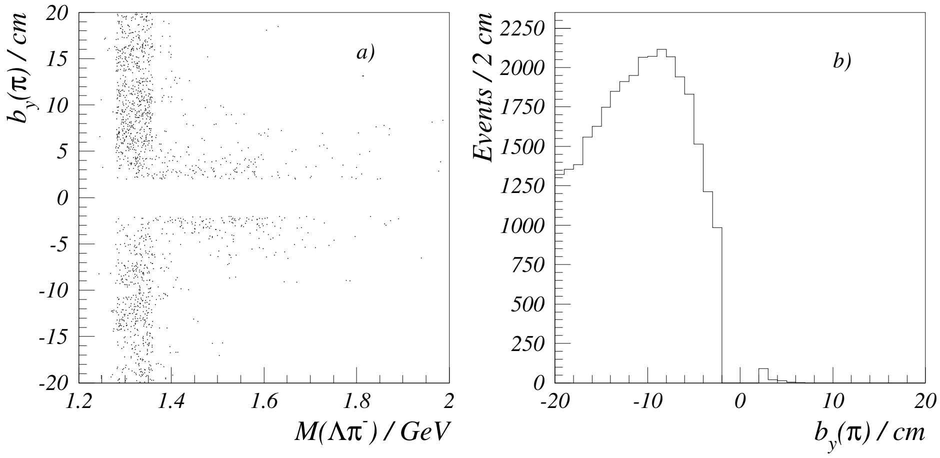

Figure 3.11: a) Impact parameter of the cascade decay pion plotted against candidate mass and b) impact parameter of cascade decay pion from a Monte Carlo simulation.

The final cut is that the candidate should have a mass within 50 MeV of the accepted Ξ^- mass (1.321 GeV [29]). Of course, only those candidates in the correct kinematic region as defined earlier are considered for further analysis.

3.3 Summary of Cuts for Λ Reconstruction

1. Each decay particle track has at least four space points.

2. Each decay particle track traces through all seven A-chambers, not including a 1 cm band around the edges of the chambers.
3. At least one of the tracks from the decay particles satisfies the LEFT-LEFT or RIGHT-RIGHT hodoscope trigger condition.
4. The V^0 candidate must have a momentum greater than 6.5 GeV/c.
5. The tracks of the two decay particles approach within 1 cm of each other.
6. The angle between the V^0's line of flight and the sum of the three momenta of the decay particles is less than 0.75°.
7. q_T is greater than 0.01 GeV/c.
8. The V^0 vertex lies in the region described by $-80 < x_\Omega < 71$ cm.
9. For Λs, $0.45 < \alpha < 0.6$ and for $\overline{\Lambda}$s, $-0.60 < \alpha < -0.45$.
10. The effective mass lies in a 50 MeV range centred on the PDG mass of the Λ.
    i.e. $1.09 < M_{cand} < 1.14$ GeV/c

Figure 3.12 shows effective proton–pion mass distributions for the 1993 proton-sulphur run after cuts a) 1 to 4, b) 1 to 7, c) 1 to 8 and d) 1 to 9. The lines on figure 3.12d) shows cut 10. Even after the loose cuts, there is a clear peak at the Λ mass. After all cuts, there is little background.

3.4 Summary of Cuts for Ξ Reconstruction

1. Each decay particle track has at least four space points.
2. Each decay particle track traces through A-chambers A1 to A4, not including a 1 cm band around the edges of the chambers.
3. At least one of the tracks from the decay particles satisfies the LEFT-LEFT or RIGHT-RIGHT hodoscope trigger condition.
4. At the V^0 vertex, the distance of closest approach is less than 1.6 cm.

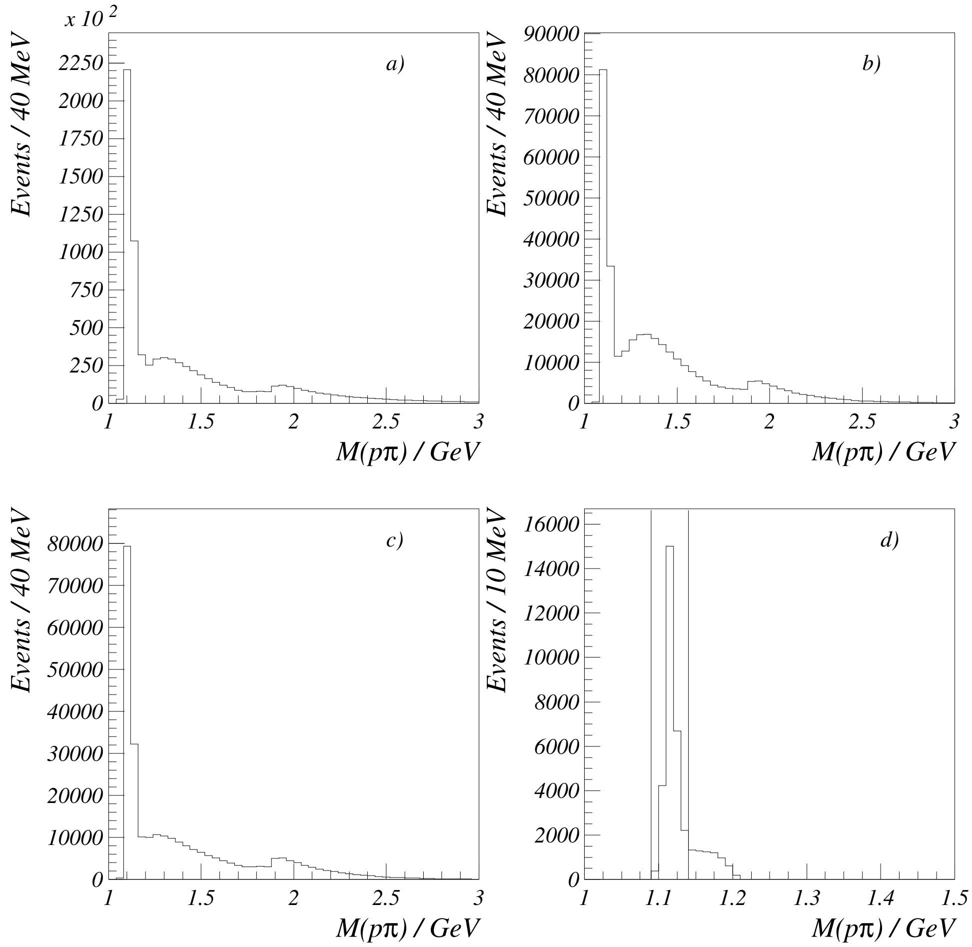

Figure 3.12: Effective M(pπ) distributions after a) cuts 1 to 4, b) cuts 1 to 7, c) cuts 1 to 8 and d) cuts 1 to 9. The lines in d) show cut 10.

5. The V^0 vertex lies in the region described by $-115 < x_\Omega < 71$ cm.
6. $|\alpha| \geq 0.4$
7. $q_T \leq 0.14$ GeV/c
8. The effective mass of the V^0 falls in the interval 80 MeV wide centred on the accepted value of the Λ mass.
9. The distance of closest approach between the 'extra' pion and the line of flight of the V^0 is less than 2.0 cm.
10. The V^0 vertex is further downstream from the target than the cascade vertex.

11. The cascade vertex is in the region described by $-125 < x_\Omega < 71$ cm.
12. When the cascade candidate is traced back to the target plane, its impact parameter is less than 2.0 cm.
13. The impact parameter in the target plane of the first pion is greater than 6.0 cm.
14. The effective mass of the cascade candidate is within 50 MeV of the PDG Ξ mass.

Figure 3.13 shows the effective $\Lambda\pi$ mass distribution after four stages in candidate selection. There is a very clear peak with little background.

3.5 Λ, $\overline{\Lambda}$, $\Xi^-$and Ξ^- Raw Yields

The complete selection procedure yielded the results shown in table 3.1. The numbers of Λs and $\overline{\Lambda}$s are uncorrected for 'feed-down' of Λs coming from the cascade decays. The 'feed-down' fraction is greater for $\overline{\Lambda}$ than for Λ and is described in chapter seven.

The yields give uncorrected ratios of

$$\frac{\overline{\Lambda}}{\Lambda} = 0.266 \pm 0.005$$

and

$$\frac{\Xi^+}{\Xi^-} = 0.41 \pm 0.04.$$

These ratios (after 'feed-down' corrections) will not change much after correcting for reconstruction efficiency and acceptance, since the experiment is charge–symmetric. In order to calculate ratios involving different species, however, it is necessary to include these corrections. Acceptance and reconstruction efficiency will be described in chapters five and six.

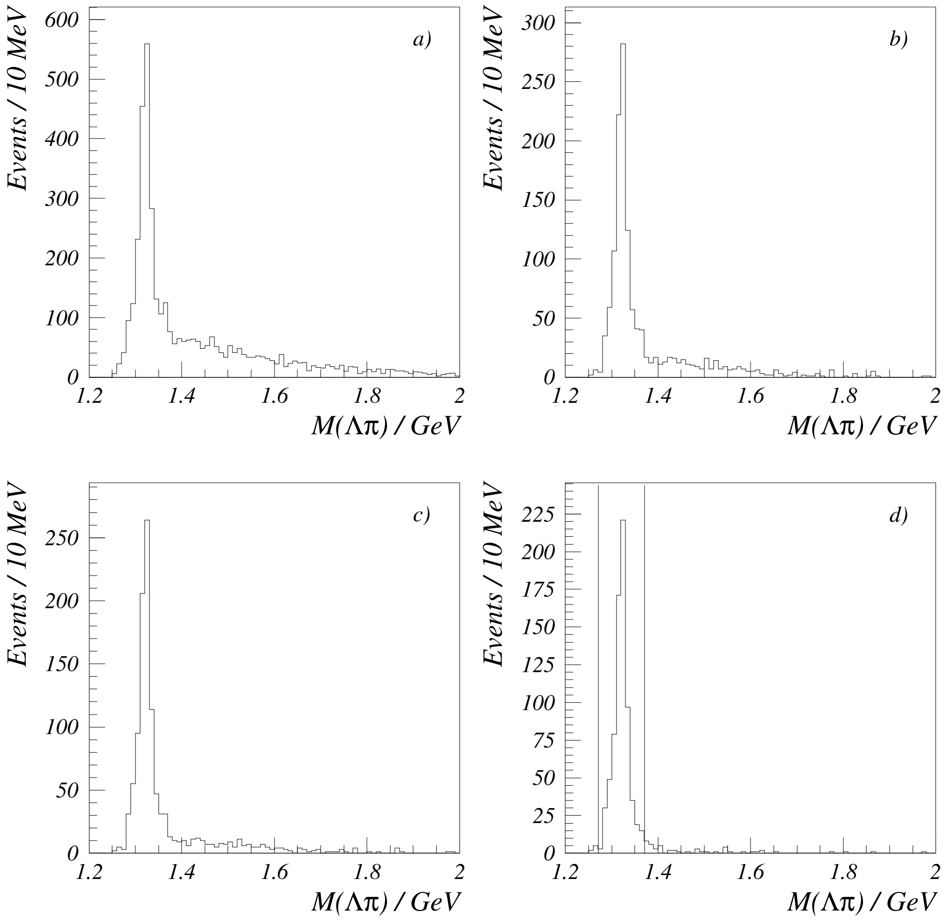

Figure 3.13: Effective M($\Lambda\pi$) distributions after a) STRIPXI, b) cuts 1 to 11, c) cuts 1 to 12, d) cuts 1 to 13. The lines in d) show cut 14.

Table 3.1: Level two hyperon yields for full statistics and for both field polarities.

Particle Species	Field		Total
	Up	Down	
Λ	7782	4064	11846
$\overline{\Lambda}$	2031	1116	3147
Ξ^-	317	133	450
$\overline{\Xi}^+$	125	60	185

Chapter 4

Charged Kaon and Negative Particle Reconstruction

The study of strange and non–strange meson production is of interest to the heavy ion physics community. One idea states that mesons might well equilibrate at a different time from hyperons. Negative particle yields also seem to be a good way of normalising hyperon yields from different collisions.

4.1 Reconstruction of Charged Kaons

Charged kaons decay *via* the weak, so–called 'tau' decay

$$K^+ \rightarrow \pi^+\pi^-\pi^+$$

with a branching ratio of 5.59% . This topology is similar to the cascade decay ($\Xi^- \rightarrow \Lambda\pi^- \rightarrow p\pi^-\pi^-$). For this reason, the cascade finding program was modified to look for K decays instead of Ξ^-decays.

The program looked for the signal of a charged pion coming from an apparent $V^0 \rightarrow \pi^-\pi^+$ and used two cuts early on to remove contamination from Λ and $\overline{\Lambda}$ decays.

The first cut was the requirement that the two pion object was less than 420 MeV. The second of the two initial cuts was the Armenteros–Podolanski variable α was required to lie in the range $|\alpha_{V^0}| < 0.45$.

As mentioned previously, the data summary tape–writing program made cuts to reduce the background for Λ reconstruction. In particular, a momentum cut of 6.5 GeV/c was imposed since real Λs have momentum greater than this. Results have been presented elsewhere [56] for sulphur–sulphur interactions on K meson reconstruction using these tapes. A Monte Carlo study has shown that around half of the Ks will have momenta less than 6.5 GeV/c, and at present, new data summary tapes are being analysed. The momentum cut was removed, however, when the proton–sulphur data summary tapes were remade in late 1996.

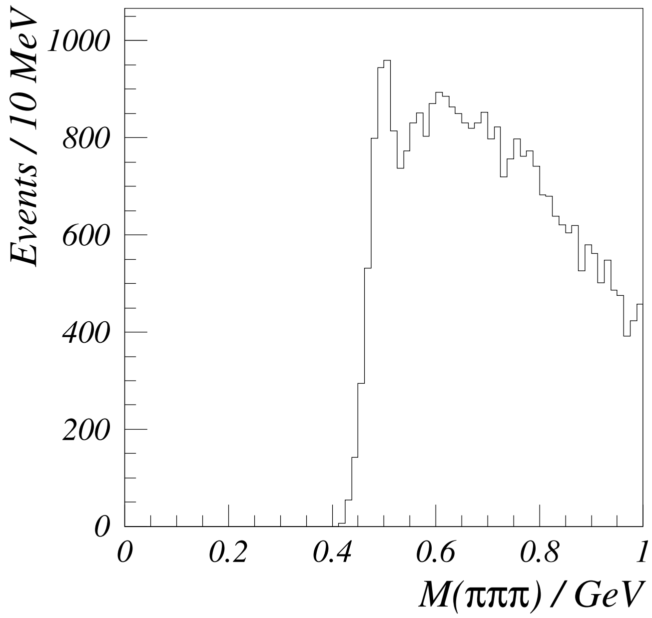

Figure 4.1: Three pion invariant mass after initial cuts.

Just as in the case of the cascade reconstruction, each track from a decay particle is required to pass through the first four MWPCs and have at least four space points. One track must also satisfy the LEFT–LEFT or RIGHT–RIGHT correlation of hits mentioned in the previous chapter. The effective mass of the three pion object, after these initial cuts is shown in figure 4.1. Even with these cuts, there is a clear peak at the mass of the $K^{\pm}$.

4.2 Further cuts applied to the $K^{\pm}$ sample

Despite displaying a clear peak in the three pion invariant mass distribution, figure 4.1 also shows that there is a lot of three track combinatorial background. Figure 4.2, a plot of decay vertex position versus the three pion effective mass, shows that these false combinations predominantly come from a region between the target and $x_\Omega = -55$ cm. For this reason, the decay vertex is required to lie in the region $-55 < x_\Omega < 71$ cm.

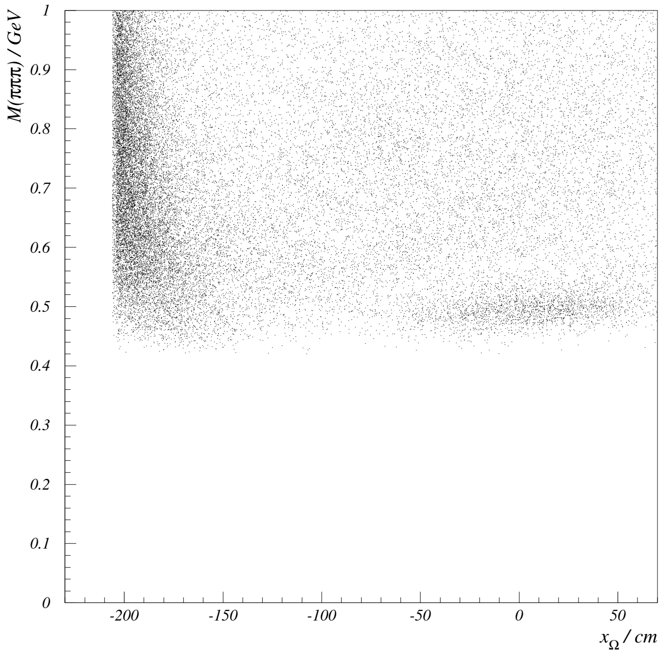

Figure 4.2: Three pion invariant mass plotted against kaon vertex position.

When the kaon has been reconstructed it should be shown to have come from the target. $K^{\pm}$ candidates have their momentum defined from the decay tracks and are then traced back to the target. Figures 4.3a) and 4.3b) show the $y-$ and $z-$impact parameters at the target plane respectively. Only candidates that lie within 2.0 cm of the target are selected for further analysis.

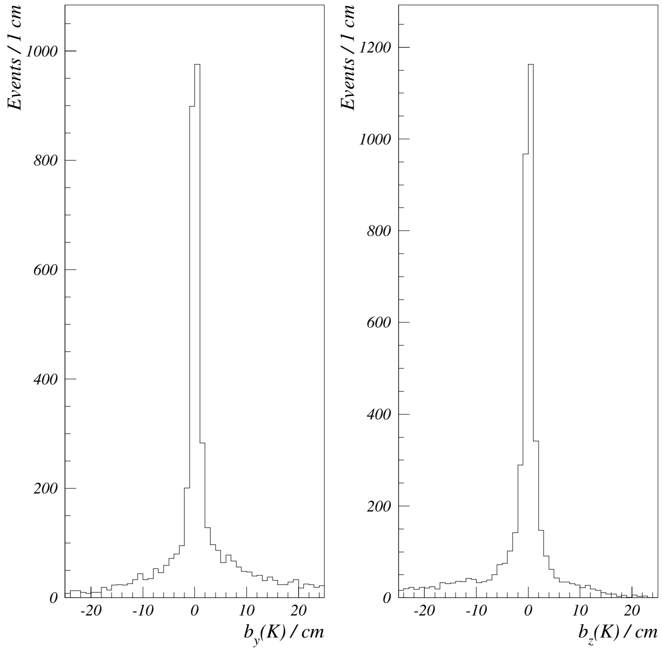

Figure 4.3: Impact parameters at the target plane for the a) $y-$direction and b) $z-$direction.

Whilst it is clear that the candidate should trace back to the target, it is also clear that the decay tracks should not come from the target. Figure 4.4 shows the impact parameter, at the target plane, of the decay tracks plotted against the effective three pion mass. The high–mass background can clearly be seen in cases where the pion impact parameter is less than 5.0 cm, where one of the three tracks has come from the target instead of a kaon decay vertex.

In the cascade topology case, it was important that the two vertices were distinct. In the 'tau' topology case, however, the reverse is true. Figure 4.5 shows how tracks recorded in the MWPCs and traced backwards towards the target could be reconstructed to form a charged kaon. The tracks forming the V^0 cross twice. The line–of–flight of the V^0 and the track of the extra pion also cross twice, but there may be some ambiguity as to which of these two crossings is the real decay point of the kaon. These crossing points are calculated and the four distances between the third

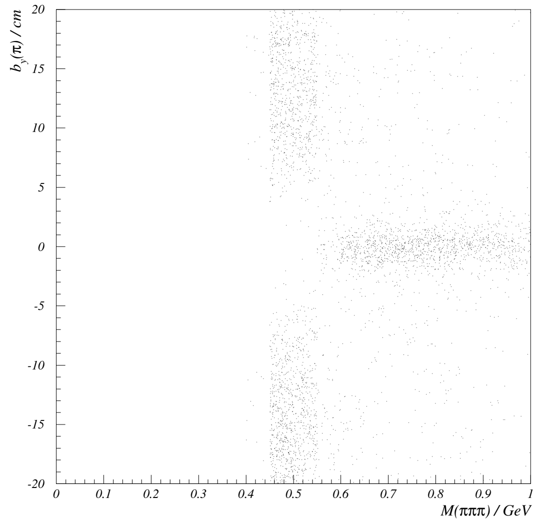

Figure 4.4: Impact parameters at the target plane of the third pion against three pion effective mass.

pion's crossing points and the V^0's crossing points are calculated. Figure 4.6 shows the effective three pion mass against the minimum crossing distance. The cut to remove the background was placed at 20 cm. The final cut for a candidate to be used as a kaon for analysis purposes was that the candidate mass should lie within 50 MeV of the accepted mass of the charged kaon [29] *i.e.* $444 < M_{3\pi} < 544$ MeV

4.3 Summary of cuts used to identify charged kaon decays

1. Each decay track has at least four space points,
2. each decay track passes through at least the first four MWPCs,
3. one track satisfies the hodoscope condition mentioned in the previous chapter,
4. $M_{\pi\pi} < 420$ MeV,
5. $|\alpha_{V^0}| < 0.45$,

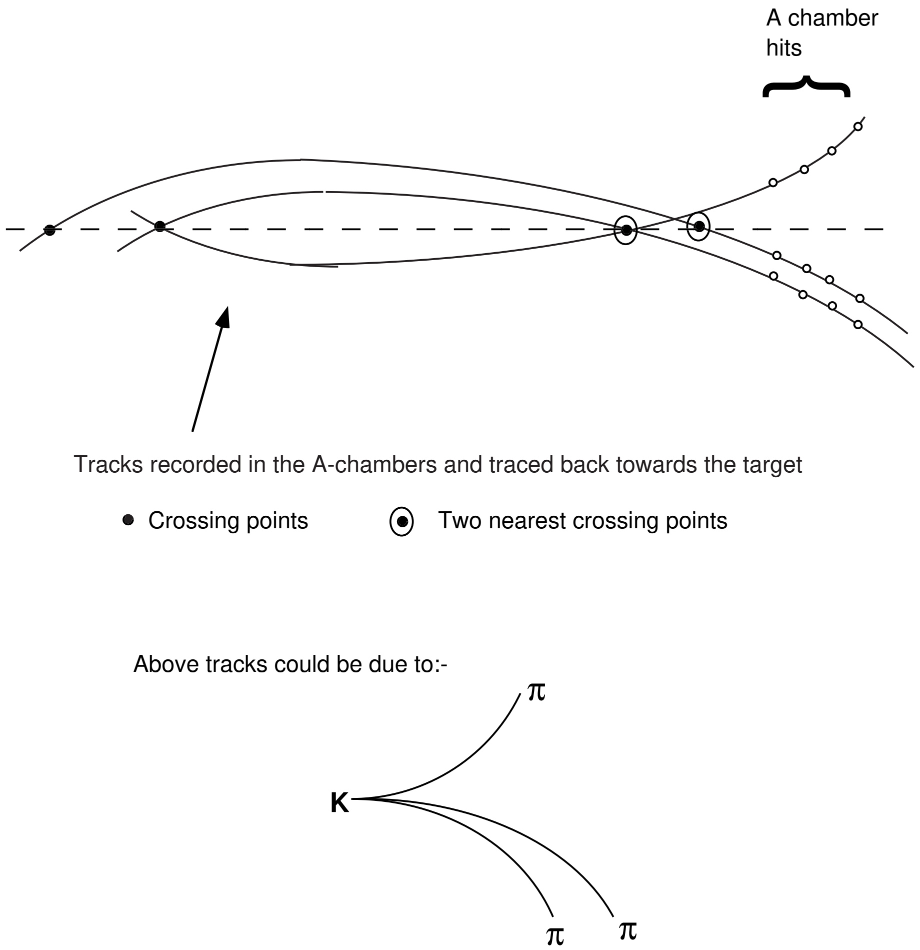

Figure 4.5: Schematic diagram of a kaon decay.

6. the decay vertex of the kaon lies in the range $-55 < x_\Omega < 71$ cm,
7. the impact parameters in the $y-$ and $z-$ directions at the target plane is less than 2.0 cm,
8. the decays tracks all have impact parameters in the $y-$direction of greater than 5.0 cm in the target plane,
9. the minimum distance between the crossing points of the V^0 line–of–flight and the third decay track is less than 20 cm and

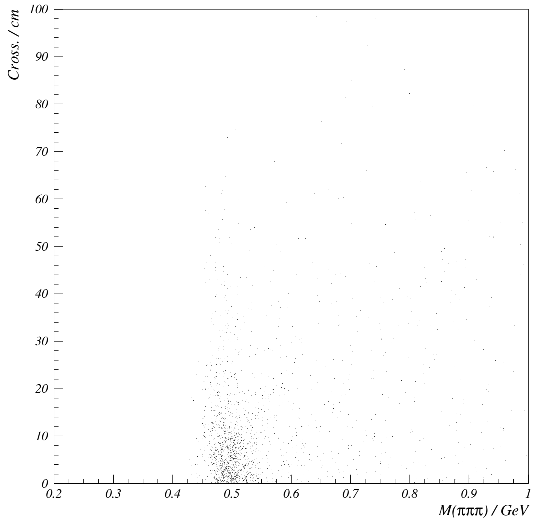

Figure 4.6: Minimum crossing distance against three pion effective mass.

10. the effective mass of the three pion system lies in the range $444 < M_{3\pi} < 544$ MeV

Figures 4.7a), b), c) and d) show the effective mass distributions after the first six, seven, eight and nine cuts respectively. Figures 4.8a) and b) show the effective mass distributions for K^+ and K^- respectively before the final mass cut has been applied. Upon application of this mass cut, there are 745 K^+ s and 354 K^- s (table 4.1), giving an uncorrected $\frac{K^+}{K^-}$ of 2.10 ± 0.63. The next chapter discusses the acceptance and reconstruction efficiency corrections needed to compare yields of different particle species.

4.4 Negative particle reconstruction

In order to measure the absolute enhancements of strange particles when going from the proton–sulphur collisions to sulphur–sulphur collisions, it is necessary to measure the yield of negative particles from both sets of data. For this purpose, data was taken at the level one stage of the trigger because these events are suitably unbaised towards

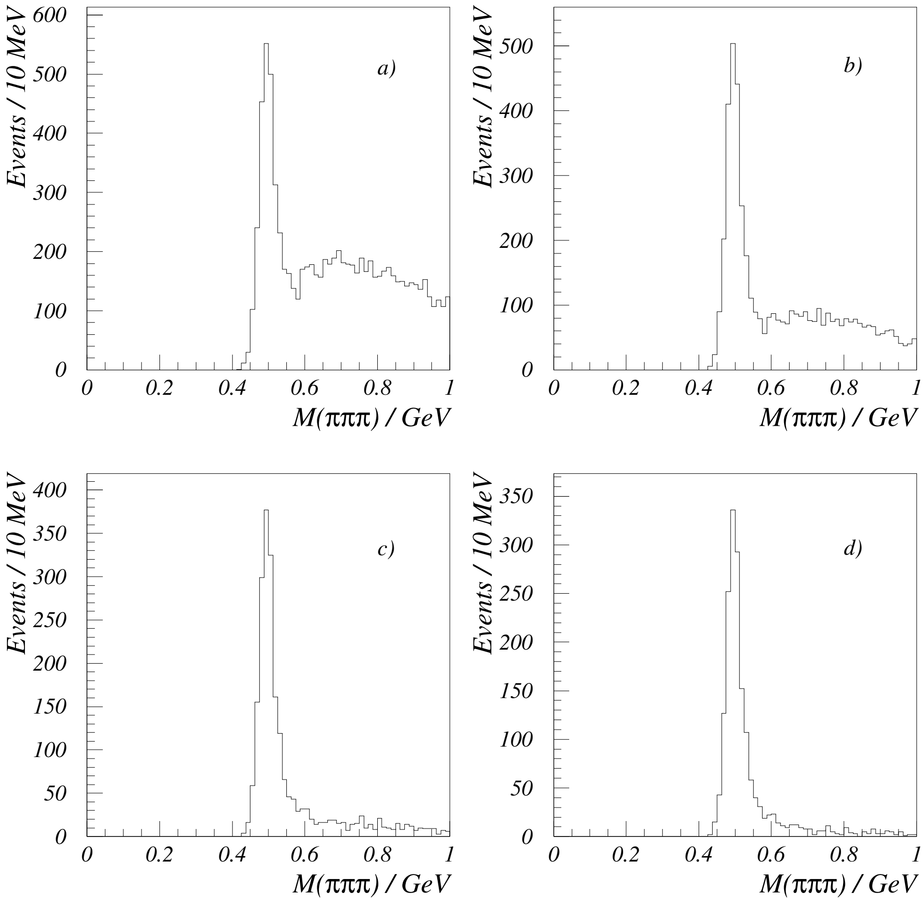

Figure 4.7: Three pion invariant mass after first a) six, b) seven, c) eight and d) nine cuts.

both strange and negative particles. Level two data is biased because of the condition that requires a multiplicity of at least two in the MWPCs. As there is no direct particle identification in the WA94 experiment, all negative particles are assumed to be pions. Positive pions prove to be more difficult to measure due to the large number of protons remaining from the target and projectile nuclei. The negative particle analysis was based on approximately 10 million triggers distributed evenly throughout the run.

Each track under consideration was required to trace through all seven MWPCs, including the 1 cm edge cut (described in the previous chapter), which removes the inefficient area of the detectors. Just like in the hyperon and charged kaon reconstruction, each track needed four space points to be considered further. The track must also pass

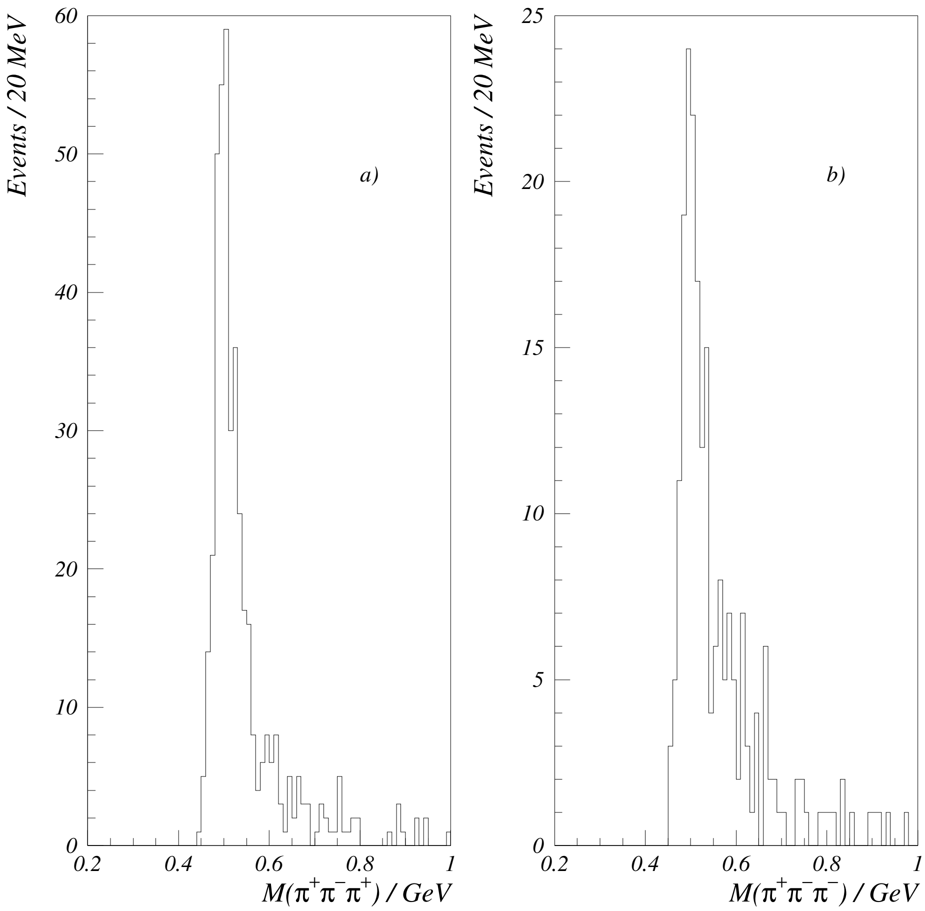

Figure 4.8: Three pion invariant mass for a)$K^+$and b)K^-candidates.

the RIGHT–RIGHT or LEFT–LEFT correlation condition that has been mentioned in previous sections.

Negative particles are traced back to the target plane and the impact parameters in both the $y-$ and $z-$direction are measured. Figure 4.9 shows the $y-$ and $z-$ impact parameters in the target plane plotted against each other and individually. The centre of the distribution corresponds well to the nominal target position. Particles that lie within 2.0 cm of the target position are considered for futher analysis. The total yields of both $K^{\pm}$ and negative particles are shown in table 4.1

Figure 4.10 shows the uncorrected $p_{\rm T}$ distribution and figure 4.11 the uncorrected rapidity distribution of the negative particles that pass all the selection criteria. The

Table 4.1: Level one negative particle and level two $K^{\pm}$ yields.

Particle Species	Field		Total
	Up	Down	
h^-	35297	13479	48776
K^+	529	216	745
K^-	251	103	354

cut off in the transverse momentum distribution drops off at 600 MeV/c. This effect is a result of the 'butterfly' design of the MWPCs. The rapidity distribution is strongly peaked in the forward region, because of the imposition of the hodoscope criterion. The corrected transverse momentum distribution is shown in chapter seven.

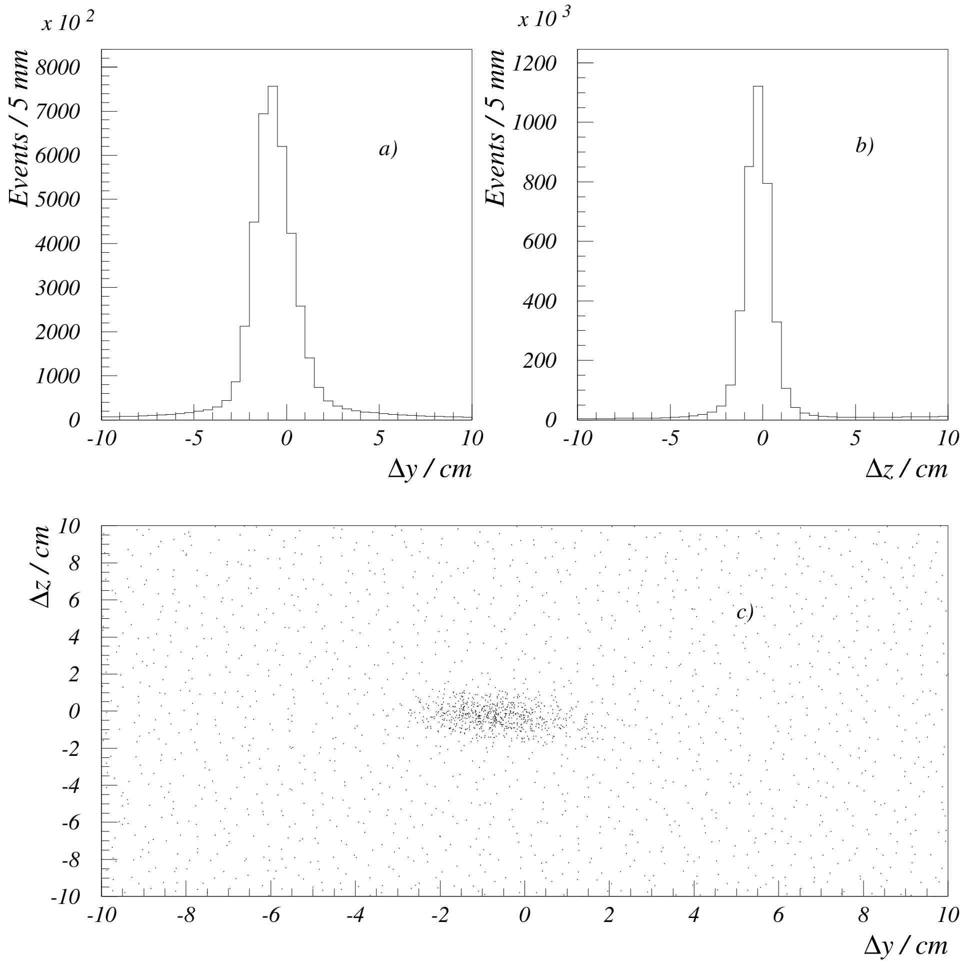

Figure 4.9: a)$y-$ and b) $z-$direction impact parameters for negative particles. c) shows the correlation of the two.

4.5 Summary

Selection criteria have been discussed for both charged kaons and negative pions. The statistics enable good comparisons with published results from other experiments and the WA94 sulphur–sulphur data for both species. The corrections for the distributions and yields will be discussed in later chapters, along with corrected particle ratios, transverse mass distributions and absolute enhancements of strange particles.

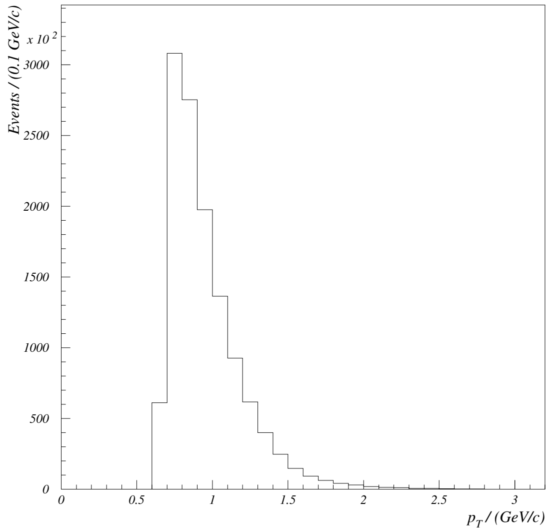

Figure 4.10: Negative particle transverse momentum distribution.

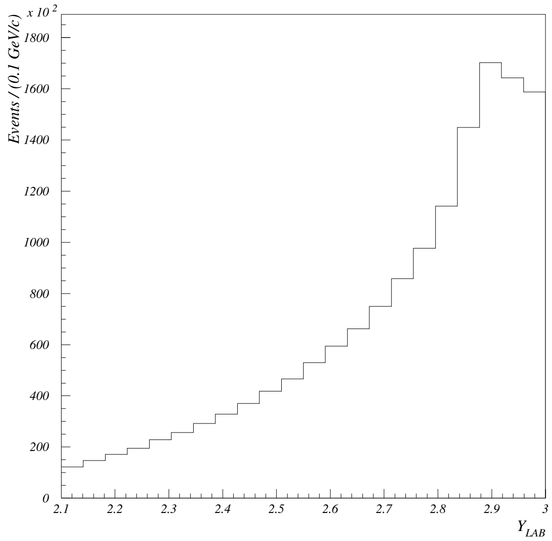

Figure 4.11: Negative particle rapidity distribution.

Chapter 5

Acceptance

As the detectors of WA94 do not cover the entire 4π solid angle and are several mean decay distances from the target, it is necessary to correct the data for acceptance in order to calculate particle yields in proton–sulphur and sulphur–sulphur collisions. This chapter briefly describes what acceptance is and then goes on to tackle the exact acceptance conditions for all the species of particle that have been studied.

Acceptance is a statistical measure of that fraction of all of a certain species of particle produced at the interaction point that would be recorded by the detectors if they were 100% efficient. The A–chambers were designed to be insensitive to particles which have transverse momentum less than 0.6 GeV/c. This is an example of a geometrical constraint on the kinematic region of decays that the detectors can observe.

A second type of constraint on acceptance is a physical, analysis-based constraint, such as requiring the decay vertex to lie in a fiducial region. The final type of restriction on the acceptance is related to the trigger. The most obvious example of this is the hodoscope condition; at least one of the tracks must pass through both of either the right hand or the left hand quadrants of both of the hodoscopes. This was performed early in the trigger to reduce the number of empty events written to tape. All of these types of conditions have to be considered, because they were all used in either the data-taking procedure or in the final analysis to select strange particle decays. One needs to take care to ensure that the cuts in the program which calculated acceptances and in the final analysis programs are precisely the same. This chapter shall describe the conditions used in order to calculate the acceptances starting with the Λ and $\overline{\Lambda}$ acceptances and then going on to the acceptances for Ξ^-, $\overline{\Xi}^+$, K^+, K^- and π^-, concluding with a description of the hodoscope efficiency calculation.

5.1 Λ and $\overline{\Lambda}$ Acceptances

The acceptance program generates one million Monte Carlo Λ decays at the centre of each bin in the kinematic region

$$2.5 < Y_{LAB} < 3.0$$

$$0.8 < p_T < 3.0 \text{ GeV}/c.$$

Each Y_{LAB} bin is 0.05 units wide and each p_T bin is 0.1 GeV/c wide. From the Y_{LAB} and the p_T value, the longitudinal momentum p_L is defined as

$$p_L = m_T \sinh(Y_{LAB})$$

where

$$m_T = \sqrt{M_\Lambda^2 + p_T^2}.$$

Given the p_T value for any Λ, one must also work out the components of the momentum in both the $y-$ and $z-$directions of the OMEGA co-ordinate system. To do this, the angle of the momentum vector in the $y_\Omega - z_\Omega$ plane was assigned a random value which was generated uniformly between 0 and π, *i.e.* in the upper hemisphere.

The next step is to make the Λ travel in this direction for a random decay length. This length is determined by the probability distribution $P(d)$ below.

$$P(d) = e^{-M_\Lambda d/|p|c\tau}$$

where $|p|$ and τ are the magnitude of the momentum and the mean lifetime of the Λ respectively. A random number with a uniform distribution between 0 and 1 is generated and substituted for $P(d)$. The $c\tau$ of the Λ is 7.89 cm. The program can then calculate the decay distance from the target and hence, using the momentum vector of the particle under consideration, calculate the position of the decay vertex in three-dimensional space. At this point one implements the vertex cut, *i.e.* that the vertex must be in the fiducial region $-80 < x_\Omega < 71$ cm.

The Monte Carlo Λ is forced to decay into a p and a π^- with equal but opposite momenta in the centre-of-mass frame; the magnitude of the momentum for each decay product in the centre of mass frame is $p^* \simeq 0.101$ GeV/c and the direction of the proton is determined using a three-dimensional random number generator flat in the cosine of the centre of mass decay angle mentioned in chapter three. Then the momentum vectors are transformed from the CM frame to the LAB frame using a CERN library routine.

The transformed momenta, the charge of the decay particles and the x-position of the final position are the inputs for a tracing algorithm that employs a map of the magnetic field in the OMEGA spectrometer. The output of the routine are the position and momentum vectors of the particle at the desired x-position. This is used to trace the decay particles to the positions of the A1 and A7 chambers. If the y_Ω and z_Ω co-ordinates fall within the sensitive areas of the two chambers the event is kept.

The tracks are then traced to the two hodoscope planes. Only one of the tracks has to pass through both planes, but this track must pass through either the right hand quadrants of both planes or the left hand quandrants of both planes. This is called a correlation of hits. If one of the tracks satisfies this correlation and a random number between zero and one is less than the hodoscope slab efficiency (as discussed in section 5.4) the event is kept.

The final cut on the Monte Carlo Λs is the ambiguity cut. The decay under consideration must have Armenteros α in the range $0.45 < \alpha < 0.6$. If the decay satisfies all of the criteria outlined above, then the decay is accepted.

To gain adequate statistics, the program generates one million events per $Y_{LAB} - p_T$ bin. The total acceptance is then given by

$$\text{Acceptance} = \frac{\text{Number accepted}}{\text{Number generated}} \times \frac{1}{2} \times 0.641$$

where the factor of $\frac{1}{2}$ takes into account that the Λs were only generated in the upper hemisphere. The factor of 0.641 is the branching ratio of the decay $\Lambda \rightarrow \mathrm{p} + \pi^-$ and it allows for the unseen decays of the Λ. The acceptance of Λs over the $Y_{LAB} - p_T$ is shown in figure 5.1.

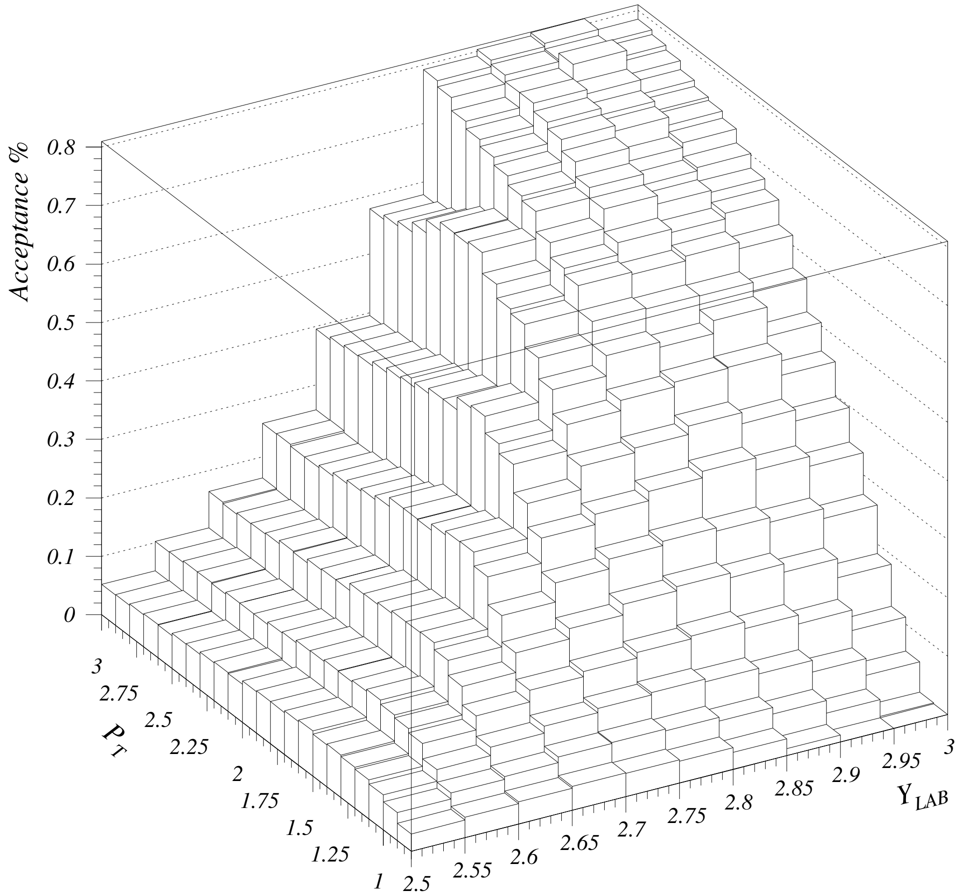

Figure 5.1: Λ acceptances.

5.2 Ξ^- and $\overline{\Xi}^+$ acceptances.

To calculate the acceptances of Ξ^- decays is a slightly more involved task. There are two decays instead of one for each event, and the Λ from the Ξ^- decay must fulfil some of the cuts above. The Monte Carlo Ξ^-s are generated in the kinematic window

$$2.5 < Y_{LAB} < 3.0$$

$$1.2 < p_T < 3.0 \text{ GeV}/c$$

and the transverse mass and momentum are constructed in an analogous way, using M_{Ξ^-} instead of M_Λ.

It must be remembered that the Ξ^- is charged, unlike the Λ. Instead of merely extrapolating from one point to the next linearly, the track of the Ξ^- must be calculated using the same tracing algorithm that was described earlier in this chapter. The decay distance is formulated in the same way, but with $c\tau = 4.91$ cm. The fiducial region for the Ξ^- vertex is slightly larger, $-125 < x_\Omega < 71$ cm. The Ξ^- must then decay via

$$\Xi^- \to \Lambda + \pi^-$$

again using the same technique as above, but with a different p^*. In this case, $p^* = 0.139$ GeV/c.

The π must trace through the first four A-chambers and also hit the target plane (when traced backwards) at a distance in the bend direction (the $y_\Omega-$direction) greater than 6 cm from the target itself. This is a cut applied to the real Ξ candidates and hence should be applied here. Failure to do so would result in a biased p_T spectrum. The Λ from the Ξ decay is then decayed in exactly the same way as it is in the Λ acceptance program, except that the tracks need only trace through the first four A-chambers instead of all seven. Again, at least one of the tracks must satisfy the hodoscope condition (including the efficiency of each slab in the same way as in the case of the Λ acceptance program) for an event to be accepted. The acceptance is then calculated using the same formula as for the Λs. Figure 5.2 shows the acceptances of Ξs as a function of Y_{LAB} and p_T.

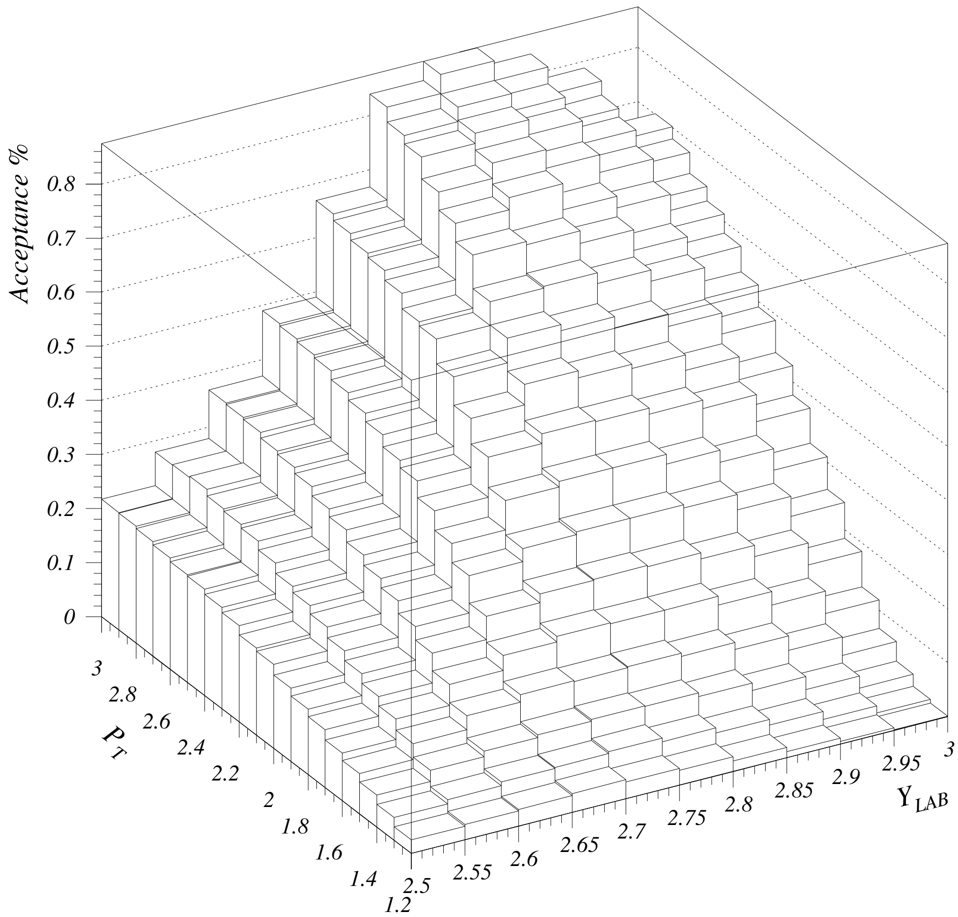

Figure 5.2: Ξ^- acceptances.

5.3 Charged kaon and negative particle acceptances

The calculation of the charged kaon acceptances is slightly different to those for the Λ and Ξ particles because the kaon decays into three particles *via* the 'tau' decay $K^\pm \to \pi^+\pi^-\pi^\pm$. One million kaons per $Y - p_T$ bin are generated by a CERN three–body decay subroutine GENBOD [57] and made to decay with a decay length given by

$$d = -\frac{c\tau|p|}{M_K}\ln(R),$$

where $c\tau$ of the kaon is 370.9 cm and R is a random number with a flat distribution between 0 and 1. If the kaon vertex lies in the same region as defined in chapter four, *i.e.* $-55 < x_\Omega < 71$ cm, the kaon is decayed into three charged pions. The energy and momentum of the decay is randomly distributed between the three pions, such that the total centre of mass energy is equal to the mass of a charged kaon and momentum is conserved. The momentum four–vectors then undergo a Lorentz transformation to the laboratory frame.

Just as in the acceptance calculations for the Λ and Ξ particles, the Monte Carlo charged kaons must satisfy the analysis cuts and trigger conditions as set out in chapter four. The decay particles are required to trace through the sensitive regions of the first four MWPCs and must miss the target by at least 5 cm when traced back to the target plane. Furthermore, at least one of the tracks has to satisfy the hodoscope condition.

The acceptances of the kaons are then given by

$$\mathrm{A}cceptance = \frac{\text{no.accepted}}{\text{no.generated}} \times \frac{1}{2} \times 0.0559,$$

where the factor $\frac{1}{2}$ is present due to generation only taking place in the upper hemisphere, and the factor 0.0559 is the branching ratio of a charged kaon into three charged pions. The acceptances of the Ks are shown in figure 5.3.

In the negative particle case, the particles were generated as pions. The pions are generated at the target and are required to pass through all seven MWPCs. The track must also satisfy the hodoscope condition as mentioned previously. The acceptances of the pions are shown in figure 5.4. The acceptance tables of all the particles mentioned in the chapter are shown in appendix B. It will be noted that the pion acceptance plot shows a distinct dip at about $p_{\mathrm{T}} = 1.6$ GeV/c. This is due to the hodoscope condition. The tracks in this kinematic region sweep from positive to negative y_{Ω} when going from HZ0 to HZ1, thus failing the hodoscope trigger condition.

The acceptance tables for the Ks and πs are presented here and also in tabular form in appendix B. The events used in the finally corrected analysis are those which lie in the region of good acceptance, which is defined as those bins which have acceptance greater than 10% of the maximum acceptance for any particle under consideration.

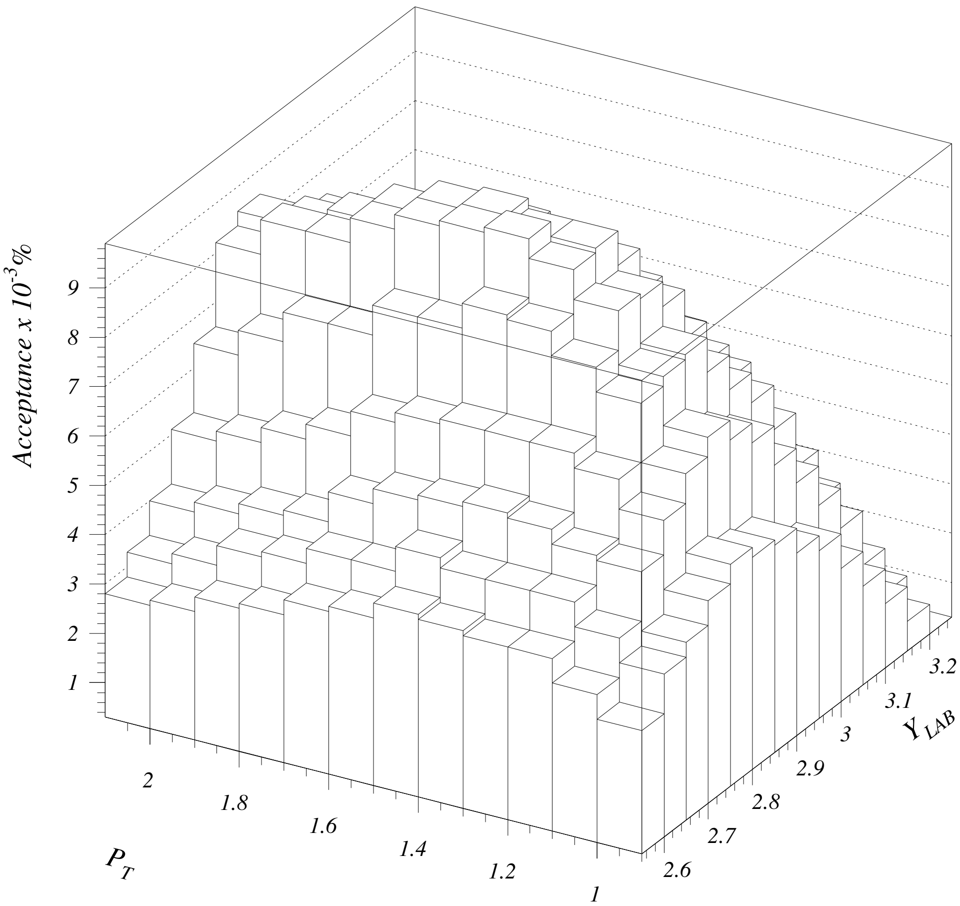

Figure 5.3: K^+ acceptances.

5.4 Hodoscope Efficiencies

The hodoscope efficiencies have been determined using about 350,000 special events, in which the hodoscopes were not used in the trigger. These events, taken from seven runs, were distributed throughout the data–taking. To calculate the efficiencies slab by slab, the requirements for 'good' tracks were that they should have seven space points - so that the momentum of each track is well defined - and that the track traced to the slab under consideration. The slab that the track traced to is recorded and the hit pattern in the hodoscope is consulted to see whether the slab fired. If this is the case then the traced track is deemed to have fired the slab. The efficiency is defined as the fraction of 'good' tracks that fired the slab divided by the total number of 'good' tracks tracing through a slab.

To account for track smearing by the reconstruction programs, the tracks used in

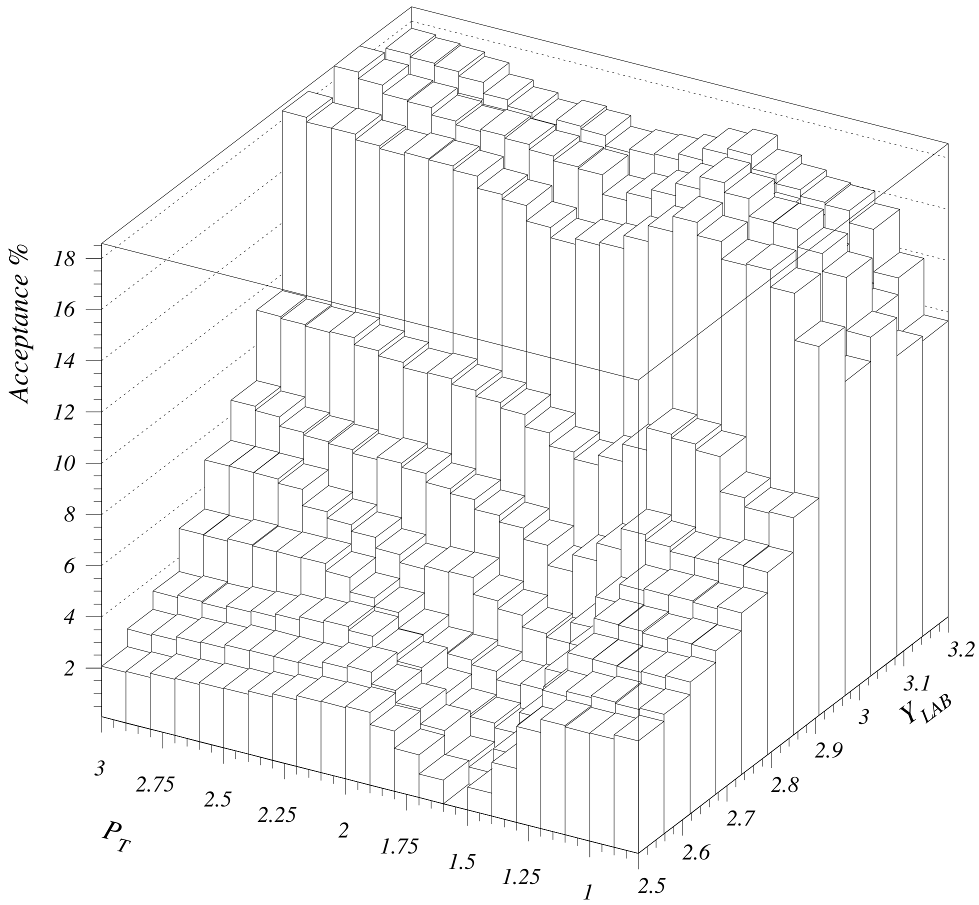

Figure 5.4: π^- acceptances.

the efficiency calculation were required to pass through the slab at least one centimetre from the edge. If a track that in reality misses a slab but is smeared by the reconstruction programs such that it appears to pass through the slab, the efficiency would be effectively reduced. The slab efficiencies for both halves of the hodoscopes HZ0 and HZ1 are presented in graphical form in figure 5.5.

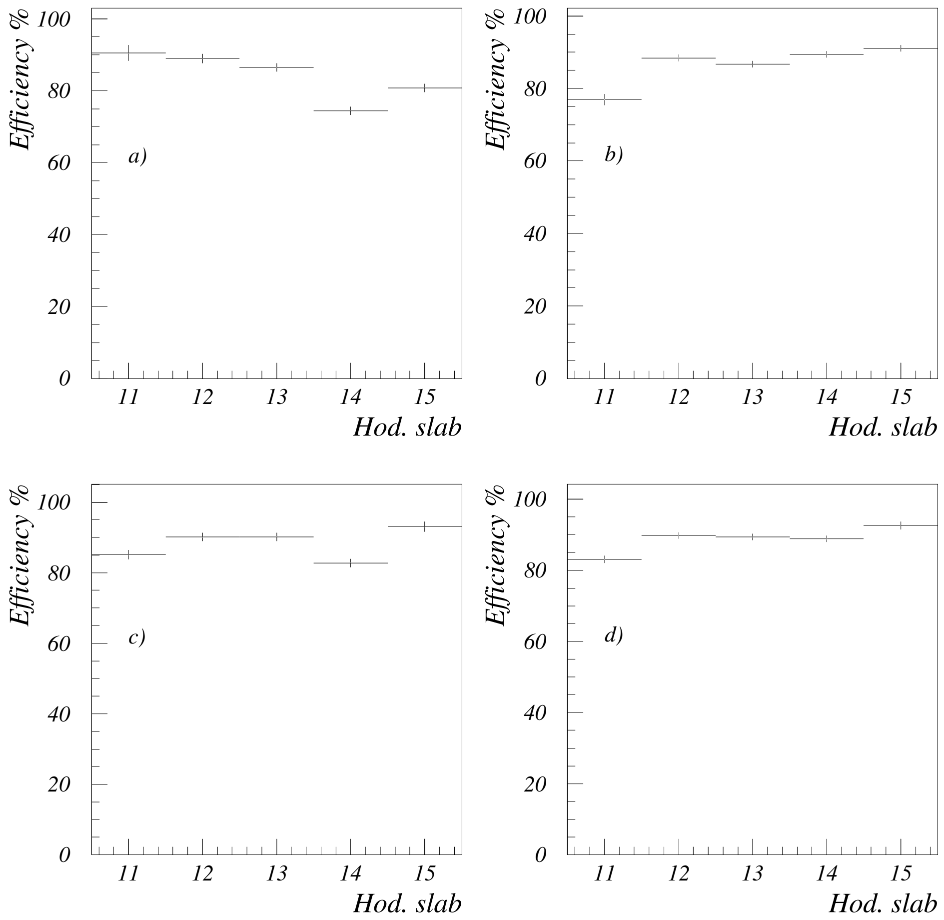

Figure 5.5: Hodoscope efficiencies for quadrants a) HZ0 right, b) HZ0 left, c) HZ1 right and d) HZ1 left.

Chapter 6

Reconstruction Efficiencies

Given that an algorithm is used to reconstruct strange and multi–strange particle decays, it is important to ascertain how well the software does its job, especially when comparing two different species of particle, whose efficiencies are different. The way to test this is to implement another Monte Carlo simulation, using the chamber efficiencies calculated in section 6.4. The method, in short, is to find the percentage of Monte Carlo events that survive being passed through the reconstruction chain. This chapter will explain, in detail, how this is done.

6.1 Λ and $\overline{\Lambda}$ Reconstruction Efficiencies

The first program in the chain, as shown in figure 6.1, generates Monte Carlo Λs in much the same way as the acceptance program did. The particles are generated over a $Y_{\mathrm{L}AB}$ and p_{T} distribution as opposed to a given $Y_{LAB} - p_T$ point. In addition, one must realise that the reconstructed tracks are imperfectly reconstructed (due to the finite resolution of the detectors), such that hyperons can 'smear' either into or out of the desired $Y_{LAB} - p_T$ window. To take this into account, the particles are generated over a larger window than is accepted by the final analysis program, so that particles are allowed to smear into the accepted region as well as out.

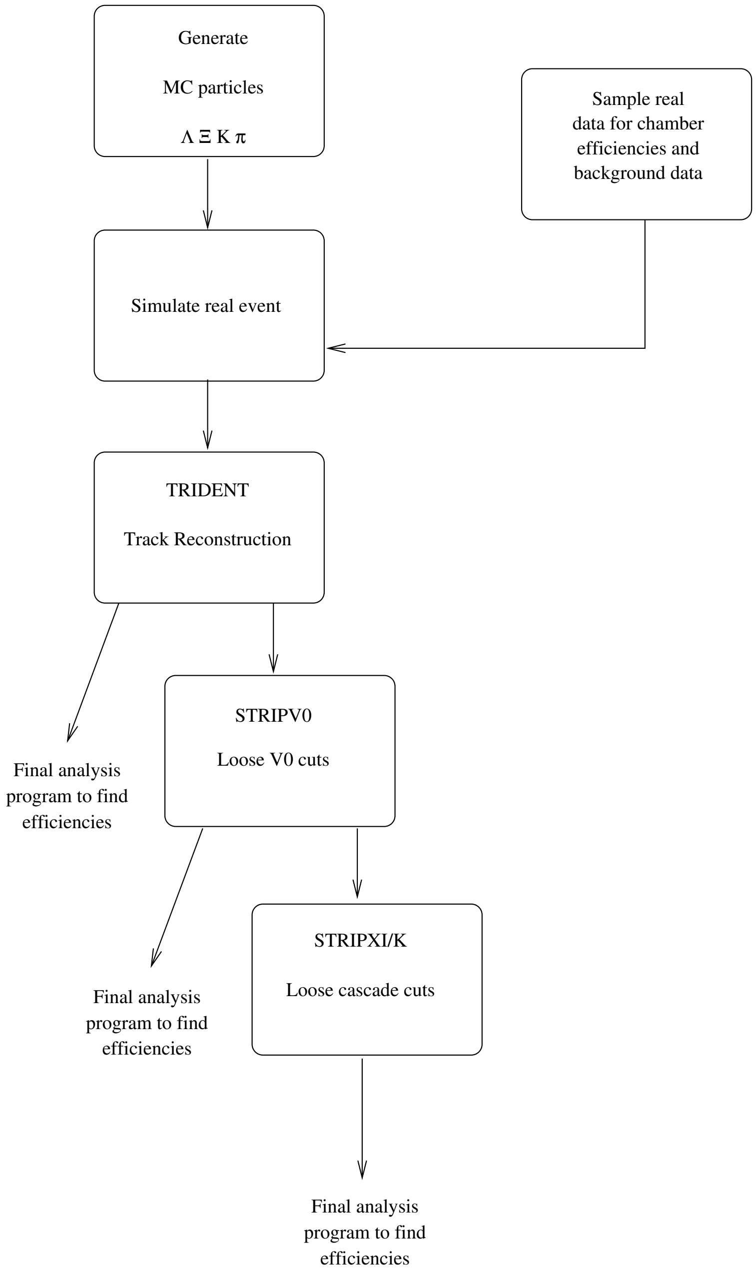

Figure 6.1: Diagram showing the reconstruction efficiency chain of programs.

A Monte Carlo event is built up in two stages. Stage one is where the Λ is generated according to the kinematic distributions which is done in the first program in the chain.

The window is slightly larger than the 'proper' window for smearing reasons. The Λ particles are generated with a transverse mass m_{T} distribution

$$\frac{dN}{dm_T} \propto m_{\mathrm{T}}^{\frac{3}{2}} e^{-m_{\mathrm{T}}\beta}$$

where $m_{\mathrm{T}} = \sqrt{p_{\mathrm{T}}^2 + M^2}$ and M is the mass of the particle. The limits on m_{T} are $1.37 < m_{\mathrm{T}} < 3.48$ GeV, which correspond to limits in p_{T} of $0.8 < p_{\mathrm{T}} < 3.3$ GeV/c. β is determined from the real data when they are corrected for acceptance only. To be passed on to the second program in the chain, the Λ has to have $0.9 < p_T < 3.1$ GeV/c. The rapidity distribution of the Λs is generated flat in the region $2.2 < Y_{LAB} < 3.3$ and the vertex is generated between the values $x_\Omega = -135$ cm and $x_\Omega = 71$ cm; vertex smearing increases with distance of the decay from the A-chambers.

Both of the tracks from the decay particles must pass through all seven A-chambers, but those events that have both tracks passing the 1cm edge cut are flagged. A further condition is that one of the decay tracks from a Λ must pass through both hodoscope planes, but need not satisfy the correlation condition nor the 1cm edge cut. The Armenteros-Podolanski variable α is calculated for each event and those events whose α falls in the range $0.4 < \alpha < 0.70$ are also kept to allow for smearing in α.

The conditions outlined in the previous paragraphs place relatively loose criteria on the Λs that are passed to the background mixing program. The output from the generating program consists of the $y - z$ co-ordinates of the hits of each track in each plane in each of the seven chambers and also a logical flag. This flag is set to 'true' if the event satisfies the exact acceptance conditions mentioned in chapter five and 'false' if not.

As a self-consistency check, the program weights each Λ that has a 'true' flag with the appropriate acceptance weighting. In this way, it is possible to check the inverse slope of the m_T distribution and also to check the overall normalisation in the window under consideration as a function of Y_{LAB} and p_T. To do this adequately requires high statistics (*i.e.* at least 100,000 events).

The second stage of the complete Monte Carlo generation is mixing in the A-chamber hits from the Λ decay tracks into real background data to make sure that the final event looks more like a real event. It is important to do this because reconstruction efficiencies are a function of the average number of clusters per plane (hereafter known as the planar cluster multiplicity). For example if a level two Λ is generated and level two background data is added to it, then the average planar cluster multiplicity will be higher than that for the real data. This means that level one background data are used.

The program then works out the quadrant of each plane through which each decay track will pass. The effect of the detector efficiency is taken into account by seeing whether a random number between zero and one is greater or less than the given chamber efficiency the program decides whether the track produces a real hit or not. If the random number is above the given chamber efficiency for that plane, then there is deemed to be no real hit in the chamber. The method for calculating chamber efficiencies is described in section 6.4

The distance between the wires inside the chambers is 2 mm, so to simulate a cluster of wire hits around any track intercept, if the track passes greater than $\frac{1}{3}$ of the wire pitch from the nearest wire, then both wires either side of the track fire. If not, then only the nearest wire fires. The wire hits from real events are unpacked from the ROMULUS block structure and added to the wire hits from the Monte Carlo Λs. The complete events are then re-packed into the ROMULUS block structure and written out in the EPIO data format that the track identification program TRIDENT expects.

The events are then passed through TRIDENT, STRIPV0 and a final analysis program that is exactly the same as that used for real data apart from the subroutine that reads in the data. All of the cuts are as they are for the real data. At this final stage there are two important histograms. The reconstructed m_T distribution is used to see how far away the inverse slope has moved from the input value at the top of the chain. The planar cluster multiplicity histograms before TRIDENT for those flagged 'true' and at the end of the chain are used to find the reconstruction efficiency as a function of planar cluster multiplicity. For each bin, the reconstruction efficiency is given by

$$\text{Efficiency} = \frac{N_{rec}}{N_{gen}}$$

where N_{gen} is the number of events that have satisfied all of the final cuts before TRIDENT and N_{rec} is the number of reconstructed events that have survived the same cuts. The Λ and $\overline{\Lambda}$ reconstruction efficiencies for both field polarities are shown as a function of average planar cluster multiplicity in figure 6.2.

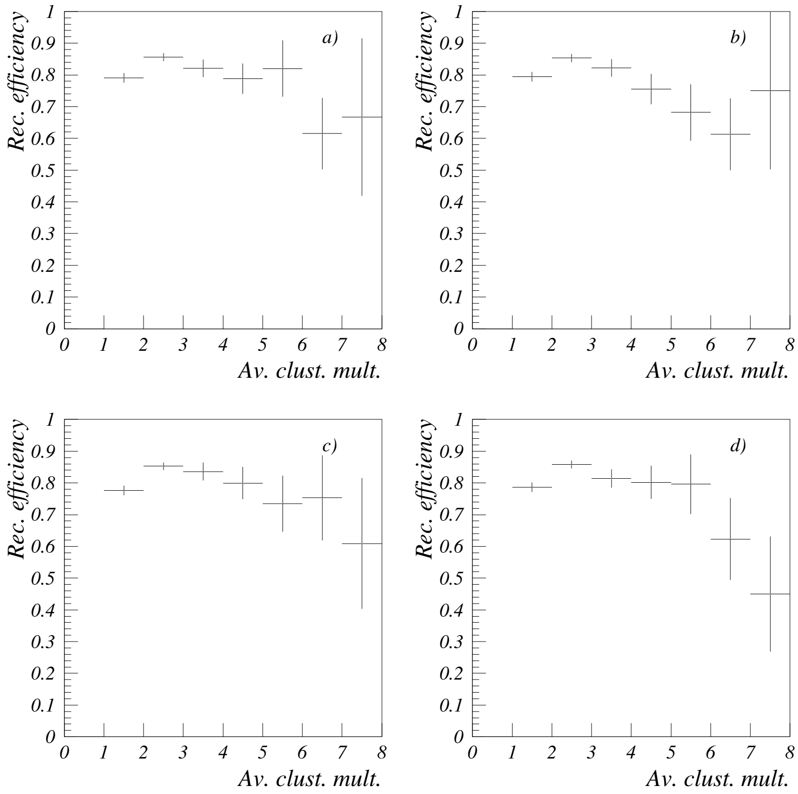

Figure 6.2: Reconstruction efficiencies for a) Λ H$\Uparrow$, b)$\overline{\Lambda}$ H$\Uparrow$ c)Λ H$\Downarrow$ d) $\overline{\Lambda}$ H$\Downarrow$. 100% = 1.

6.2 Ξ^- Reconstruction Efficiencies

As for the case of the Λs, the Ξ^- reconstruction efficiencies are determined by using Monte Carlo events. The decays are generated in a similar manner to that employed by the program that calculates acceptances. An almost identical program to that used for the Λs mixes the tracks of the decay particles in with background data. The complete Monte Carlo events are passed through TRIDENT, STRIPV0 and STRIPXI and then onto a final analysis program that is identical to that used to analyse the real data, again apart from the way that the events are read in. The efficiencies are determined in precisely the same manner as for the Λs, *i.e.* by dividing the number of reconstructed Ξ^-s by the number of Ξ^-s with a 'true' flag attached to them.

In order to be passed onto the background mixing program, the event must satisfy the following requirements:

The Ξ^-s are generated over the p_T domain $1.1 < p_T < 3.3$ GeV/c with the m_T distribution given by

$$\frac{dN}{dm_T} \propto m_T^{\frac{3}{2}} e^{-m_T \beta}$$

where β is again determined by the acceptance corrected data. Once more, the particles have a flat rapidity distribution in the region $2.2 < Y_{LAB} < 3.3$.

The Ξ^- decay vertex must fall in the fiducial region $-200 < x_\Omega < 71$ cm and the Λ vertex must also fall into the fiducial region $-80 < x_\Omega < 71$ cm. Again this allows for smearing in the vertex position. Finally one of the tracks from the decay particles must satisfy the loose hodoscope condition described in the Λ reconstruction efficiency calculation. Those particles that satisfy the analogous conditions in the final analysis program are given the 'true' flag in the same way as in the Λ efficiency chain. The Ξ^- and $\overline{\Xi}^+$ reconstruction efficiencies for both field polarities are shown in figure 6.3

6.3 $\mathrm{K}^\pm$ and π Reconstruction Efficiencies

In a similar fashion to the Λ and Ξ^- reconstruction efficiencies, the reconstruction efficiencies for $\mathrm{K}^\pm$ and π are calculated using Monte Carlo techniques. The same mixing, track reconstruction and V^0 finding programs are used and in the case of the

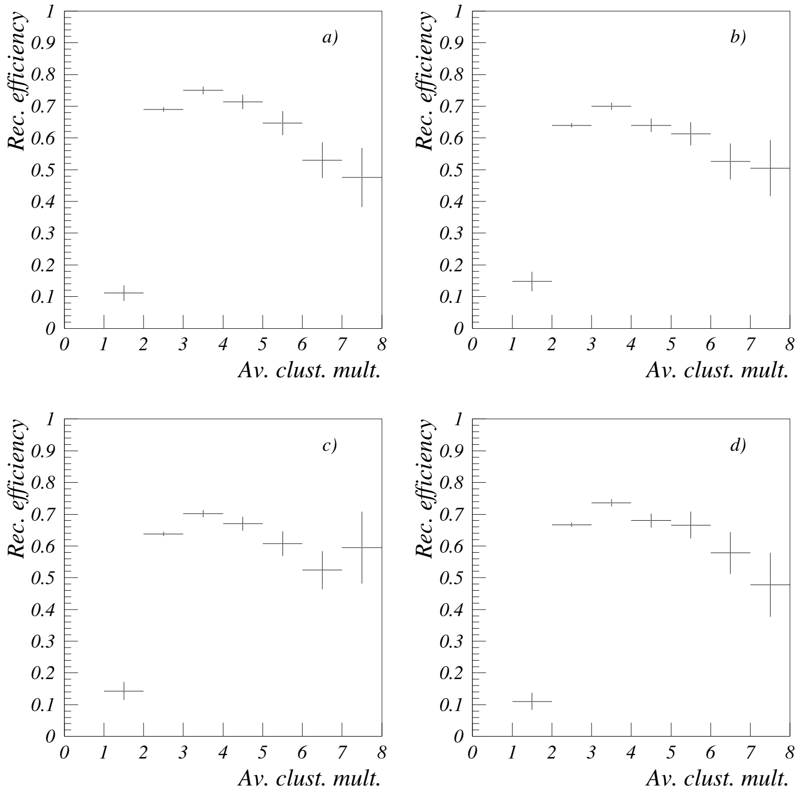

Figure 6.3: Reconstruction efficiencies for a)Ξ^- H$\Uparrow$, b)$\overline{\Xi}^+$ H$\Uparrow$ c)Ξ^- H$\Downarrow$ d)$\overline{\Xi}^+$ H$\Downarrow$. 100% = 1.

charged kaons, the same program that combines a third track with a V^0 is also used. The remainder of this section will outline the differences in the generation programs and the final analysis programs.

The K$^\pm$s are generated over the p_T domain $0.9 < p_T < 2.2$ GeV/c with the m_T distribution given by

$$\frac{dN}{dm_T} \propto m_T^{\frac{3}{2}} e^{-m_T \beta}$$

where β is again determined by the acceptance corrected data. Once more, the particles have a flat rapidity distribution in the region $2.2 < Y_{LAB} < 3.3$.

The particle was decayed into three pions using the same CERN routine employed by the acceptance program. The decay distance was assigned in the same way as before. If the decay occured in the region $-100 < x_\Omega < 71$ cm, then the decay was kept for further processing. This allows for vertex smearing. The decay tracks should pass through the first four A–chambers without the 1 cm edge cut and one track should pass through both of the hodoscopes. Those charged kaons that satisfy the analogous cuts from the final analysis program are flagged 'true' in just the same way as the Λ and the Ξ^- before. The calculation chain then proceeds as before, using the charged kaon analysis program as used in chapter 4. The K^+ and K^- reconstruction efficiencies are shown in figure 6.4.

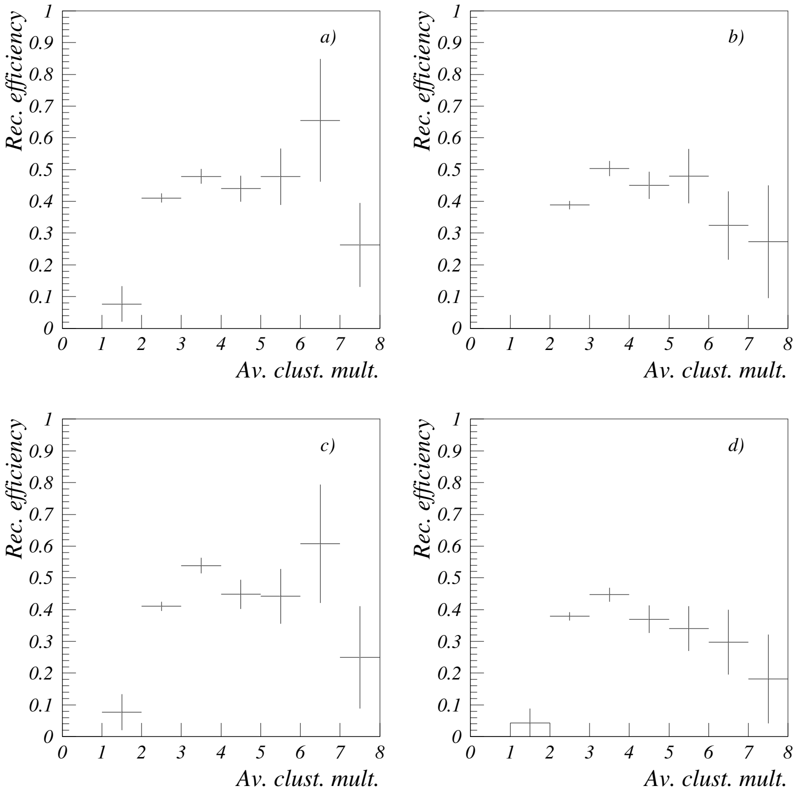

Figure 6.4: Reconstruction efficiencies for a)K^+ H$\Uparrow$, b)K^- H$\Uparrow$ c)K^+ H$\Downarrow$ d)K^- H$\Downarrow$. 100% = 1.

The pions were generated in the same way as in the acceptance program, but over the kinematic region similar to the Λs. Those generated pions that passed through all seven A–chambers and the two hodoscope planes were processed further. The points where the pion crossed the chambers was recorded and used to identify the generated pion in the final analysis program after background was added. Once more, those tracks satisfying the final analysis cuts were flagged and the data was passed through a mixing program, track reconstruction program and then a final analysis program. Care was taken to identify the correct track in the event. Those flagged tracks which passed the final cuts were used to calculate the final reconstruction efficiencies, which are shown, for both field polarities, in figure 6.5

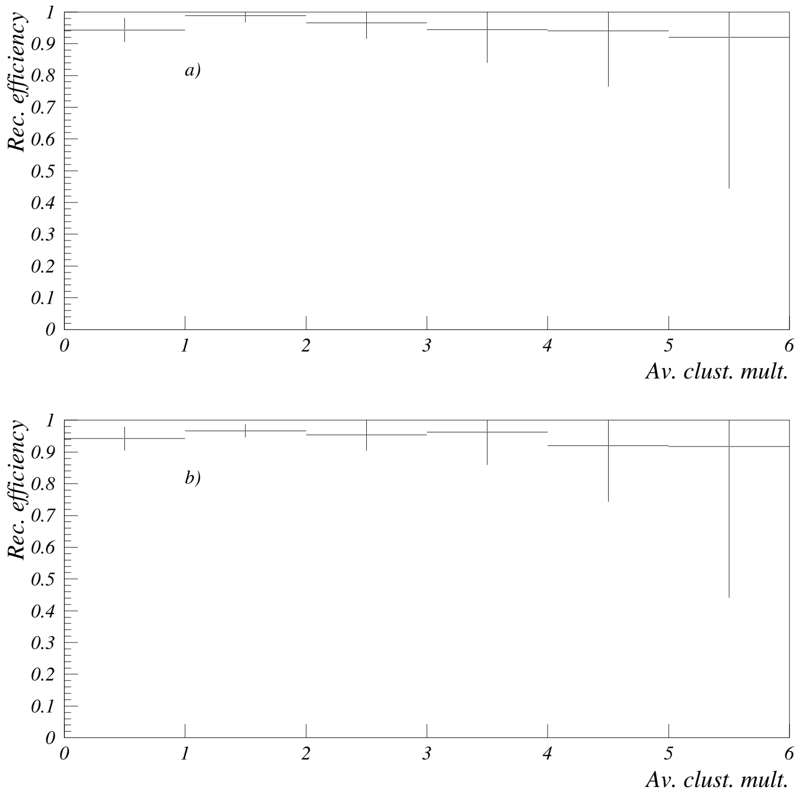

Figure 6.5: π^- reconstruction efficiencies for a) H$\Uparrow$ and b) H$\Downarrow$. 100% = 1.

6.4 Chamber Efficiencies

Chamber efficiencies have been calculated using over 400,000 level one events sampled throughout the entire proton-sulphur run. Level two data should not be used, because of the multiplicity condition from the first four A-chambers. These events are biased and so are not used.

6.4.1 Chamber Efficiency Calculation Method

The task here was to calculate the efficiency of each quadrant (as defined in figure 6.6) of each of the 21 wires planes in the A-chambers. The sample[1] of raw level one data was processed by TRIDENT once and then again by a special version of TRIDENT. This new version would have the chamber under consideration removed from the track fitting algorithm.

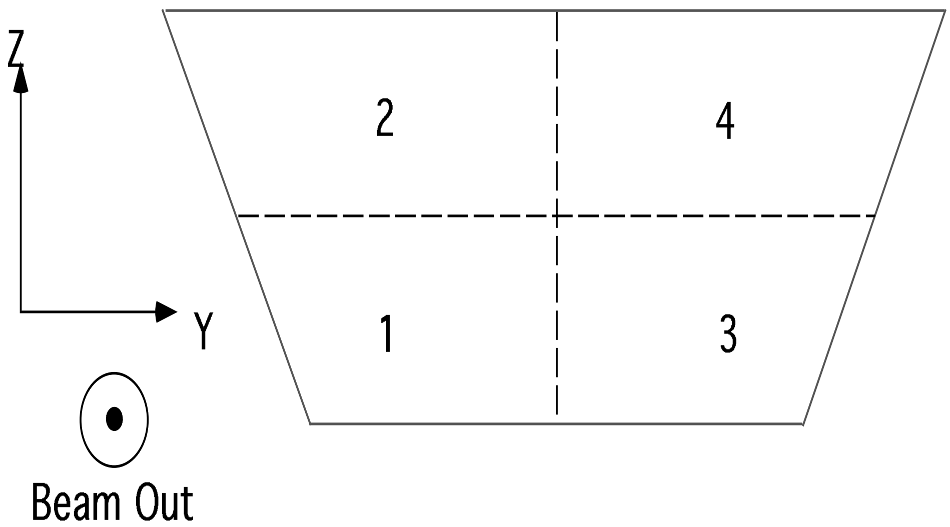

Figure 6.6: Schematic diagram showing a chamber divided into quadrants.

The output from this program was then passed to a further program which identified all tracks with six space points for each event. The program traced the track to the U, V and Y plane of the chamber under study and the recorded the point of intersection. The wire hit information in the event record is decoded and the program checks if the central wire of any cluster in the event is within two millimetres of the point of intersection in the plane of the track. If this is indeed the case, then the plane is said to have detected the track. The number of successfully detected tracks as a percentage of the total number of tracks is the chamber efficiency for any given quadrant.

[1] Every tenth event from each raw data cartridge was put in a file. Ten cartridges were produced covering the entire run.

Chamber Edge Effects

The A-chambers' 'butterfly' profile was described in chapter two. It was thought that removing graphite paint might well affect the efficiency of the planes near to the edges of the sensitive regions. A study showed that the efficiency did indeed drop off in the centimetre nearest to the edge of the sensitive region. For this reason, there is a cut of one centimetre around the inside of the edges to ensure that only the regions of uniform efficiency are used.

6.4.2 Chamber Efficiency Results

The total efficiency for each quadrant of each plane of each chamber has been calculated. These results are presented in graphical form in figure 6.7. The efficiency is fairly uniform. This has been noticed in earlier runs using these chambers.

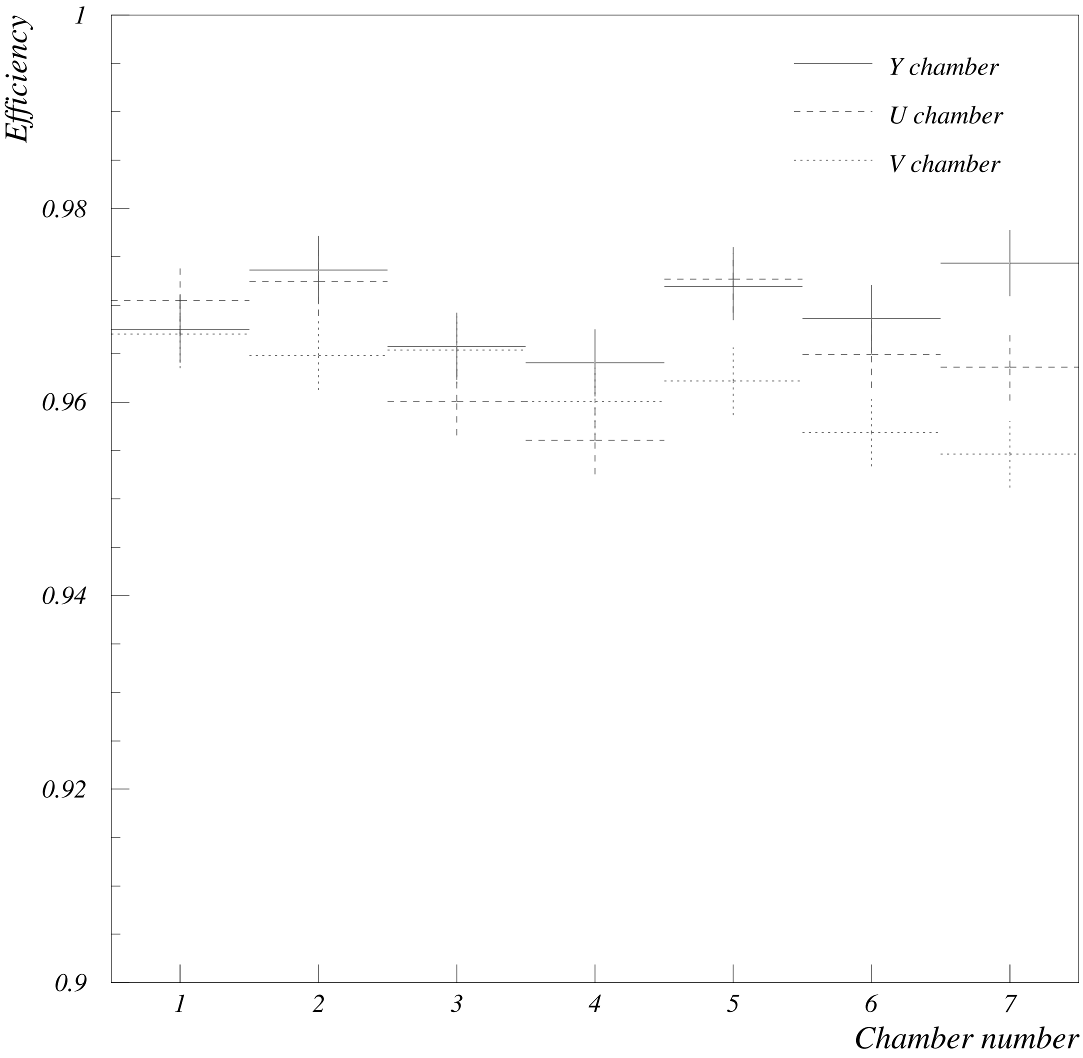

Figure 6.7: Efficiencies for chambers A1–A7. 1.0 = 100%.

6.5 Summary

Reconstruction efficiencies are important when it comes to comparing two different species of particle. Using the procedures that were outlined in this chapter, the reconstruction efficiencies for Λs, Ξ^-s, $K^\pm$ and πs have been calculated implementing the chamber efficiencies that were calculated *via* the procedure in section 6.4, thus reflecting the efficiencies of the detectors. The overall reconstruction efficiencies are shown in table 6.1

Table 6.1: Overall reconstruction efficiencies in %.

Particle Species	Field	
	Up	Down
h^-	95 $\pm$ 2	93 $\pm$ 2
K^+	44 $\pm$ 2	40 $\pm$ 2
K^-	40 $\pm$ 2	42 $\pm$ 2
Λ	83 $\pm$ 1	82 $\pm$ 1
$\overline{\Lambda}$	82 $\pm$ 1	83 $\pm$ 1
Ξ^-	70 $\pm$ 2	65 $\pm$ 2
$\overline{\Xi}^+$	65 $\pm$ 2	68 $\pm$ 2

Chapter 7

Results, conclusions, summary and outlook

In earlier chapters, there has been discussion of the reconstruction of various species of particle. In order to produce meaningful ratios between two different species, it is necessary to include corrections for acceptance and reconstruction efficiency. The transverse mass distributions can also be examined for each species. This chapter shall present fully corrected results and go on to compare them with results from other experiments.

7.1 Corrected Yields and Ratios

Ratios involving strange particles are important because they provide information about the baryochemical and strangeness potentials inside the 'fireball' at the point of hadronisation (see chapter one). The WA94 experiment looks at these ratios in three different kinematic windows. The region defined by $2.5 < Y_{LAB} < 3.0$ and $1.2 < p_{\mathrm{T}} < 3.0$ GeV/c has the greatest acceptance for Ξs and Λs. All points in the $Y - P_{\mathrm{T}}$ plane for which the acceptance for both species of particle is greater than 10% of the maximum acceptance are included in the analysis. Figure 7.1 shows the 'shared region' of greatest acceptance in the $Y - P_{\mathrm{T}}$. The second region under consideration is the so–called 'm_{T}' region, which is used because theoreticians prefer to use transverse mass in their calculations rather than transverse momentum. The WA94 experiment uses the m_{T} region $2.5 < Y_{\mathrm{L}AB} < 3.0$ and $m_{\mathrm{T}} > 1.9$ GeV. The final region, $2.5 < Y_{\mathrm{L}AB} < 3.0$ and $1.0 < p_{\mathrm{T}} < 2.0$ GeV/c, is used to compare results with those from the AFS collaboration's proton–proton data. This region includes a low–p_{T} region which has low acceptance in the WA94 layout so an extrapolation procedure is used and is described later in this chapter.

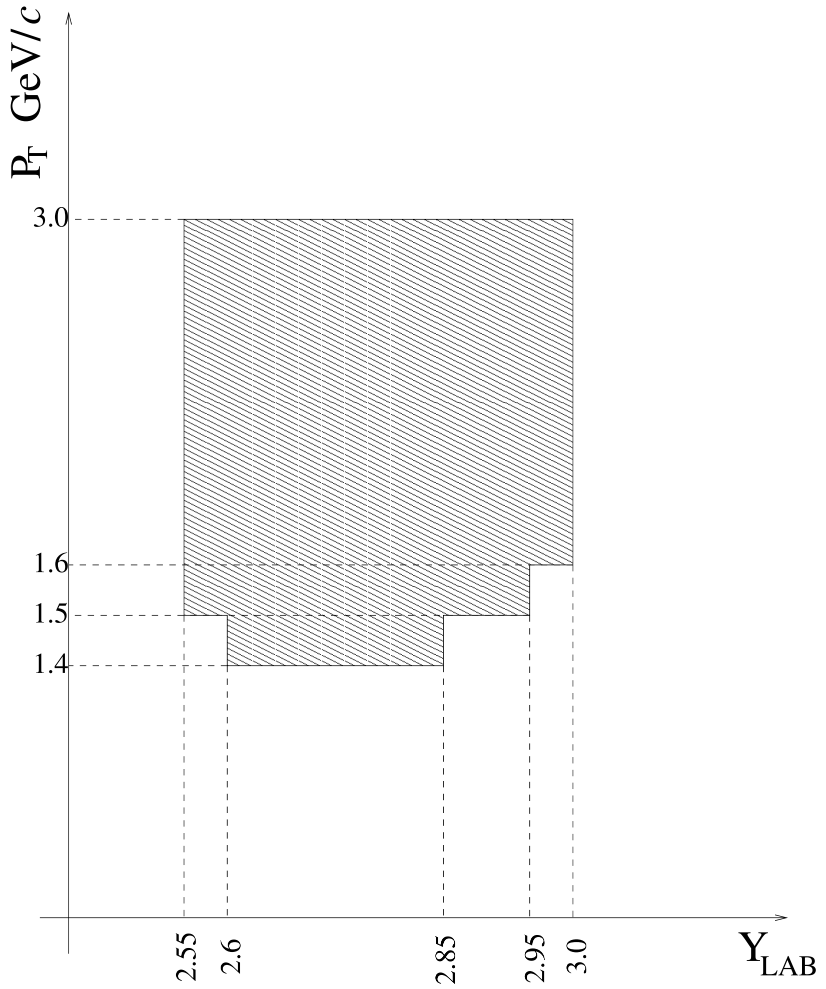

Figure 7.1: The shared region of acceptance for Λs and Ξ^{-}s.

Even after completing all the cuts mentioned in chapter 3, both the Λ and $\overline{\Lambda}$ mass distributions have contamination from K^0 decays. To find the amount of contamination underneath the peaks, the mass of each V^0 is found as if the two tracks were both pions. Figure 7.2 shows the $\pi^+\pi^-$ effective mass versus the $\overline{p}\pi^+$ effective mass for the $\overline{\Lambda}$ candidate. The two vertical lines show the final mass cut which is performed on the $\overline{\Lambda}$ candidate mass. The two diagonal lines represent the Armenteros α cuts. Even with the Armenteros α cuts, it can be seen that there is still some residual contamination from the K^0 reflection. Those candidates with mass within 50 MeV of the K^0 mass and within 25 MeV of the Λ mass are selected as the contamination. The contamination underneath the Λ peak is found to be 1% and that under the $\overline{\Lambda}$ peak is 2%.

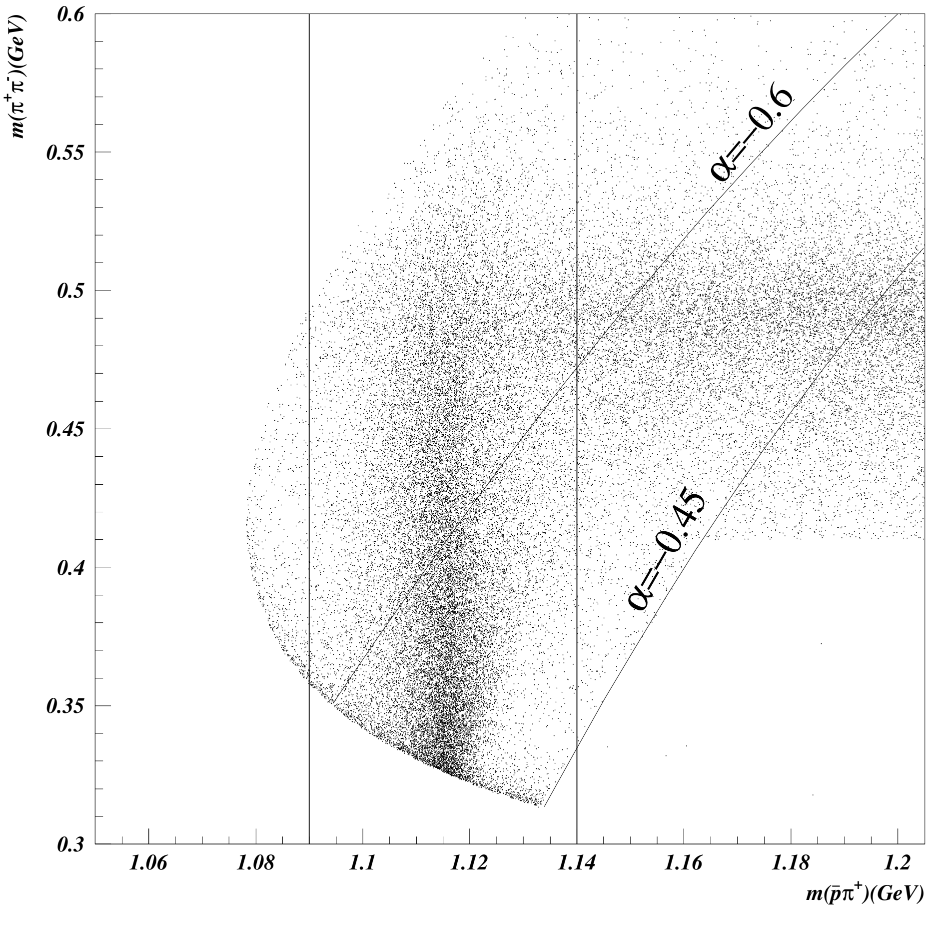

Figure 7.2: $M(\pi^-\pi^+)$ vs $M(\overline{p}\pi^-)$.

Another correction that has to be taken into account is the amount of contamination in the Λ and $\overline{\Lambda}$ samples from the V^0s from $\overline{\Xi}^0$ and Ξ^- decays. Figure 7.3 shows how this contamination occurs. A Λ from a $\overline{\Xi}^0$ or Ξ^- decay could have a momentum four–vector such that it satisfies all the same cuts as a 'proper' Λ from the target. Using a modified version of the reconstruction efficiency chain, Monte Carlo Ξ^-s and $\overline{\Xi}^+$s are generated. Once again, the particles are generated according to the m_T distribution described in chapter six and then mixed with background data. The composite events are passed through the track and V^0 reconstruction programs and then the final analysis program for Λs and $\overline{\Lambda}$s. The amount of contamination is then given by

$$contamination = \frac{n(\Xi_{\mathrm{real}})}{2 \times n(\Xi_{gener.})} \frac{n(\Lambda_{\mathrm{feed}-down}) \times 0.641}{n(\Lambda_{\mathrm{real}})}.$$

The factor $\frac{n(\Xi_{\mathrm{real}})}{n(\Xi_{gener.})}$ normalises the Monte Carlo to the real data and the factor of two is present because the Monte Carlo particles were generated only in the upper hemisphere. The factor of 0.641 takes unseen decay modes of the Λ into account. Contamination from $\overline{\Xi}^0$s and Ξ^0s is calculated in the same way, using the isospin assumption that the number of $\overline{\Xi}^0$s and Ξ^-s produced at the target is the same. The amounts of contamination for each kinematic region and field polarity are shown in tables 7.1 and 7.2. The total contaminations were 16.7% and 29.9% for lambdas and anti–lambdas respectively.

Table 7.1: Feed–down from cascade decays:Shared region.

Particle Species	Contamination from cascade type (%)	
	$\overline{\Xi}^0$	Ξ^-
Λ H $\Uparrow$	11.5 ±0.8	5.3 ± 0.4
Λ H $\Downarrow$	11.1 ± 1.2	5.1 ± 0.6
$\overline{\Lambda}$ H $\Uparrow$	20.5 ± 2.2	8.5 ± 0.9
$\overline{\Lambda}$ H $\Downarrow$	21.6 ± 3.4	10.5± 1.7

After applying all of these corrections, the final ratios for the kinematic region of shared acceptance are shown in table 7.3, along with the corresponding ratios from sulphur–sulphur interactions. It can be seen that the anti–particle/particle ratios stay constant, within errors. More significantly, though, are the changes in the $\frac{\Xi^-}{\Lambda}$ and $\frac{\overline{\Xi}^+}{\overline{\Lambda}}$ when going from proton–sulphur to sulphur–sulphur. Both ratios increase when going

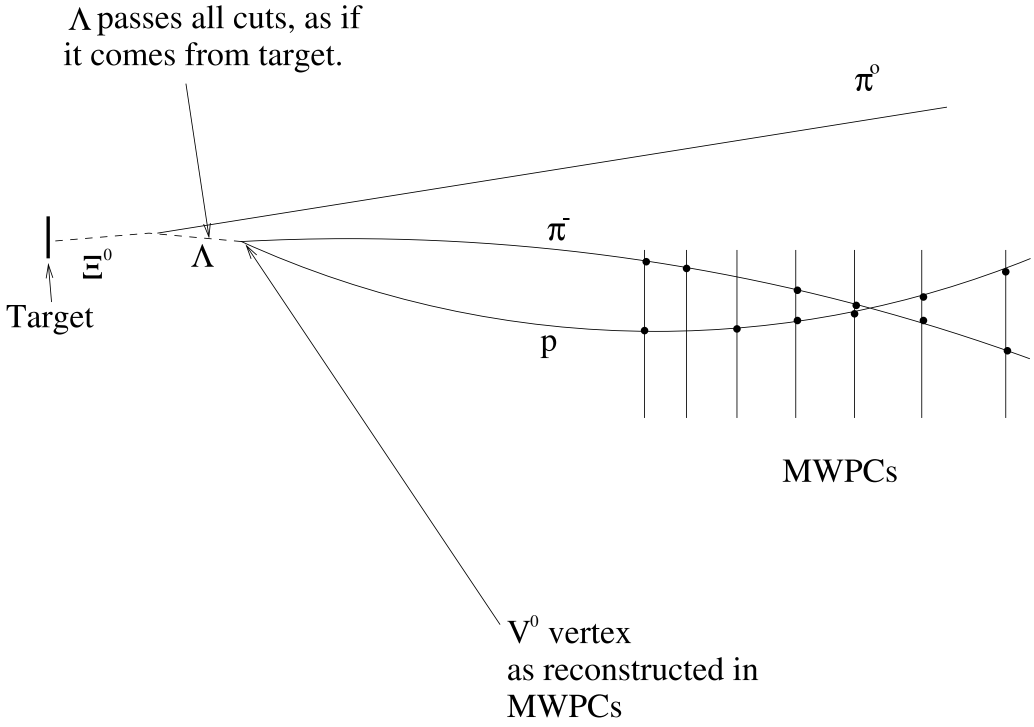

Figure 7.3: How feed–down occurs.

from a proton beam to a sulphur ion beam, the increase in the $\frac{\overline{\Xi}^+}{\overline{\Lambda}}$ ratio being about 30%. This corresponds to a 2σ effect. An effect witnessed also by the WA85 experiment in proton–tungsten and sulphur–tungsten collisions [58]. Table 7.4 shows the ratios in the $m_{\mathrm{T}} > 1.9$ GeV, which would be the ratios that are used by theoreticians.

In order to make an absolute measurement of the amount of strangeness enhancement when going from proton–sulphur to sulphur–sulphur interactions, one requires a normalising factor. This factor is determined by normalising the amount of negative particle production in both proton–sulphur and sulphur–sulphur collisions, since the number of negative particles scales with the number of participating nucleons. The NA35 experiment presented results that showed that this was a valid assumption to make [59]. Sulphur–sulphur and normalised proton–sulphur rapidity distributions were

Table 7.2: Feed–down from cascade decays:transverse mass region.

Particle Species	Contamination from cascade type (%)	
	Ξ^0	Ξ^-
Λ H $\Uparrow$	10.3 $\pm$ 0.7	5.2 $\pm$ 0.4
Λ H $\Downarrow$	10.4 $\pm$ 1.1	5.0 $\pm$ 0.5
$\overline{\Lambda}$ H $\Uparrow$	18.9 $\pm$ 2.1	11.5 $\pm$ 1.3
$\overline{\Lambda}$ H $\Downarrow$	21.3 $\pm$ 3.4	10.9 $\pm$ 1.8

very similar when compared. The absolute strangeness enhancement for any hyperon Y is given by the relation

$$\text{enhancement} = \frac{(Y/h^-)_{SS}}{(Y/h^-)_{pS}}.$$

The enhancements are shown in table 7.5 and in graphical form in figure 7.4. These enhancements are compatible with those from the WA85 experiment.

7.2 Transverse Mass Distributions

Transverse mass distributions are studied because the inverse slope $1/\beta$ from the distribution

$$\left(\frac{1}{m_{\mathrm{T}}}\right)^{\frac{3}{2}} \frac{dN}{dm_{\mathrm{T}}} \propto e^{-m_{\mathrm{T}}\beta}$$

provides information of the temperature of the central fireball [60]. This distribution has been chosen because at present, theoreticians believe that it gives the best description of a cooling thermal source with a flat rapidity distribution. The inverse slope cannot be directly related to the source temperature because of factors such as collective flow (which is related to the expansion of the fireball and results in an increase in the measured inverse slope) and resonance production.

Each hyperon candidate has a value of transverse momentum and rapidity assigned to it which defines a point on the $Y_{LAB} - p_{\mathrm{T}}$ plane. Each point lies in a particular bin

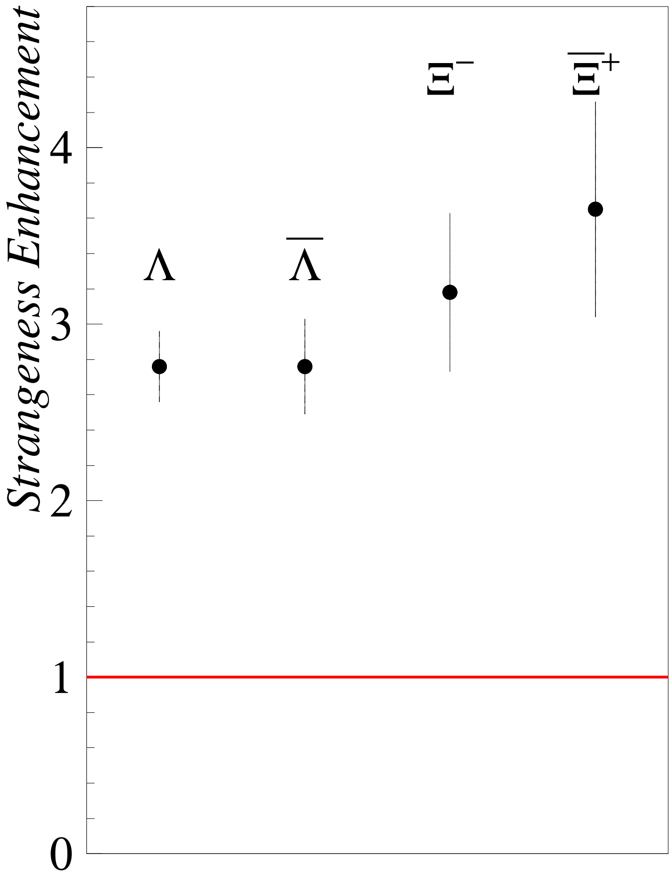

Figure 7.4: Strangeness enhancements.

Table 7.3: Shared region of acceptance table of ratios.

Ratio	WA94	
	pS	SS
$\frac{\overline{\Lambda}}{\Lambda}$	0.22 ± 0.01	0.22 ± 0.01
$\frac{\overline{\Xi}^{+}}{\Xi^{-}}$	0.46 ± 0.05	0.55 ± 0.07
$\frac{\Xi^{-}}{\Lambda}$	0.078 ± 0.004	0.09 ± 0.01
$\frac{\overline{\Xi}^{+}}{\overline{\Lambda}}$	0.16 ± 0.02	0.21 ± 0.02
$\frac{\Lambda}{h^{-}}$	0.137 ± 0.010	0.378 ± 0.020
$\frac{\mathrm{K}^{+}}{\mathrm{K}^{-}}$	2.0 ± 0.2	1.9 ± 0.4

of the acceptance table. The acceptance weight for the candidate is given by 100/acceptance in per cent. The reconstruction efficiency is classified by particle type and average cluster multiplicity per plane and again, the weight is given by 100/efficiency in per cent. The final weight for the event is the product of the two weights. The total weight as a function of tranverse mass is plotted and the distribution above is fitted to it.

Figure 7.5 shows the fully corrected transverse momentum distributions for Λs, $\overline{\Lambda}$s, Ξ^{-}s, $\overline{\Xi}^{+}$s. The distributions for the Λs and $\overline{\Lambda}$s have been corrected bin–by–bin for

Table 7.4: m_{T} region of acceptance table of ratios.

Ratio	WA94	
	pS	SS
$\frac{\overline{\Lambda}}{\Lambda}$	0.20 ± 0.01	0.22 ± 0.01
$\frac{\overline{\Xi}^{+}}{\Xi^{-}}$	0.427 ± 0.05	0.54 ± 0.06
$\frac{\Xi^{-}}{\Lambda}$	0.14 ± 0.01	0.18 ± 0.01
$\frac{\overline{\Xi}^{+}}{\overline{\Lambda}}$	0.30 ± 0.03	0.44 ± 0.04

the feed–down from cascade decays. Figure 7.6 a) and figure 7.6 b) show the same distributions for $K^{\pm}$ and while figure 7.6 c) shows the m_{T} distribution for negative particles. Table 7.6 lists the inverse slopes for each species for both proton–sulphur and sulphur–sulphur collisions. The errors in this table are statistical only and were calculated using the MINOS package [61]. The systematic errors have been estimated using Monte Carlo simulations. Things such as moving the chambers and hodoscopes by a small amount were varied. The effects on the acceptance and reconstruction efficiency yielded systematic errors of about 10 MeV. In the baryonic sector, the Λ and $\overline{\Lambda}$ inverse slopes are 6.2σ and 3.2σ lower, respectively, in proton–sulphur than in sulphur–sulphur collisions. The inverse slopes from the Ξ^{-} and $\overline{\Xi}^{+}$ distributions are lower in proton–proton collisions, but not significantly so. A similar effect was observed by the WA85 experiment. In addition, the inverse slopes for proton–sulphur collisions are consistent with those found from proton–tungsten collisions in the WA85 experiment [58].

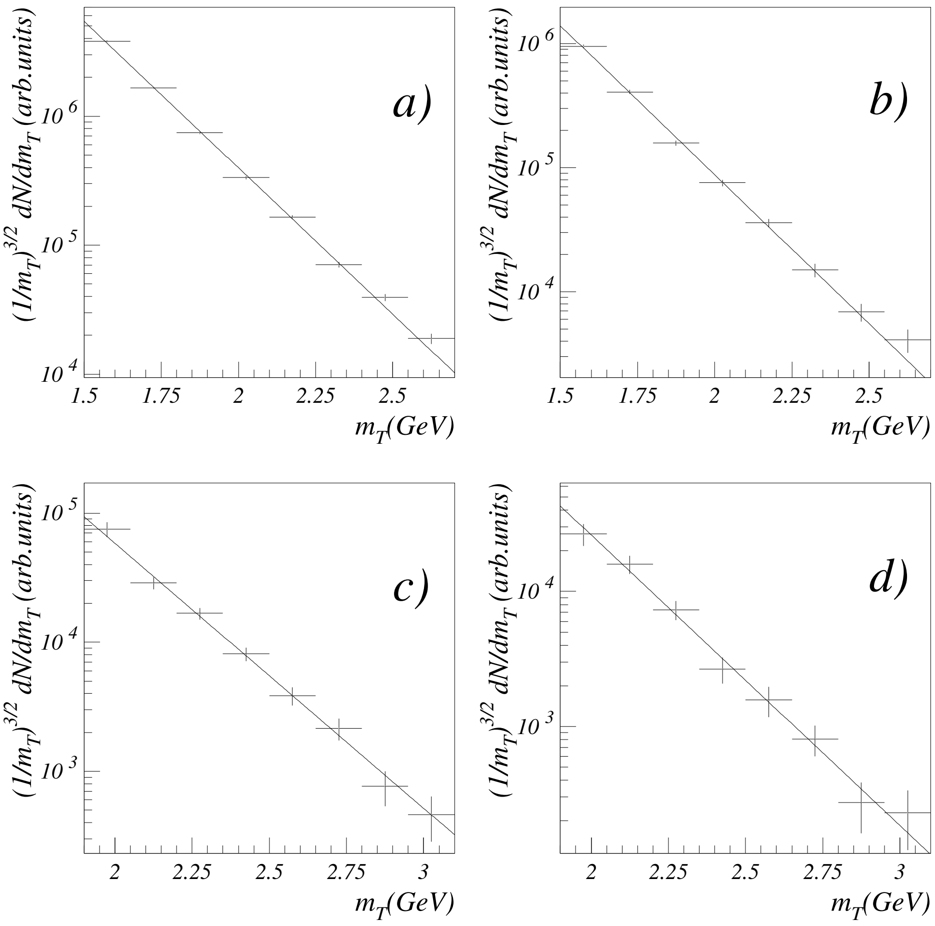

Figure 7.5: Transverse mass distributions for full statistics for a) Λ, b) $\overline{\Lambda}$, c) $\Xi^-$and d) $\overline{\Xi}^+$in proton–sulphur interactions.

Table 7.5: Enhancement factors from the WA94 experiment.

Particle Species	Enhancement factor
Λ	2.76 ± 0.25
$\overline{\Lambda}$	2.76 ± 0.31
Ξ^-	3.18 ± 0.48
$\overline{\Xi}^+$	3.62 ± 0.70

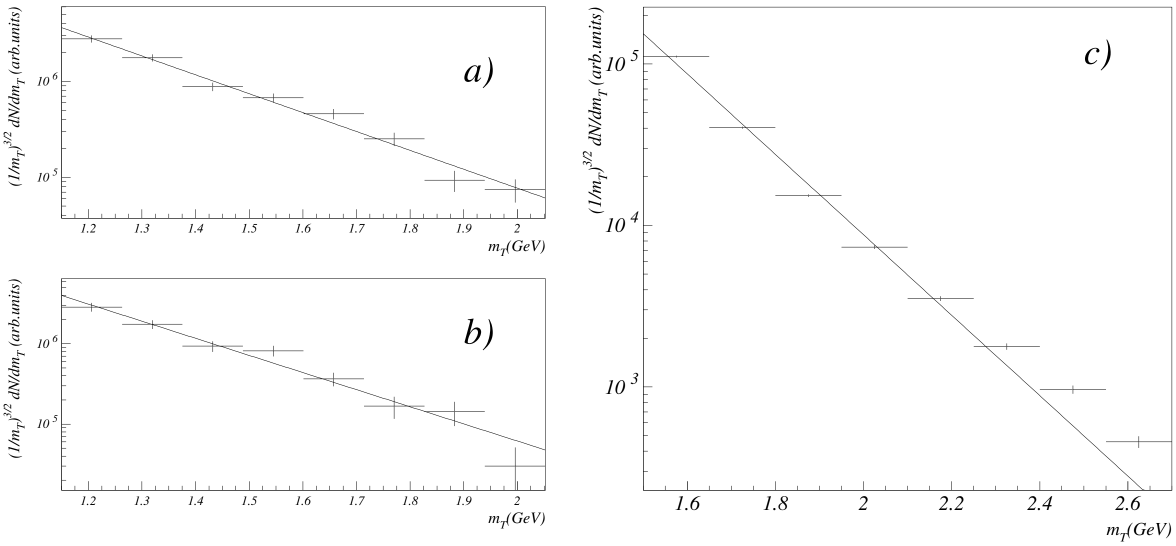

(a) (b)

Figure 7.6: Transverse mass distributions for full statistics for a) K^+, b) K^-, c) h^- in proton–sulphur interactions.

To obtain ratios in the third kinematic region, the transverse mass distributions are extrapolated down to $p_T = 1.0$ GeV/c. This is done to compare WA85 and WA94 results with results from the AFS experiment. In order to get meaningful errors on the ratios, each transverse mass distribution is 'randomised' by spreading each bin with a Poisson distribution one thousand times. An exponential fit is performed, just as described earlier in this chapter, to each of the new distributions. A further program calculates the total yield of each particle by integrating the transverse mass distribution over the range $1.0 < p_T < 2.0$ GeV/c. This gives rise to one thousand values for each of the four hyperon ratios. Each value is plotted in a histogram and the final ratios

Table 7.6: Hyperon inverse slopes for full statistics.

Particle Species	Inverse Slope / MeV	
	pS	SS
h^-	171 $\pm$ 1	-
K^+	220 $\pm$ 20	172 $\pm$ 20
K^-	204 $\pm$ 25	152 $\pm$ 25
Λ	191 $\pm$ 3	213 $\pm$ 2
$\overline{\Lambda}$	181 $\pm$ 5	204 $\pm$ 5
Ξ^-	212 $\pm$ 9	222 $\pm$ 10
$\overline{\Xi}^+$	202 $\pm$ 12	208 $\pm$ 25

and errors are found by fitting a Gaussian to each distribution. These histograms are shown in figure 7.8. The final ratios are shown, along with the corresponding results from sulphur–sulphur collisions, in table 7.7. The WA94 and WA85 results are shown on the same plot as the AFS proton–proton result ($\frac{\overline{\Xi}^+}{\overline{\Lambda}} = 0.06 \pm 0.02$ [62]) in figure 7.7. Both the WA94 and WA85 results show an increase of 30% in the $\frac{\overline{\Xi}^+}{\overline{\Lambda}}$ ratio when going from a proton projectile to a sulphur projectile. This increase corresponds to a 2σ effect. A further interesting point is that the proton–ion collision values are also higher than that for the proton–proton value. Further work is being carried out to explore the proton/light ion system by the WA97 experiment and will be discussed in a later section.

7.3 Comparison with other experiments

Results on cascade and charged kaon production in proton–sulphur interactions are scarce. The bulk of the results from the NA5 [63] and NA35 [64] experiments involve $\frac{V^0}{h^-}$ ratios and cover a larger kinematic window than the WA85 and WA94 experiments. For example, the NA35 experiment found a ratio $\frac{\Lambda}{h^-} = 0.049 \pm 0.006$ in the region $1.0 < Y_{LAB} < 5.0$ and $0.0 < p_T < 2.0$ GeV/c [64]. For the whole phase space, the NA5

Table 7.7: AFS region of acceptance table of ratios.

Ratio	WA94	
	pS	SS
$\frac{\overline{\Lambda}}{\Lambda}$	0.24 ± 0.01	0.24 ± 0.01
$\frac{\overline{\Xi}^+}{\Xi^-}$	0.46 ± 0.08	0.58 ± 0.07
$\frac{\Xi^-}{\Lambda}$	0.068 ± 0.007	0.08 ± 0.01
$\frac{\overline{\Xi}^+}{\overline{\Lambda}}$	0.13 ± 0.02	0.20 ± 0.02

experiment found the ratios shown in table 7.8 [63]. All of these ratios are lower than the one presented in this thesis, but one must remember that the kinematic regions and triggers are very different. The only result which provides a direct comparison with the WA94 result is that presented by the WA85 experiment for proton–tungsten. The WA85 experiment looked in the kinematic region $2.3 < Y_{LAB} < 3.0$ and $1.2 < p_{\mathrm{T}} < 3.0$ GeV/c and found a ratio $\frac{\Lambda}{h^-} = 0.151 \pm 0.010$ [58] , slightly higher than that found in proton–sulphur collisions.

Table 7.8: $\frac{\Lambda}{h^-}$ ratios from the NA5 experiment.

Reaction	$\frac{\Lambda}{h^-}$ ratio
p–p	0.028 ± 0.007
p–Ar	0.086 ± 0.015
p–Xe	0.096 ± 0.020

Table 7.9 shows particle ratios from the NA35 experiment and are quoted for full

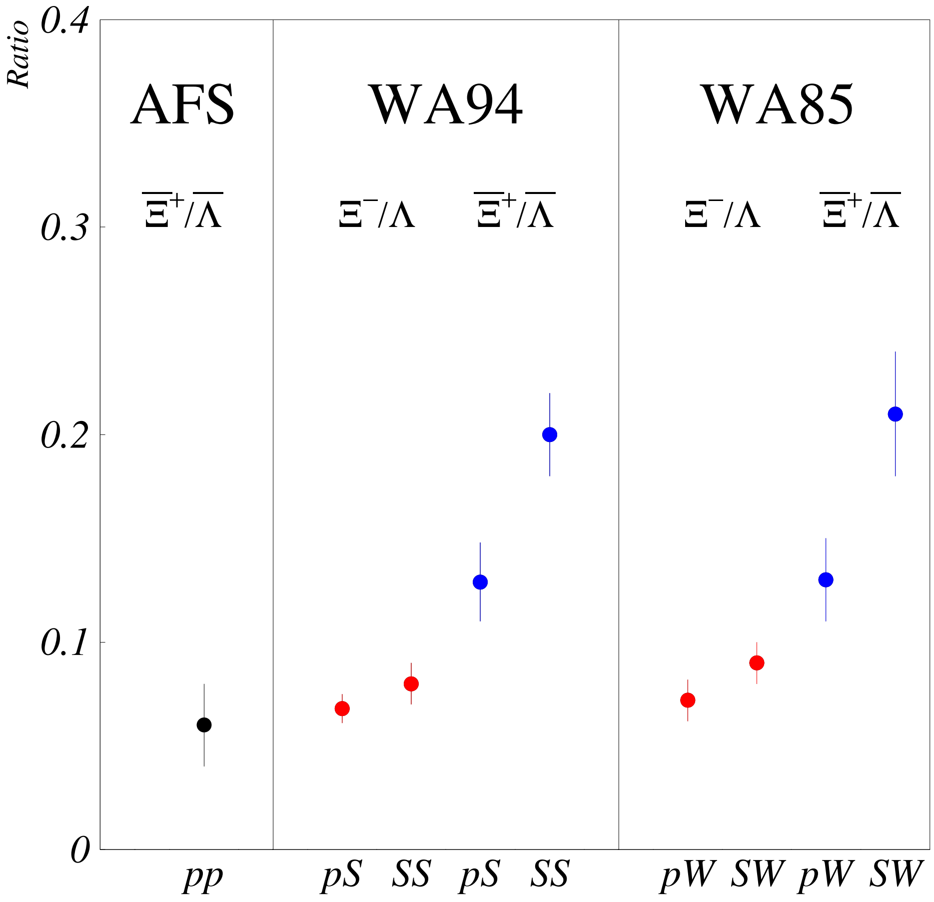

Figure 7.7: Comparison of ratios in the AFS region for the AFS, WA94 and WA85 experiments.

phase space. Using these ratios, one finds an enhancement factor of 1.8 ± 0.3 and 2.5 ± 1.1 for Λ and $\overline{\Lambda}$ particles respectively. These figures compare reasonably with those from the WA94 and WA85 experiments. The WA94 and WA85 results are higher, predominantly because they are from the very central region of the collision, rather than for the entire phase space, which includes not only the hot fireball, but also the target and projectile regions.

The NA35 experiment finds a slope parameter of 172 ± 17 MeV for Λ particles in proton–sulphur collisions[64] in a kinematic window given by $0.8 < Y_{LAB} < 4.2$ and $0.0 < p_{\mathrm{T}} < 1.0$ GeV/c. This result is compatible with the result from the more

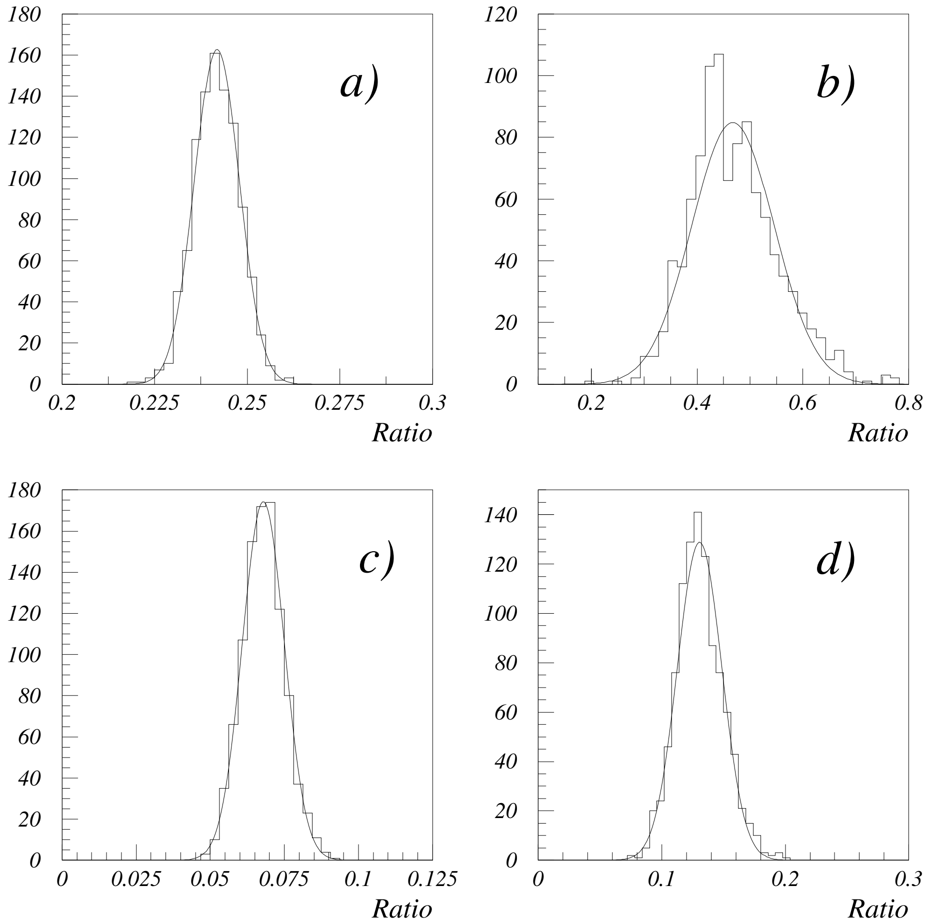

Figure 7.8: Histograms for the four ratios.

narrow kinematic window in the WA94 and WA85 experiments. For negative particles, the WA85 experiment finds an inverse slope parameter of 217±7 MeV for proton–tungsten collisions, which is somewhat higher than that found in proton–sulphur in WA94. These two experiments have slightly different rapidity coverages, which might very well explain the difference in inverse slopes.

Table 7.9: Particle ratios from the NA35 experiment.

Ratio	Value	
	p–S	S–S
$\frac{\overline{\Lambda}}{\Lambda}$	0.13 ± 0.02	0.18 ± 0.06
$\frac{\Lambda}{h^-}$	0.044 ± 0.005	0.080 ± 0.010

7.4 Outlook for heavy ion physics

In November 1994, the first lead beam arrived from the SPS at CERN. Several experiments had been designed, but the successor to the WA94 and WA85 experiments, the WA97 experiment was the first experiment to employ silicon pixel technology. To begin with, there were five pixel planes and ten microstrip planes arranged into a telescope. Each 5 cm $\times$ 5 cm plane of pixels had 72,000 channels, giving much better track momentum resolution than the MWPCs employed before. At present, 162 million triggers have been analysed from both proton–lead and lead–lead interactions at 158 GeV/c per nucleon. The resulting uncorrected mass distributions for Ξs and Ωs are shown in figure 7.9.

One of the more interesting features of the WA97 experiment is its ability to reconstruct large numbers of Ω^- and $\overline{\Omega}^+$ particles which were first seen in heavy–ion interactions in the WA85 experiment [65]. For the first time in heavy ion interactions, these truly strange particles can be accurately studied and relative yields and ratios with Ξ^- and $\overline{\Xi}^+$ particles can be formed. Table 7.10 shows these ratios from lead–lead collisions [66]. By comparing the mass plots for Ξs and Ωs from proton–lead and lead–lead collisions and by bearing in mind the small difference in acceptance corrections, it seems that Ω particles are enhanced by a factor of about three compared to the Ξ particles. Given that the Ξ particles are enhanced by a factor of about 3.5 when going from proton–sulphur to sulphur–sulphur, the enhancement factor for Ωs going from proton–lead to lead–lead collisions could be higher than ten.

The final part of the WA97 experiment was a proton beam incident on a beryl-

Table 7.10: Hyperon ratios from the WA97 experiment.

Ratio	Enhancement factor
$\frac{\overline{\Xi}^+}{\Xi^-}$	0.27 $\pm$ 0.05
$\frac{\overline{\Omega}^+}{\Omega^-}$	0.42 $\pm$ 0.12
$\frac{\Omega^-}{\Xi^-}$	0.19 $\pm$ 0.04
$\frac{\overline{\Omega}^+}{\overline{\Xi}^+}$	0.30 $\pm$ 0.09
$\frac{\Xi^-+\overline{\Xi}^+}{\Omega^-+\overline{\Omega}^+}$	0.21 $\pm$ 0.03

lium target. The proton–beryllium system is by far the lightest system studied in the OMEGA series of heavy–ion experiments and would be the closest approximation to a proton–proton system. It would also serve as a check on the AFS proton–proton $\frac{\overline{\Xi}^+}{\overline{\Lambda}}$ result and to provide a benchmark for proton–nucleon $\frac{\Omega}{\Xi}$ ratios in both proton–lead and lead–lead interaction.

The NA57 experiment [37], due to start taking data in 1997, intends to explore the boundary between the hadron gas phase and the QGP phase as described in chapter one. Runs will be performed at two different beam energies, 44 GeV/nucleon and 158 GeV/nucleon for the lead beam. It is predicted that lowering the beam energy will switch off the strangeness enhancement observed so far in previous heavy ion experiments. A further refinement incorporated into the NA57 experiment are three stations of two pixel planes, designed to sample the charged particle asymmetry. This can, in turn, be used to deduce the entropy per baryon of the lead–lead collisions, measuring another potential signal of Quark–Gluon Plasma formation, as described in chapter one.

For the long term future, the prospects of exploring Quark–Gluon Plasmas are good. The Relativistic Heavy Ion Collider at Brookhaven should be taking data by the turn of the century at 100+100 GeV per nucleon. Two experiments, STAR [67] and PHENIX [68] will be looking at gold–gold collisions. STAR will be looking at mainly hadronic signals and PHENIX J/Ψ suppression and photon production, amongst other things.

The latest planned experiment for investigating heavy–ion collisions, the ALICE experiment [69] at the Large Hadron Collider at CERN (figure 7.10), is designed to cover 2π in azimuthal angle and greater than $\pm 45°$ from the beam. It will measure many different proposed signals of the Quark–Gluon Plasma. It shall be able to measure some strange particle ratios on an event–by–event basis. Figure 7.11 shows Monte Carlo invariant mass distributions. There is also a muon detector, covering very forward rapidities, designed to measure hidden charm and beauty particle decays. This would show up J/Ψ and Ψ' as well as Υ, Υ' and Υ'' supression. It is predicted that the ALICE experiment will look in the low baryon density and high temperature region of the phase diagram, much closer to the conditions in the early universe than the experiments of the SPS.

7.5 Conclusions

Observation of strangeness enhancements such as those presented in this thesis are difficult to explain using a solely hadronic model for heavy–ion collisions. This would seem to indicate that experiments at the SPS at CERN are close to the phase boundary and that the WA97 experiment is possibly probing into the edge of mixed phase area. The RHIC and ALICE experiments planned for the very near future, should, if the theoretical predictions are accurate, thoroughly investigate the phase of matter which existed so early on in our universe.

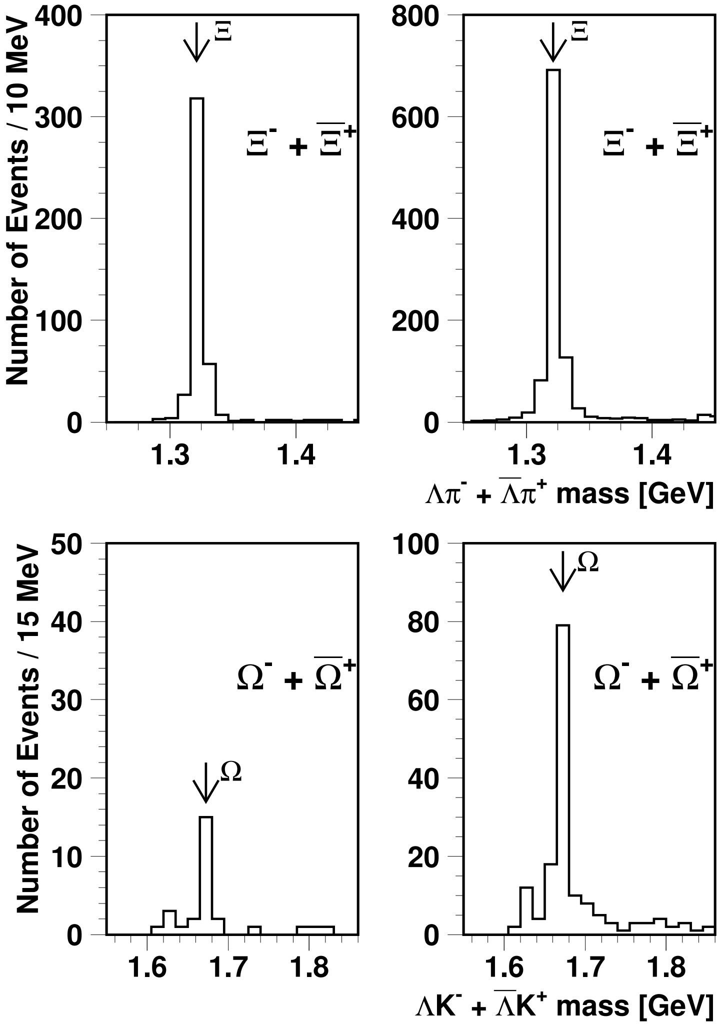

Figure 7.9: Effective mass distributions for a) Ξ and b) Ω candidates from the WA97 experiment.

Figure 7.10: Layout for the proposed ALICE experiment.

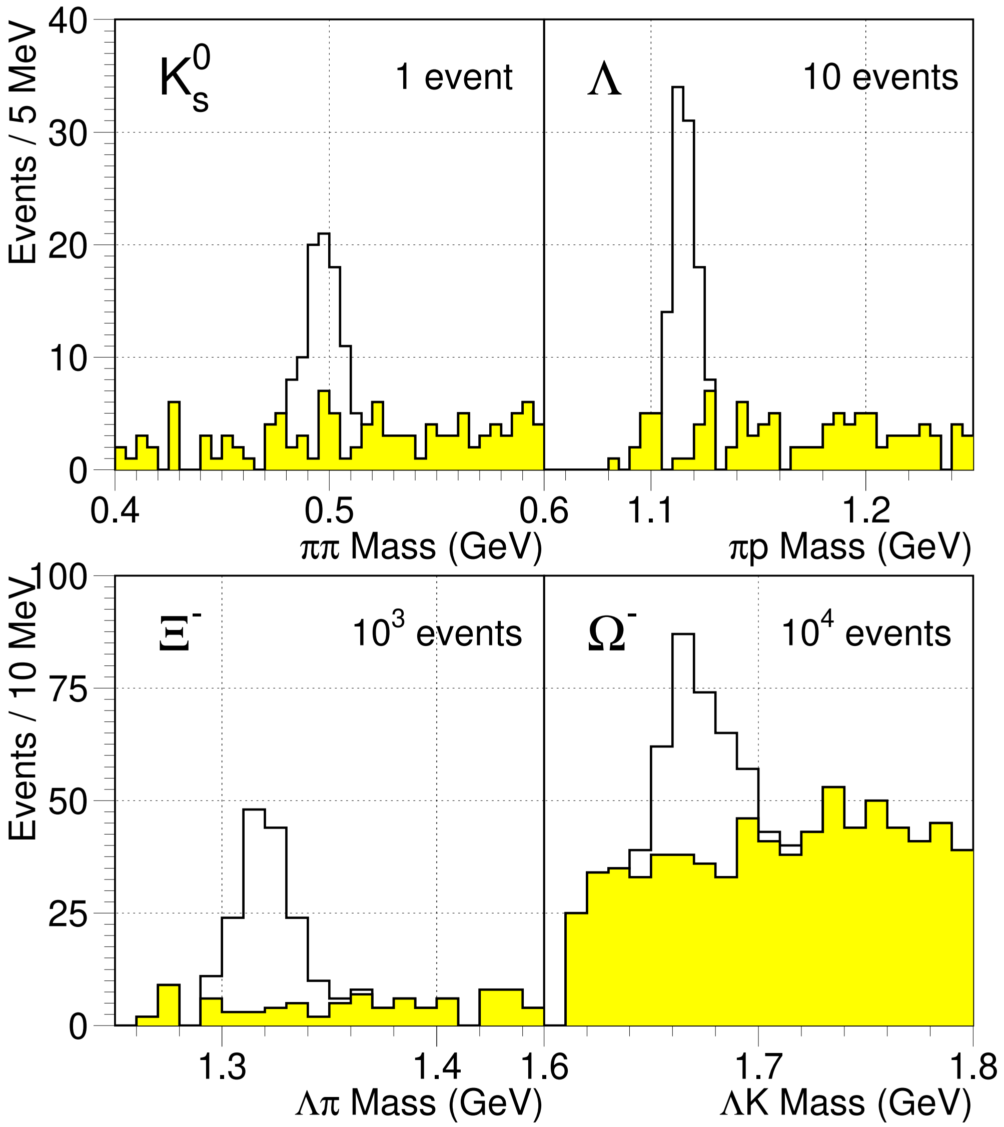

Figure 7.11: Effective mass distributions for four species of particles from ALICE Monte Carlo studies.

Appendix A

Armenteros-Podolanski Plots

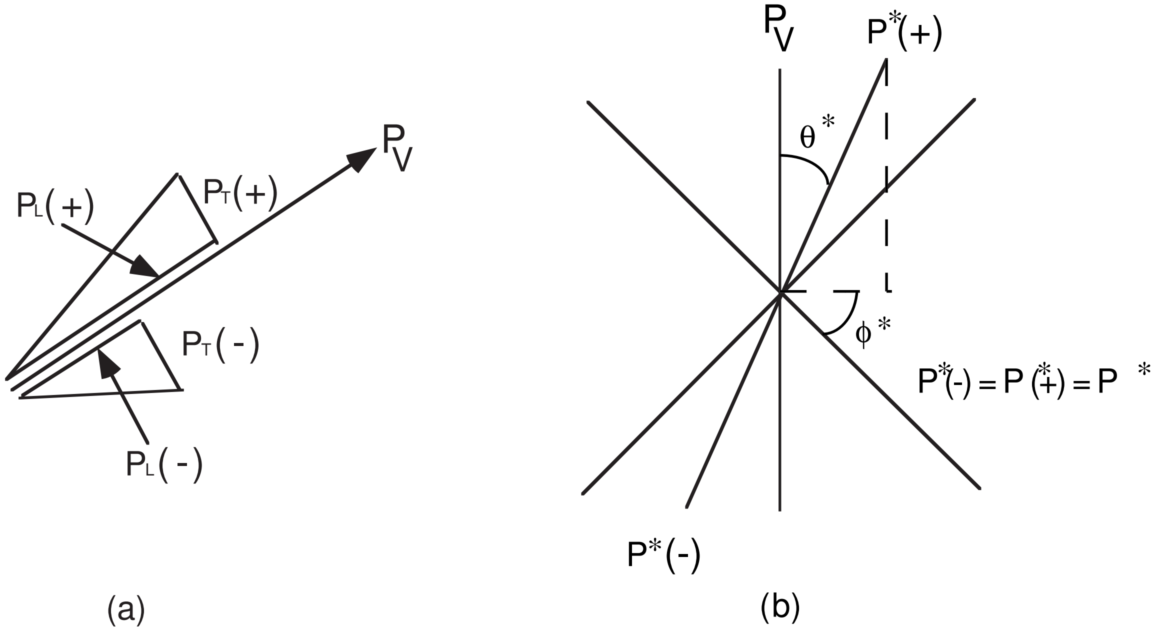

Figure A.1: Schematic representation of a V^0 decay in a) the lab frame and b) the V^0's centre-of-mass frame.

Figure A.1 (a) illustrates a V^0 decay into a positive and negative particle. The tracks have logitudinal momentum components $p_L(+)$ and $p_L(-)$ and transverse momentum components $p_T(+)$ and $p_T(-)$ with respect to the V^0's direction of motion. In the centre-of-mass frame, (shown in figure A.1 (b)) the momentum components are,

$$p_L^*(+) = p^* \cos\theta,$$

$$p_T^*(+) = p^* \sin\theta,$$

$$E^*(+) = \sqrt{p^{*^2} + m^2(+)}.$$

To transform to the lab frame requires Lorentz transformations, which in matrix form are given by [6]

$$\begin{pmatrix} E \\ p_L \end{pmatrix} = \begin{pmatrix} \gamma & \gamma\beta \\ \gamma\beta & \gamma \end{pmatrix} \begin{pmatrix} E^* \\ p_L^* \end{pmatrix}, \qquad p_T^* = p_T$$

where $\gamma = 1/\sqrt{1-\beta^2}$ and β is the velocity of the lab in the particle's rest frame. This gives

$$E^{Lab}(+) = \gamma E^*(+) + \gamma\beta p_L^*(+)$$

$$p_L^{Lab}(+) = \gamma p_L^*(+) + \gamma\beta E^*(+) = \gamma p^* \cos\theta^* + \gamma\beta E^*(+)$$

$$p_T^{Lab}(+) = p_T^*(+) = p^* \sin\theta^*$$

i.e.

$$p_L^{Lab}(+) = \gamma p^* \cos\theta^* + \gamma\beta E^*(+)$$

$$p_L^{Lab}(-) = -\gamma p^* \cos\theta^* + \gamma\beta E^*(-)$$

therefore

$$p_L^{Lab}(+) - p_L^{Lab}(-) = 2\gamma p^* \cos\theta^* + \beta\gamma(E^*(+) - E^*(-))$$

$$p_L^{Lab}(+) + p_L^{Lab}(-) = p_L^{Lab} = \beta\gamma m_V^0.$$

The Armenteros-Podolanski variable, α, is defined by [55]

$$\alpha = \frac{p_L^{Lab}(+) - p_L^{Lab}(-)}{p_L^{Lab}(+) + p_L^{Lab}(-)} = \frac{2p^*\cos\theta^*}{\beta m_V^0} + \frac{E^*(+) - E^*(-)}{m_V^0} = \zeta\cos\theta^* + \varphi$$

Table A.1: Armenteros-Podolanski quantities.

Decay	ζ	p^* (GeV/c)	α_{min}	α_{max}	φ
$K_S^0 \rightarrow \pi^+\pi^-$	0.8282	0.206	-0.828	+0.8282	0.
$\Lambda \rightarrow p\pi^-$	0.179	0.101	+0.515	0.873	0.694
$\overline{\Lambda} \rightarrow \overline{p}\pi^+$	0.179	0.101	-0.873	-0.515	-0.694

therefore

$$\cos\theta^* = \frac{\alpha - \varphi}{\zeta} \qquad \sin\theta^* = \frac{p_T^*}{p^*}$$

$$\cos^2\theta^* + \sin^2\theta^* = 1 = (\frac{\alpha - \varphi}{\zeta})^2 + (\frac{p_T^*}{p^*})^2.$$

This is an equation of an ellipse with centre (φ,0) and semi-axis in α of length ζ, and in p_T length p^*. Table A.1 shows the value of these variables for the decays of Λs, $\overline{\Lambda}$s and K^0s, whilst the theoretical plots for Λs, $\overline{\Lambda}$s and K^0s are shown in figure A.2.

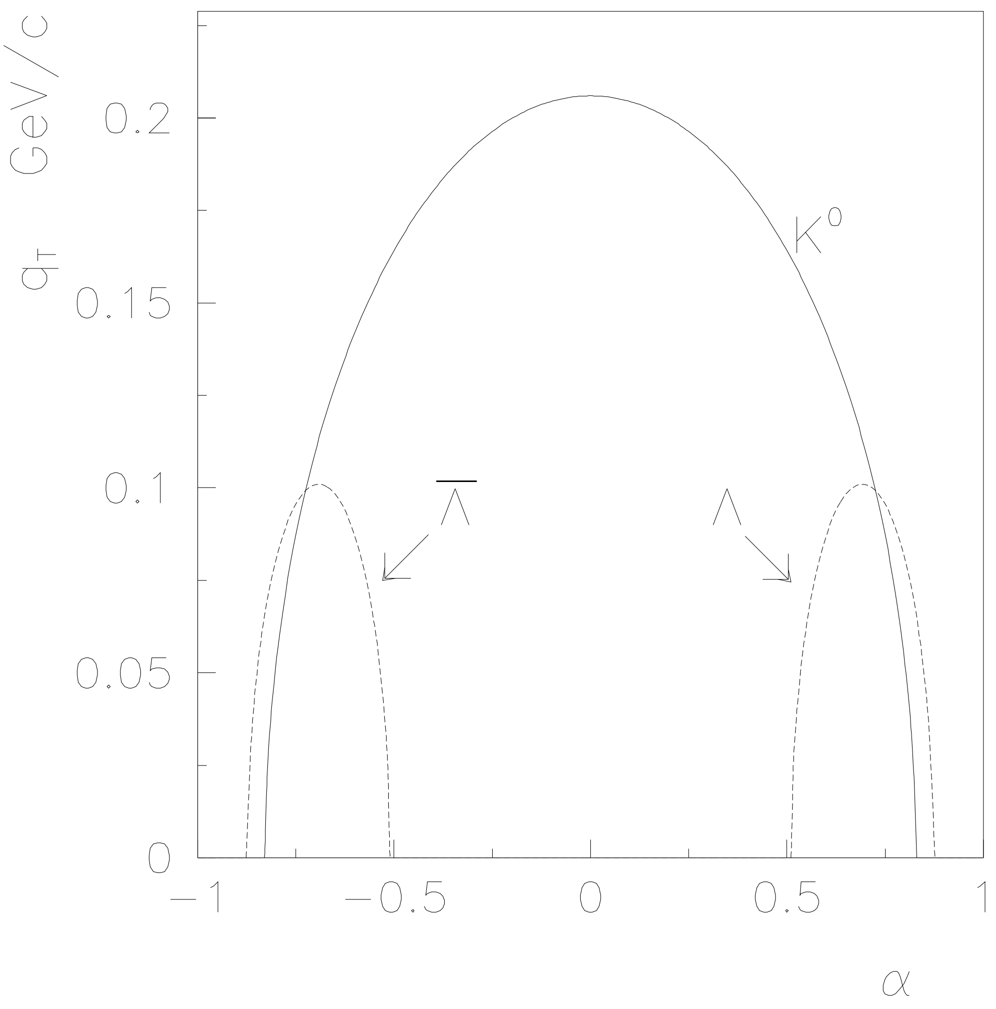

Figure A.2: Podolanski-Armenteros regions for different V^0 candidates.

Appendix B

Acceptance Tables

The geometrical acceptances of unambiguous Λs $(0.45 < |\alpha| < 0.60)$ and Ξ^-s for the experimental layout and trigger used in the WA94 1993 proton-sulphur run are given in the following tables, as a function of rapidity, $Y_{\mathrm{L}AB}$, and transverse momentum, p_{T}. The acceptances of the corresponding antiparticles are the same due to the symmetry of the magnetic field and apparatus. Unseen decay modes and decays outside the fiducial region are included in the acceptance tables.

Table B.1: Acceptances for Λs produced in p-S interactions (in *per cent*).

Y_{LAB}	2.525	2.575	2.625	2.675	2.725	2.775	2.825	2.875	2.925	2.975
p_T = 0.85 GeV/c	0.043	0.053	0.060	0.063	0.063	0.060	0.044	0.016	0.000	0.000
p_T = 0.95 GeV/c	0.066	0.077	0.095	0.103	0.109	0.106	0.098	0.083	0.047	0.002
p_T = 1.05 GeV/c	0.084	0.112	0.133	0.147	0.163	0.170	0.168	0.155	0.126	0.079
p_T = 1.15 GeV/c	0.087	0.144	0.173	0.202	0.226	0.239	0.242	0.235	0.212	0.174
p_T = 1.25 GeV/c	0.089	0.155	0.222	0.260	0.294	0.316	0.323	0.318	0.302	0.263
p_T = 1.35 GeV/c	0.092	0.155	0.259	0.317	0.360	0.393	0.403	0.409	0.401	0.355
p_T = 1.45 GeV/c	0.101	0.163	0.259	0.369	0.424	0.461	0.484	0.494	0.474	0.445
p_T = 1.55 GeV/c	0.095	0.163	0.256	0.412	0.481	0.519	0.561	0.564	0.557	0.521
p_T = 1.65 GeV/c	0.094	0.161	0.256	0.408	0.537	0.588	0.607	0.629	0.622	0.594
p_T = 1.75 GeV/c	0.095	0.158	0.253	0.386	0.576	0.631	0.655	0.687	0.676	0.653
p_T = 1.85 GeV/c	0.089	0.158	0.245	0.383	0.595	0.683	0.708	0.734	0.733	0.702
p_T = 1.95 GeV/c	0.089	0.150	0.242	0.381	0.599	0.723	0.765	0.779	0.768	0.755
p_T = 2.05 GeV/c	0.087	0.151	0.231	0.372	0.576	0.758	0.798	0.806	0.810	0.785
p_T = 2.15 GeV/c	0.086	0.152	0.231	0.365	0.560	0.779	0.822	0.839	0.838	0.819
p_T = 2.25 GeV/c	0.081	0.143	0.225	0.360	0.546	0.807	0.853	0.871	0.876	0.851
p_T = 2.35 GeV/c	0.081	0.143	0.226	0.350	0.547	0.830	0.879	0.892	0.902	0.872
p_T = 2.45 GeV/c	0.079	0.141	0.219	0.346	0.542	0.829	0.901	0.916	0.926	0.898
p_T = 2.55 GeV/c	0.076	0.138	0.218	0.340	0.532	0.818	0.928	0.946	0.934	0.923
p_T = 2.65 GeV/c	0.075	0.136	0.219	0.335	0.534	0.805	0.937	0.958	0.949	0.946
p_T = 2.75 GeV/c	0.073	0.134	0.215	0.332	0.516	0.777	0.955	0.966	0.974	0.952
p_T = 2.85 GeV/c	0.071	0.131	0.218	0.334	0.512	0.767	0.966	0.976	0.988	0.966
p_T = 2.95 GeV/c	0.070	0.131	0.213	0.331	0.509	0.760	0.977	0.992	0.990	0.986

Table B.2: Acceptances for Ξ^-s produced in p-S interactions (in *per cent*).

Y_{LAB}	2.525	2.575	2.625	2.675	2.725	2.775	2.825	2.875	2.925	2.975
p_T = 1.25 GeV/c	0.040	0.044	0.049	0.051	0.054	0.054	0.051	0.041	0.028	0.014
p_T = 1.35 GeV/c	0.069	0.079	0.086	0.089	0.094	0.097	0.088	0.078	0.066	0.045
p_T = 1.45 GeV/c	0.104	0.120	0.133	0.140	0.147	0.149	0.144	0.134	0.112	0.086
p_T = 1.55 GeV/c	0.134	0.166	0.196	0.203	0.206	0.209	0.207	0.193	0.174	0.143
p_T = 1.65 GeV/c	0.162	0.217	0.251	0.270	0.278	0.277	0.276	0.263	0.235	0.206
p_T = 1.75 GeV/c	0.193	0.249	0.314	0.343	0.356	0.350	0.346	0.324	0.299	0.273
p_T = 1.85 GeV/c	0.219	0.286	0.356	0.412	0.427	0.432	0.417	0.401	0.368	0.335
p_T = 1.95 GeV/c	0.249	0.313	0.409	0.480	0.498	0.492	0.489	0.465	0.435	0.398
p_T = 2.05 GeV/c	0.263	0.342	0.445	0.530	0.573	0.569	0.561	0.534	0.503	0.452
p_T = 2.15 GeV/c	0.286	0.373	0.475	0.577	0.642	0.641	0.624	0.596	0.564	0.512
p_T = 2.25 GeV/c	0.293	0.393	0.505	0.615	0.702	0.698	0.693	0.652	0.614	0.568
p_T = 2.35 GeV/c	0.304	0.411	0.524	0.644	0.747	0.767	0.748	0.711	0.664	0.609
p_T = 2.45 GeV/c	0.312	0.419	0.544	0.671	0.804	0.818	0.799	0.759	0.711	0.656
p_T = 2.55 GeV/c	0.317	0.422	0.562	0.688	0.844	0.872	0.841	0.801	0.759	0.683
p_T = 2.65 GeV/c	0.325	0.430	0.565	0.700	0.861	0.907	0.887	0.847	0.784	0.716
p_T = 2.75 GeV/c	0.321	0.429	0.580	0.724	0.877	0.952	0.934	0.879	0.810	0.744
p_T = 2.85 GeV/c	0.332	0.426	0.580	0.726	0.893	0.983	0.966	0.908	0.845	0.766
p_T = 2.95 GeV/c	0.329	0.427	0.578	0.745	0.899	1.008	0.990	0.934	0.863	0.786

Table B.3: Acceptances for K^+s produced in p-S interactions per ten thousand.

Y_{LAB}	2.525	2.575	2.625	2.675	2.725	2.775	2.825	2.875	2.925	2.975	3.025	3.075	3.125	3.175
p_{T} = 0.95 GeV/c	28	36	39	44	48	46	45	40	37	30	23	16	9	3
p_{T} = 1.05 GeV/c	33	41	51	58	64	68	64	60	52	45	37	29	18	9
p_{T} = 1.15 GeV/c	38	46	52	64	76	78	79	72	65	59	50	39	29	17
p_{T} = 1.25 GeV/c	38	46	55	67	81	89	88	83	73	65	58	46	36	23
p_{T} = 1.35 GeV/c	39	46	56	67	86	95	96	89	80	73	64	52	41	29
p_{T} = 1.45 GeV/c	40	48	55	67	87	99	96	91	82	72	65	55	45	33
p_{T} = 1.55 GeV/c	37	43	54	66	82	98	98	92	80	75	65	57	46	34
p_{T} = 1.65 GeV/c	36	43	51	64	82	97	97	91	82	73	65	58	46	34
p_{T} = 1.75 GeV/c	33	40	45	59	76	94	94	88	80	71	64	55	46	33
p_{T} = 1.85 GeV/c	32	39	44	56	76	89	90	84	75	67	62	53	41	34
p_{T} = 1.95 GeV/c	29	35	42	53	70	89	87	84	75	67	59	49	41	32
p_{T} = 2.05 GeV/c	28	33	40	51	65	82	85	78	69	63	57	47	40	30

Table B.4: Acceptances for π^{-}s produced in p-S interactions (in *per cent*) (Part 1).

Y_{LAB}	2.525	2.575	2.625	2.675	2.725	2.775	2.825	2.875	2.925	2.975	3.025	3.075
p_{T} = 0.95 GeV/c	4.409	4.817	5.289	5.807	6.470	7.354	8.867	13.948	13.281	12.587	8.885	11.663
p_{T} = 1.05 GeV/c	4.338	4.757	5.249	5.802	6.427	7.386	8.694	15.113	14.221	14.580	10.658	13.632
p_{T} = 1.15 GeV/c	4.505	4.800	5.197	5.775	6.467	7.328	9.771	16.372	15.940	15.100	11.724	15.298
p_{T} = 1.25 GeV/c	4.487	4.738	5.235	5.703	6.377	7.313	10.540	16.504	16.840	15.708	13.715	15.547
p_{T} = 1.35 GeV/c	3.825	4.610	5.202	5.758	6.371	7.652	11.109	17.455	16.720	15.886	14.476	15.921
p_{T} = 1.45 GeV/c	2.277	2.978	3.748	4.627	5.537	7.907	10.917	18.213	16.806	16.735	15.108	16.065
p_{T} = 1.55 GeV/c	1.179	1.807	2.459	3.413	4.367	6.945	10.273	17.828	16.261	16.958	15.351	16.667
p_{T} = 1.65 GeV/c	.220	.842	1.651	2.435	3.669	6.087	9.326	17.189	15.429	16.655	15.293	16.890
p_{T} = 1.75 GeV/c	.973	1.028	1.687	2.490	3.785	5.502	9.066	16.435	14.574	16.357	14.741	16.849
p_{T} = 1.85 GeV/c	1.812	1.873	1.963	2.704	4.256	6.168	9.183	16.307	13.998	15.754	14.431	16.639
p_{T} = 1.95 GeV/c	2.586	2.606	2.331	3.013	4.730	6.616	9.434	16.403	14.276	15.467	14.158	16.240

Table B.5: Acceptances for π^-s produced in p-S interactions (in *per cent*) (part 2).

Y_{LAB}	2.525	2.575	2.625	2.675	2.725	2.775	2.825	2.875	2.925	2.975	3.025	3.075
$p_T = 2.05$ GeV/c	2.987	3.098	3.088	2.885	5.219	6.952	10.024	16.738	14.165	16.070	14.121	16.086
$p_T = 2.15$ GeV/c	2.957	3.451	3.608	3.546	5.021	7.209	10.154	17.302	14.449	15.984	14.478	16.012
$p_T = 2.25$ GeV/c	2.967	3.486	4.035	4.123	5.194	7.515	10.502	17.667	14.538	16.288	14.549	16.430
$p_T = 2.35$ GeV/c	2.817	3.438	4.162	4.462	5.358	7.802	10.754	17.951	14.566	16.546	15.092	16.548
$p_T = 2.45$ GeV/c	2.718	3.350	4.104	5.152	5.915	7.927	10.619	18.092	14.941	16.785	15.441	16.288
$p_T = 2.55$ GeV/c	2.580	3.308	3.914	5.413	6.020	7.956	10.934	18.469	15.204	16.699	15.865	16.538
$p_T = 2.65$ GeV/c	2.528	3.194	3.821	5.353	6.482	8.140	10.936	18.581	15.432	16.762	15.851	16.632
$p_T = 2.75$ GeV/c	2.426	3.111	3.695	5.480	6.880	8.163	11.331	18.509	15.504	17.014	16.136	16.985
$p_T = 2.85$ GeV/c	2.380	3.020	3.674	5.567	7.120	8.186	11.380	18.636	15.682	17.255	16.006	17.446
$p_T = 2.95$ GeV/c	2.249	2.980	3.573	5.362	7.302	8.444	11.579	18.645	15.845	17.471	16.100	17.654
$p_T = 3.05$ GeV/c	2.148	2.858	3.561	5.397	7.282	8.840	11.612	18.880	15.641	17.641	16.177	17.679

Bibliography

[1] WA85 Technical Proposal, CERN/SPSC/84-76 (1984); CERN/SPSC/87-18 P206 Add. (1987); CERN/SPSC/88-20 P206 Add. (1988).

[2] WA94 Technical Proposal, CERN/SPSLC/91-5 (1991).

[3] J. Rafelski and B. Müller, Phys. Rev. Lett. **48** (1982) 1066.

[4] L. van Hove, *Quark Gluon Plasma and Multiparticle Production*, CERN-TH 5236/88.

[5] B. Müller, *The Physics of the Quark Gluon Plasma*, Springer-Verlag, (1985).

[6] D.H. Perkins, *Introduction to High Energy Physics*, Addison-Wesley Publishing Company, Third Edition (1987) 291-297.

[7] R. P. Feynman, *Quantum Electrodynamics*, Benjamin Press, New (1962).

[8] F. Halzen and A. D. Martin, *Quarks and Leptons: An Introductory Course in Modern Particle Physics*, John Wiley and Sons (1984).

[9] A. Chodos, R. L. Jaffe, K. Johnson, C. B. Thorn and V. F. Weisskopf, Phys. Rev **D9** (1974) 4371.

[10] K. Johnson, Acta Phys. Pol. **B6** (1975) 865.

[11] J. Cleymans *et al.*, Phys. Rep. 130 (1986) 217.

[12] S. Gottlieb *et al.*, Phys. Rev. **D35** (1987) 3972.

[13] D. J. Gross and F. Wilczek, Phys. Rev. **D8**, (1973) 3633.

[14] J. Barrette *et al.*, Phys. Rev. **C45** (1992) 819.

[15] H. Hamagaki (E866 Coll.), Nucl. Phys. **A566** (1994) 27c-34c.

[16] R. Stock, Nucl. Phys. **A525** (1991) 221c.

[17] M. Jacob, *In Search of Quark Matter*, CERN-TH 7343/94.

[18] T. C. Awes (WA80 Coll.), Nucl. Phys. **A590** (1995) 81c-92c.

[19] P. Wurm, Nucl. Phys. **A590** (1995) 103c-116c.

[20] NA45 technical proposals, SPSC/CERN/88-25, SPSC/P237; CERN/SPSC/94-01.

[21] R. Baur *et al.*, Z. Phys. **C71** (1996) 571.

[22] R. Albrecht *et al.*, Z. Phys. **C51** (1991) 1.

[23] R. Albrecht *et al.*, CERN-PPE/95-186.

[24] S. Ramos (NA38 Coll.), Nucl. Phys. **A590** (1995) 117c-126c.

[25] T. Ullrich *et al.*, Nucl. Phys. **A610** (1996) 317c-330c.

[26] I. J. R. Aitcheson and A. J. G. Hey, *Gauge Theories in Particle Physics, 2nd. edition*, IOP Publishing (1989).

[27] S. Adler and R. F. Dashen, *Current Algebras*, Benjamin (1968).

[28] S. Weinberg, Phys. Rev. Lett. **18** (1967) 507.

[29] Particle Data Group, Phys. Rev. **D50** (1994) 1172-1825.

[30] M. Masera (HELIOS Coll.), Nucl. Phys. **A590** (1995) 93c-102c.

[31] T. Matsui and H. Satz, Phys. Lett. **B178** (1986) 416.

[32] F. Karsch and R. Petronzio, Phys. Lett. **B193** (1987) 105.

[33] M. C. Abreu *et al.*, Nucl. Phys. **A610** (1996) 404c-417c.

[34] C. Gerschel and J. Hüffner, Z. Phys. **C56** (1992) 71.

[35] S. Gavin and R. Vogt, Report Number LBL 37980 (1996).

[36] J. Letessier, A. Tounsi, U. Heinz, J. Sollfrank and J. Rafelski, Phys. Rev. Lett. 70 (1993) 3530.

[37] NA57 Technical Proposal, CERN/SPSLC/96-40 (1996).

[38] G. L. Shaw, M. Shin, R. Dalitz and M. Desai, Nature Vol. 377 (1987) 436.

[39] B. S. Kumar, Nucl. Phys. **A590** (1995) 29c-46c.

[40] S. Kabana *et al.*, To be published in the proceedings of *International Symposium on Strange Quark Matter*, Santorini, Greece, April 1997.

[41] U. Heinz, Nucl. Phys. **A566** (1994) 205c-216c.

[42] P. Koch, B. Müller and J. Rafelski, Phys. Rep. **142** (1986) 167.

[43] K. Werner, in *Proc. ICPA–QGP '93*, ed. B. Sinha, Y. P. Viyogi

[44] H. Sorge *et al.*, in *Particle Production in Highly Excited Matter*, ed. H. H. Gutbrod and J. Rafelski, Plenum Press, New York, 1993.

[45] H. Sorge, SUNY–NTG–94–50, October 1994.

[46] N. S. Amelin *et al.*, Phys. Rev. **C47** (1993) 2299.

[47] K. Werner, Nucl. Phys. **A566** (1994)

[48] J. Rafelski, J. Letessier and A. Tounsi, Invited Talk at *4th International Workshop on Relativistic Aspects of Nuclear Physics*, Rio de Janiero, August 1995.

[49] J. Stachel, Nucl. Phys. **A610** (1996) 509c-522c.

[50] A. Corre, CERN/OMEGA 0038N/AC/sm.

[51] *MBNIM User's Guide*, ed. F. Bourgeois, CERN/EF (1984).

[52] H. Grote and I. McLaren, *EPIO User's Guide*, CERN Program Library (1993).

[53] 2 J.-C. Lassalle *et al.*, *TRIDENT User's Manual*, DD/EE/79-2.

[54] *NAGLIB Manual FORTRAN Mark 13 Volume 4*, NAGLIB (1988).

[55] J. Podolanski and R. Armenteros, Phil. Mag **45** (1954) 13.

[56] Thesis of A. C. Bayes, *Strange Particle Production in Sulphur-Sulphur Interactions at 200 GeV/c per Nucleon*, The University of Birmingham (1995).

[57] GENBOD short write–up, CERN Program Library Short Write–ups W515 (1996).

[58] S. Abatzis *et al.*, Phys. Lett. **B393** (1997) 210-216.

[59] The NA35 Collaboration, Nucl. Phys. **A566** (1994) 35c.

[60] H. C. Eggers and J. Rafelski, Int. J. of Mod. Phys. **A7** (1991) 1067.

[61] F. James and M. Roos, *MINUIT manual*, CERN Program Library D506.

[62] T. Åkesson *et al.*, Nucl. Phys. **B354** (1984) 1-11.

[63] I. Derado *et al.*, Z. Phys. **C50** (1991) 31-36.

[64] J. Bartke *et al.*, Z. Phys. **C48** (1990) 191-200.

[65] S. Abatzis *et al.*, Phys. Lett. **B316** (1993) 615.

[66] A. K. Holme *et al.*, To be published in the proceedings of *International Symposium on Strange Quark Matter*, Santorini, Greece, April 1997.

[67] RHIC letter of intent for an experiment on Particle and Jet production at Midrapidity, The STAR collaboration, LBL reports 29651 and 31040.

[68] PHENIX conceptual design report : an experiment to be performed at the Brookhaven national laboratory relativistic heavy ion collider, edited by Nagamiya, S., Aronson, S., Young, G. and Paffrath, L., publ. Upton, Brookhaven, N.Y. 1993.

[69] ALICE - Technical Proposal for A Large Ion Collider Experiment at the CERN LHC, CERN/LHCC/95-71, December 1995.